

**Computational Molecular Design for Developing Metal-Free Organic Emissive Materials**

by

Ramin Ansari

A dissertation submitted in partial fulfillment  
of the requirements for the degree of  
Doctor of Philosophy  
(Chemical Engineering)  
in the University of Michigan  
2022

Doctoral Committee:

Professor John Kieffer, Co-Chair  
Professor Jinsang Kim, Co-Chair  
Assistant Professor Bryan R. Goldsmith  
Professor Robert M. Ziff  
Associate Professor Paul Zimmerman

Ramin Ansari

raminans@umich.edu

ORCID iD: 0000-0002-1844-7762

© Ramin Ansari 2022

## **Dedication**

To My Family

For all that they have done for me and all that they are still doing

## **Acknowledgements**

Foremost, I would like to express my sincere gratitude to my PhD advisor, Prof. John Kieffer, and my co-advisor, Prof. Jinsang Kim, for their wonderful mentorship and unconditional support. I want to thank them for always believing in me and providing me with great career and life advice. Under their guidance, I successfully overcome many difficulties and learnt a lot from them. I would like to also thank the rest of my thesis committee: Prof. Bryan R. Goldsmith, Prof. Robert M. Ziff, and Prof. Paul Zimmerman, for their encouragement and insightful comments.

In Prof. Kieffer and Prof. Kim's research lab, I had the opportunity of working with so many talented researchers. I want to thank my great colleagues and collaborators: Dr. Daniel Hashemi, Dr. Seong Jun Yoon, Wenhao Shao, and all my other lab mates for all the inspiring and helpful discussions. I want to thank my friends for always supporting me: Sina, Amirata, Saeid, Danial, Alireza, Elham, Farima, Alireza, and many other great friends. I am very grateful for the encouragement they have given me and for being there by my side.

Finally, I would like to thank my family for all their love and encouragement. My brothers, Armin and Amin, who were my best friends throughout my entire life and have always been by my side during my happy and difficult times; my father, Yahya Ansari, who always taught me to work hard and shoot for the stars; and most importantly, my mother, Farzaneh Nikfar, for all her sacrifice and care. I would have never reached this place without them.

## Table of Contents

Dedication .....	ii
Acknowledgements .....	iii
List of Tables .....	vii
List of Figures .....	viii
List of Schemes .....	xi
Abstract .....	xii
Chapter 1 Introduction .....	1
1.1 Thesis Overview .....	1
1.2 Background and Motivation .....	2
1.2.1 Thermally Activated Delayed Fluorescence .....	2
1.2.2 Metal Free Room-Temperature Phosphorescence (RTP).....	4
1.2.3 White Light Emission from a Single Molecule .....	6
1.2.4 Applications of Machine Learning in Materials Science and Molecular Property Prediction .....	8
1.3 References .....	9
Chapter 2 Charge Transfer as the Key Parameter Affecting the Color Purity of TADF Emitters	12
2.1 Introduction .....	12
2.2 Methodologies .....	16
2.2.1 Experimental Section.....	16
2.2.2 Synthesis of Molecules .....	17
2.2.3 Computational Method.....	23

2.3 Results and Discussion .....	25
2.4 Conclusions .....	36
2.5 References .....	36
Chapter 3 The Role of Halogen Bonding in Metal Free Phosphors .....	41
3.1 Introduction .....	41
3.2 Methodologies .....	44
3.3 Results and Discussion .....	46
3.4 Conclusions .....	56
3.5 References .....	57
Chapter 4 Molecular Design for Fluorene Based Metal Free White Light Emitters .....	61
4.1 Introduction .....	61
4.2 Methodologies .....	64
4.3 Results and Discussion .....	64
4.3.1 Effect of Modifying the Functional Group on the Non-bonding Electrons of Oxygen and the Fluorescence Quantum Yield .....	64
4.3.2 Effect of Extending the Conjugation on Electronic Transitions .....	67
4.4 Conclusions and Summary .....	70
4.5 References .....	71
Chapter 5 Accurate Prediction of Free Solvation Energy of Organic Molecules via Graph Based Machine Learning Models from Pairwise Atomistic Interactions .....	74
5.1 Introduction .....	74
5.2 Methods .....	78
5.2.1 Graph Representation of Molecules .....	78
5.2.2 Message Passing Neural Network (MPNN).....	80
5.2.3 Graph Attention Network (GAT) .....	81
5.2.4 Feature Aggregation .....	82

5.3 Computational Setup and Results.....	84
5.4 Discussion .....	87
5.5 Conclusions .....	90
5.6 References .....	91
Chapter 6 Conclusion.....	97
Appendices.....	103

## List of Tables

Table 2-1. Molecular structures and emission bandwidth of some of the TADF emitters. <sup>a</sup> Measured FWHM in nm, as reported in the references. <sup>b</sup> Converted to eV using the reported emission spectrum in the references .....	14
Table 2-2. Summary of key computational and experimental results. Energy of first singlet ( $S_1$ ), oscillator strength ( $f$ ) energy of first triplet states ( $T_1$ ), and energy gap between $S_1$ and $T_1$ ( $\Delta E_{ST}$ ) were calculated using DFT at the B3LYP/6-31g(d,p) level in vacuum; overlap integral between HOMO and LUMO were calculated at the CAM-B3LYP/6-31g(d,p) level using multiwfn, <sup>43</sup> the experimental $\Delta E_{ST}$ and emission FWHM were measured in $10^{-5}$ M toluene solution at 25 °C ...	30
Table 3-1. Calculated and experimental lattice constants for F6A, Cl6A, Br6A, and I6A .....	48
Table 3-2. Calculated properties of halogen bond interaction for F6A, Cl6A, Br6A, and I6A....	49
Table 4-1. where the non-bonding electrons of oxygen lie and the energy gaps between that orbital and the HOMO .....	66
Table A-1. Summary of emission peak, FWHM, and HOMO/LUMO overlap coefficient of oCzBN in various solvents along with their relative polarity .....	107
Table A-2. [a] HONTO/LUNTO overlap coefficient for the first singlet state transition, [b] HOMO/LUMO overlap coefficient for ground state optimized structure and [c] HOMO/LUMO percentage for $S_1$ transition which shows the $S_1$ transition is mostly HOMO to LUMO at B3LYP/6-31G(d,p) level. [d] HONTO/LUNTO overlap coefficient for the first singlet state transition, [e] HOMO/LUMO overlap coefficient for ground state optimized structure at CAM-B3LYP/6-31G(d,p) level.....	108
Table A-3. Photophysical data for oDPABN, oDMACBN, and oPSeZBN in Toluene at 300 K (concentration $10^{-5}$ M). Second column shows the excitation wavelength used for the measurement. Third and fourth column show the absolute quantum yield (QY) in air and relative QY in vacuum, respectively. The QY is measured in air only, and the relative QY in vacuum is calculated by comparing the emission intensity with and without air. The photophysical properties and TADF characteristic of oCzBN, mCzBN, oPheBN, and mPheBN have been reported in the literature; all other molecules are synthesized and characterized for the first time in this work. This table shows that the oDMACBN and oPSeZBN have TADF characteristic, since the QY increases in vacuum condition (No oxygen). However, oDPABN does not have TADF characteristic and that's because of the relatively large $\Delta E_{ST}$ of this compound ( $\Delta E_{ST} = 0.313$ eV).....	109



## List of Figures

Figure 2-1. Conventional TADF molecular design. Donor and Acceptor groups can rotate around D-A connection which enhances the structural relaxation in the excited states, resulting in large stokes shift and a broad emission. However, in this contribution we systematically demonstrate that the molecular rotation is not the major cause of the broad emission of TADF. ....	13
Figure 2-2. D-A-D TADF molecules investigated in this study. ....	28
Figure 2-3. Chemical structures and calculated distributions of HOMOs and LUMOs using CAM-B3LYP/6-31g(d,p) level in vacuum. Stronger donor results in more separated HOMO and LUMO. ....	29
Figure 2-4. Correlation between measured FWHM and calculated HOMO/LUMO overlap. ....	31
Figure 2-5. Torsional potential energy of investigated molecules (ortho position) as a function of donor-acceptor dihedral angle from DFT calculations at the CAM-B3LYP/6-31g(d,p) level. ....	32
Figure 2-6. Chemical structures of oPheBN and mPheBN and the differences in the differences in the optimized geometries between the ground and first singlet excited states, hydrogens are not shown for clarity. oPheBN shows 6.6° change in the dihedral angles between the donor and acceptor, however, mPheBN shows a higher dihedral angle change of 15.5°. (b) Torsional potential energy of of oPheBN (black), mPheBN (red), oCzBN (blue), and mCzBN (purple) as a function of donor-acceptor dihedral angle from DFT calculations at the CAM-B3LYP/6-31G(d,p) level. (c) Temperature dependence FWHM of oPheBN (black), mPheBN (red), oCzBN (blue), and mCzBN (purple) in 10 <sup>-5</sup> M toluene solution (The FWHM discrepancy between (c) and table 2-1 is because different fluorimeters were used, but measurements are consistent within each data set). ....	34
Figure 3-1. The unit cell structure of the Br6A crystal. The a lattice constant is along the x axis, the b lattice constant is along the y axis, and the c lattice constant is along the z axis. ....	43
Figure 3-2. Total DOS of Br6A Crystal, with different b lattice constant. By decreasing b lattice constant, the halogen bond length decreases accordingly and there is a red shift in the LUMO states. All spectra are aligned relative to the Fermi level. ....	50
Figure 3-3. Site projected electronic density of states of Crystal Br6A. Bromine in crystal (blue trace), oxygen in crystal (red trace), total density of states of Br6A crystal (black trace). All spectra are aligned relative to the Fermi level. ....	51
Figure 3-4. Calculated distributions of HOMO (bottom) and LUMO (top) orbitals of the Br6A molecule using B3LYP/6-31g(d,p) level in vacuum .....	52

Figure 3-5. Charge density difference plots of X6A with the isosurface level of $0.0006 \text{ e}\text{\AA}^{-3}$ . Blue and red regions denote loss (depletion) and gain (accumulation) of charges, respectively. a lattice constant is along x axis, b lattice constant is along y axis, and c lattice constant is along z axis. ....	53
Figure 3-6. Plot of the plane-averaged electron density difference along the direction of the halogen bonding. The solid and dotted line represent charge accumulation and depletion, respectively. ....	54
Figure 3-7. COHP analysis for halogen and Oxygen orbitals. The various components show the dominating orbital interactions in each case. Note that x axis for F is ten times smaller than others. All spectra are aligned relative to the Fermi level. ....	56
Figure 4-1. Chemical structures of designed phosphors and their phosphorescent color image upon UV irradiation (365nm) under N <sub>2</sub> . Fluorescence and phosphorescence quantum yields of Br-FL compounds (left). Steady state emission spectra of Br-FL compounds in aPMMA films (right). Figure adopted from Jaehun Jung's thesis. <sup>30</sup> ....	63
Figure 4-2. HOMO-4 to LUMO orbitals for Br-FL series.....	65
Figure 4-3. The nature of the frontier orbitals for Br-FL molecules. The blue lines show $\pi\pi^*$ orbitals and the red lines are $n\pi^*$ orbitals. Green lines indicate ground state S <sub>0</sub> . The yellow arrows show the El-Sayed allowed intersystem crossing routes. ....	67
Figure 4-4. Energy diagram for the HOMO and LUMO molecular orbitals of hydrogen, ethene, and 1,3-butadiene.....	68
Figure 4-5. Br-FL3, Br-FL4, the newly designed compounds, and their singlet and triplet energy levels. As it can be seen, extending the conjugation redshifts the fluorescence and phosphorescence emission peaks. ....	70
Figure 5-1. Example of node (atom) and edge (bond) features for a sample molecule, 2-Nitrotoluene. ....	80
Figure 5-2. The fundamental architecture of the model (top left), an example of the model with methanol as the solvent and chlorobenzene as the solute (top right), and an explanation describing how the model works (bottom). ....	84
Figure 5-3. Figure 3: MAE (top left) and RMSE (top right) for Solvation free energy models for test dataset. MPNN and GAT are done in this study. Scatter plot for true (y-axis) and ML predicted (x-axis) values of solvation energies for MPNN (bottom left), and GAT (bottom right). All results are averaged over 10 independent runs. ....	86
Figure 5-4. The mean absolute error and the number of compounds in the dataset for different solvents. The mean absolute error is calculated based on the prediction of the test dataset. The mean absolute error tends to be larger for the solvents that present less in the dataset. ....	88
Figure A-1. UV-vis absorption spectra of the investigated molecules. ....	103

Figure A-2. Photoluminescence spectra of the investigated molecules (a) in nm and (b) in eV.	104
Figure A-3. Photoluminescence (PL) spectra of oDPABN in various solvents (a) in nm and (b) in eV (concentration $10^{-5}M$ ).....	105
Figure A-4. Photoluminescence (PL) spectra of oCzBN in various solvents (a) in nm and (b) in eV (concentration $10^{-5}M$ ).....	106
Figure A-5. Correlation between measured FWHM and calculated HOMO/LUMO overlap of oCzBN in various solvents using the polarizable continuum model (PCM) at the CAM-B3LYP/6-31G(d,p) level. More details can be found in the computational method section.....	107
Figure A-6. Chemical structures and calculated distributions of HONTO and LUNTO for the first singlet state ( $S_1$ ) transition at CAM-B3LYP/6-31G(d,p) level.....	108

## List of Schemes

Scheme 2-1. Synthetic routes of the molecules investigated in this work.....	17
Scheme 2-2. Synthesis of oDPABN. ....	18
Scheme 2-3. Synthesis of oCzBN.....	18
Scheme 2-4. Synthesis of mCzBN.....	19
Scheme 2-5. Synthesis of oPheBN. ....	20
Scheme 2-6. Synthesis of mPheBN. ....	21
Scheme 2-7. Synthesis of oDMAcBN. ....	21
Scheme 2-8. Synthesis of 10H-Phenoselenazine. ....	22
Scheme 2-9. Synthesis of oPSeZBN.....	23

## Abstract

Organic emissive materials have gained a great deal of attention due to their prominence in electronic displays, solid-state lighting, bio-probes for imaging, and sensor applications. Organic materials exhibiting thermally activated delayed fluorescence (TADF) can fully utilize triplet excitons, but their implementation is limited due to broad emission spectra (color impurity), which are principally attributed to the torsional mobility about the twist angle between the donor and acceptor groups. Our methodical computational and experimental investigation reveals that it is the dramatic change of electron configuration between ground and charge-transfer excited states that causes the broad emission. For compounds with the same rotational barrier the FWHM increases significantly when enhancing the charge transfer character. Conversely, when increasing rotational restrictions, emitters show minimal change in their FWHM. Accordingly, to constrict emission broadening it is preferable to control the charge-transfer character of emitter molecules by introducing chromophores with localized emission (LE) character, exhibiting minimal change in electron configuration upon emission.

Besides TADF materials, metal-organic phosphors can also theoretically realize 100% internal quantum efficiencies, but they suffer from stability issues as a result of the weak metal–ligand bonds. Hence, there is interest in developing all-organic phosphorescent OLEDs. The elimination of the heavy metals brings with it new challenges, such as weak spin–orbit coupling interactions and non–radiative decays due to molecular vibrations. In all-organic systems, the enhanced spin-orbit coupling necessary for phosphorescence is thought to be due to the halogen

bonding. To elucidate the underlying mechanism, the electronic and optical properties of purely organic phosphor candidates were investigated using density functional theory (DFT) and time-dependent DFT (TDDFT). Accordingly, iodine forms the strongest halogen bond and fluorine forms the weakest. The strong halogen bonding in crystalline Br and I derivatives more effectively suppresses vibrations and prevents non-radiative decays compared to F and Cl derivatives. Moreover, for heavy atoms, spin-orbit coupling is large, thus augmenting spin flipping. Consequently, triplet-to-singlet transitions are most common in molecules containing iodine and bromine.

White purely organic light-emitting materials have attracted attention for their practicality in many applications such as lighting, sensing, and imaging. Commonly reported designs combine multiple emissive layers where two or more materials simultaneously emit electromagnetic radiation that together is perceived as white. Led by computation, we have developed a fluorine-based molecular framework for white OLEDs in which fluorescence and phosphorescence from a single molecule are combined, achieving white emission at decreased device fabrication cost. A rigid molecular structure is essential for efficient phosphorescence emission so that the vibration is suppressed. Fluorescence emission can be enhanced by suppressing the  $S_1$  to  $T_1$  El-Sayed enhanced intersystem crossing.

Finally, we developed a graph-based machine learning (ML) model to predict the solvation free energies from solvent-solute pair-wise interactions. To this end, we explore two novel deep learning architectures: message passing neural network and graph attention network. The ML methods yield more accurate predictions of solvation free energies than state of the art deep learning or quantum mechanical methods, at lower computational costs. The ability to predict chemical properties is important for developing new materials with specific properties,

especially for OLED applications. Reliable predictive models allow for efficiently screening candidate organic molecules, and accelerate materials design and development.

## Chapter 1 Introduction

### 1.1 Thesis Overview

In terms of investigatory methodologies, this thesis research relies on computational and data driven techniques, including molecular simulations, first-principles electronic structure calculations, and machine learning procedures. With the research strategy laid out in this document, we established a workflow that is consistent with the mandate of Materials Genome Initiative, seamlessly integrating computational and experimental efforts, and we believe to have demonstrated the efficacy of this concept in terms of accelerating materials development for organic electronic applications.

The contents of the thesis are divided into 6 chapters. The first chapter is an introductory chapter, including motivation and background and major findings and achievements for each main project. The results of the four main projects are presented in Chapter 2, 3, 4, and 5.

Chapter 2 presents the study of the emission bandwidth of thermally activated delayed fluorescence (TADF) emitters. Our results suggest that the intrinsic TADF emission bandwidth is primarily determined by the charge transfer character of the molecule, rather than its propensity for rotational motion, which offers a renewed perspective on the rational molecular design of organic emitters exhibiting sharp emission spectra.

In Chapter 3, we report our study of the effect of halogen bonding on metal-free phosphors. The electronic and optical properties of purely organic phosphor candidates are investigated using density functional theory calculations. It is revealed that iodine forms the strongest halogen bonding interaction and fluorine forms the weakest interaction. The strong



halogen bonding more effectively suppress vibrations and prevent non-radiative decays compared to F and Cl derivatives.

Chapter 4 details our investigation of white light emission from a single organic molecule by combining fluorescence and phosphorescence emissions. White light emission has recently been in great demand for many applications. However, current white OLEDs include several emitting layers, which increases the cost of fabrication of these devices. In contrast single molecule white light OLEDs have a much lower fabrication cost.

Chapter 5 describes a graph based deep learning model that we developed to predict the solvation free energies from solvent-solute pair-wise interactions. We show that our proposed models outperform all quantum mechanical and molecular dynamics methods in addition to existing alternative machine learning based approaches in the task of solvation free energy prediction. Such machine learning models are expected to accelerate property predictions such as excited state levels, and singlet-triplet energy gaps beyond what molecular simulations and DFT calculations can achieve with today's computational resources. Here we test the approach for one of the fundamental molecular design criteria, in anticipation of translating this workflow for the development of organic materials for OLED and TADF applications.

Chapter 6 gives a final summary, including major findings in this thesis study. An outlook for future research in this field is also given. The next section gives an introduction for the main four projects presented in this thesis.

## **1.2 Background and Motivation**

### **1.2.1 Thermally Activated Delayed Fluorescence**

In an OLED device, electrically injected charge carriers form singlet and triplet excitons in a 1:3 ratio.<sup>1</sup> In a triplet state the excited electron is no longer paired with the ground state

electron; that is, they are parallel. Since the decay from triplet state back to ground state involves an additional spin rotation, it is often called forbidden transitions. Forbidden transitions occur at much lower speeds than allowed transitions. The goal of OLED research is to overcome the limitation imposed by forbidden decay from triplet states. Although phosphorescent emitters have high quantum yields, they suffer instability issues in particular for blue OLEDs.<sup>1</sup> Hence, as an alternative, blue fluorescent emitters have been used in OLED devices. However, the internal quantum efficiency (IQE) of fluorescence OLEDs is limited to 25%,<sup>2</sup> so the external quantum efficiency (EQE) can be 7.5% at most (assuming the efficiency with which the generated light comes out of the device is 20-30%).

One approach to realize high IQEs without using metals is to promote the first triplet ( $T_1$ ) to first singlet ( $S_1$ ) reverse intersystem crossing (ISC) by carefully designing organic molecules so as to exhibit a small energy gap ( $\Delta E_{ST}$ ) between  $S_1$  and  $T_1$  levels.<sup>3,4</sup> This allows for non-radiative triplet states to up-convert to radiative singlet states, a process called thermally activated delayed fluorescence (TADF). Therefore, 100% IQE can be realized. One strategy to minimize ( $\Delta E_{ST}$ ) is to configure molecules in a donor-acceptor (D-A) electronic alternation. Therefore, the highest occupied molecular orbital (HOMO) and the lowest unoccupied molecular orbital (LUMO) are localized on the donor and acceptor moieties, respectively, leading to a small overlap of HOMO and LUMO orbitals. The  $\Delta E_{ST}$  is equal to twice of the electron exchange energy ( $J$ ) as illustrated in equation (1), and  $J$  is determined by the spatial overlap extents of HOMO and LUMO.<sup>5</sup> Therefore, the smaller the overlap of HOMO and LUMO the smaller  $J$  and  $\Delta E_{ST}$  values.<sup>6</sup>

$$\Delta E_{ST} = E_{S_1} - E_{T_1} = 2J \quad (1)$$

One major challenge with TADF emitters is that they have a broad emission spectrum, whose full-width at half-maximum (FWHM) is 70-100 nm. This broad emission has imposed a serious challenge for display manufacturers to achieve standard emission colors. Therefore, OLED displays are employed with color filters<sup>7,8</sup> in order to achieve the color standard requirements defined by the Commission Internationale de l'Eclairage (CIE). The employed color filters are used to narrow the broad emission peaks. However, they significantly decrease the EQE of the OLED displays. Therefore, designing molecules with sharp and narrow emission is important for the development of OLED technology.

In Chapter 2, the key factors determining the emission bandwidth of TADF emitters are investigated by combining computational and experimental approaches. To achieve high IQEs in metal-free organic light emitting diode via TADF, the first triplet ( $T_1$ ) to first singlet ( $S_1$ ) reverse intersystem crossing (rISC) is promoted by configuring molecules in an electron donor-acceptor (D-A) alternation with a large dihedral angle, which results in a small energy gap ( $\Delta E_{ST}$ ) between  $S_1$  and  $T_1$  states. This allows for effective non-radiative up-conversion of triplet excitons to singlet excitons that fluoresce. However, this traditional molecular design of TADF results in broad emission spectral bands. Despite reports suggesting that suppressing the D-A dihedral rotation narrows the emission band,<sup>9,10</sup> the origin of emission broadening remains elusive. Indeed, our results suggest that the intrinsic TADF emission bandwidth is primarily determined by the charge transfer character of the molecule, rather than its propensity for rotational motion, which offers a renewed perspective on the rational molecular design of organic emitters exhibiting sharp emission spectra. This work is published in ACS Applied Material & Interfaces.<sup>11</sup>

### **1.2.2 Metal Free Room-Temperature Phosphorescence (RTP)**

Organic light emitting diodes (OLEDs) based on transition metal complexes have been widely used over recent decades because of their display and solid-state lighting applications.<sup>12</sup> Increasing attention has been devoted to phosphorescence materials because they can theoretically realize threefold higher internal quantum efficiency (IQE) compared to fluorescent alternatives by harvesting triplet excitons through intersystem crossing (ISC).<sup>2</sup> Most candidates for efficient phosphorescence are based on heavy element complexes because the presence of a heavy atom increases spin-orbit coupling (SOC) interactions.<sup>13</sup> Therefore, the SOC interactions in such molecules are substantial and a change of spin is more favorable. Although organometallic materials have high quantum efficiency, they require expensive and rare elements such as iridium<sup>14</sup> and platinum.<sup>15</sup> Organometallic materials also experience short device lifetimes due to the degradation of weak and unstable metal-ligand bonds.<sup>16</sup>

Unlike organometallics, purely organic materials are cheaper, lighter, readily functionalized, and easily processed. Until now, only a few examples of purely organic molecules with a high phosphorescence quantum yield have been reported.<sup>17</sup> This scarcity is often related to the fact that purely organic phosphors exhibit long-lived triplet states, which are easily consumed by vibrational effects that prevent emissive decay. To be competitive with organometallic OLEDs, purely organic materials must (1) suppress vibrations in order to prevent non-radiative decays and (2) promote the intersystem crossing rates by increasing spin-orbit coupling interactions.

To suppress vibrational relaxations of the triplet manifold, several approaches have been developed. In 2011, Bolton et al.<sup>18</sup> reported enhanced room-temperature phosphorescence (RTP) from pure organic luminogens utilizing mixed crystals and halogen bonding. The enhanced spin-orbit coupling necessary for phosphorescence is thought to be due to the halogen

bonding. Strong halogen bonding more effectively suppresses vibrations and prevent non-radiative decays. To elucidate the underlying mechanism, the electronic and optical properties of purely organic phosphor candidates are investigated using density functional theory calculations. The unit cell structure of a known organic phosphor containing bromine is used to validate the accuracy of the computational methodology. Compared to experiments, the calculated lattice constants deviate by less than 1 percent for each lattice constant. The same computational approach is then used to predict the lattice constants for molecular analogs containing fluorine, chlorine, and iodine. Electronic structure and photonic properties of the predicted crystals are computed. Finally, the presence of halogen bonding is corroborated, with fluorine forming the weakest and iodine the strongest halogen bonding interactions. Our findings demonstrate how computational methods can be effectively used for the predictive design of organic materials in lighting devices. The results and analysis of this project is presented in Chapter 3 of this thesis. Also, this work is published in *Physical Chemistry Chemical Physics*.<sup>19</sup>

### **1.2.3 White Light Emission from a Single Molecule**

White light emission has recently been in great demand for bioimaging, sensor applications, solid-state light-emitting-diode (LED), backlight in liquid-crystal displays, and illumination sources.<sup>20–22</sup> Various approaches have been developed to design white organic LEDs (WOLEDs) such as, combining several fluorophors or phosphors in a single emitting layer,<sup>23,24</sup> synthesizing polymers incorporating different color emitting moieties,<sup>25</sup> stacking several OLEDs,<sup>26</sup> and devising multilayer electroluminescence devices doped with different color emitting dopants.<sup>27</sup> Although several WOLEDs have been reported, most of the reported cases include several emitting layers, which increases the cost of fabrication of these devices. The recombination current and performance of each layer needs to be controlled by layer

thickness and doping concentration. Furthermore, to facilitate hole and electron transfer in the device, hole and electron transport layers (HTL/ETL) need to be incorporated on either side of the emitter layers. Therefore, the single doped and single emissive layer devices would be much simpler and cheaper than the widely reported stacked, multi-emissive-layer or triple doped WOLEDs.<sup>28,29</sup> In search for designing a single organic molecule that generates white light (single molecule white light emitters (SMWLEs)), we investigated a series of fluorine-based molecules that Jaehun Jung<sup>30</sup> has developed and synthesized. These molecules show high quantum yield phosphorescence emission. Surprisingly, some of these molecules also show high quantum yield fluorescence emission as well. However, the combination of fluorescent and phosphorescent emission of these molecules is not perceived as white but more in the blue region.

We computationally studied these molecules, and we were able to understand the structure-property relationship. Our computational analysis shows that the non-bonding electrons of oxygen in these molecules produces a  $^3n\pi^*$  triplet state with different energy levels. According to El-Sayed's rule, for the molecules with a low energy level  $^3n\pi^*$  triplet state the intersystem crossing rate between  $^1\pi\pi^*$  and  $^3n\pi^*$  states is much more efficient. Therefore, due to efficient singlet to triplet ISC, these molecules are very weakly fluorescent. However, for some of these molecules the  $^3n\pi^*$  triplet state is in a high energy level ( $T_8$ ) and is not accessible. Therefore, the El-Sayed's rule allow  $^1\pi\pi^* \leftrightarrow ^3n\pi^*$  transition is blocked for these molecules, leading to a more efficient fluorescence emission.

By carefully modifying these molecules we have been able to shift the fluorescence and phosphorescence peaks so that the combination of both generates white light. Our computational analysis shows that by extending the conjugation we were able to redshift the fluorescence and

phosphoresce peaks, without changing the  $^3n\pi^*$  triplet state's energy level. Our proposed molecules can be used to make white OLEDs with just a single emissive layer. The results and analysis of this project is presented in Chapter 4 of this thesis.

## **1.2.4 Applications of Machine Learning in Materials Science and Molecular Property**

### **Prediction**

Solvation free energy is an important index in the field of organic synthesis, medicinal chemistry, drug delivery, and biological processes.<sup>31-34</sup> However, accurate solvation free energy determination is a time-consuming experimental process. Furthermore, it could be useful to assess solvation free energies in the absence of a physical sample. Deep learning based methods have been widely applied to predict various kinds of molecular properties in material sciences and pharmaceutical industry with increasingly more success.<sup>35,36</sup> In this study, we propose two deep learning models for the problem of free solvation energy predictions, based on the Graph Neural Network (GNN) architectures: Message Passing Neural Network (MPNN) and Graph Attention Network (GAT). Graph Neural Network (GNN) architectures have been widely used for social media, content recommendation, advertisement, and etc. However, molecules can also be expressed in the form of graphs, with the inclusion of the chemical information. Graphs provide a natural way of describing molecular structures as atoms can be represented by nodes and chemical bonds by edges.<sup>37,38</sup>

GNNs are capable of summarizing the pertinent information about a molecule as low-dimensional features directly from its graph structure without relying on an extensive amount of intra-molecular descriptors. As a result, these models are capable of making accurate predictions of the molecular properties without the time consuming process of running an experiment on each molecule. We show that our proposed models outperform all quantum mechanical and

molecular dynamics methods in addition to existing alternative machine learning based approaches in the task of solvation free energy prediction. We believe such promising predictive models will be applicable to enhancing the efficiency of material property predictions and be a useful tool to the screening of molecular candidates for various applications.

### 1.3 References

- (1) Shizu, K.; Noda, H.; Tanaka, H.; Taneda, M.; Uejima, M.; Sato, T.; Tanaka, K.; Kaji, H.; Adachi, C. Highly Efficient Blue Electroluminescence Using Delayed-Fluorescence Emitters With Large Overlap Density Between Luminescent and Ground States. *The Journal of Physical Chemistry C* **2015**, *119*, 26283-26289.
- (2) Adachi, C.; Baldo, M. A.; Thompson, M. E.; Forrest, S. R. Nearly 100% Internal Phosphorescence Efficiency in an Organic Light-Emitting Device. *Journal of Applied Physics* **2001**, *90*, 5048-5051.
- (3) Uoyama, H.; Goushi, K.; Shizu, K.; Nomura, H.; Adachi, C. Highly Efficient Organic Light-Emitting Diodes From Delayed Fluorescence. *Nature* **2012**, *492*, 234-238.
- (4) Kim, M.; Yoon, S. J.; Han, S. H.; Ansari, R.; kieffer, J.; Lee, J. Y.; Kim, J. Molecular Design Approach Managing Molecular Orbital Superposition for High Efficiency Without Color Shift in Thermally Activated Delayed Fluorescent Organic .... *Chemistry—A European Journal* **2019**, *25*, 1829-1834.
- (5) Endo, A.; Ogasawara, M.; Takahashi, A.; Yokoyama, D.; Kato, Y.; Adachi, C. Thermally Activated Delayed Fluorescence From Sn<sup>4+</sup>–Porphyrin Complexes and Their Application to Organic Light Emitting Diodes—a Novel Mechanism for Electroluminescence. *Advanced Materials* **2009**, *21*, 4802-4806.
- (6) Chen, T.; Zheng, L.; Yuan, J.; An, Z.; Chen, R.; Tao, Y.; Li, H.; Xie, X.; Huang, W. Understanding the Control of Singlet-Triplet Splitting for Organic Exciton Manipulating: A Combined Theoretical and Experimental Approach. *Scientific reports* **2015**, *5*, 1-11.
- (7) Cho, T.-Y.; Lin, C.-L.; Wu, C.-C. Microcavity Two-Unit Tandem Organic Light-Emitting Devices Having a High Efficiency. *Applied physics letters* **2006**, *88*, 111106.
- (8) Poitras, D.; Kuo, C.-C.; Py, C. Design of High-Contrast Oleds With Microcavity Effect. *Optics express* **2008**, *16*, 8003-8015.
- (9) Chen, D.-Y.; Liu, W.; Zheng, C.-J.; Wang, K.; Li, F.; Tao, S. L.; Ou, X.-M.; Zhang, X.-H. Isomeric Thermally Activated Delayed Fluorescence Emitters for Color Purity-Improved Emission in Organic Light-Emitting Devices. *ACS applied materials & interfaces* **2016**, *8*, 16791-16798.



- (10) Cho, Y. J.; Jeon, S. K.; Lee, S.-S.; Yu, E.; Lee, J. Y. Donor Interlocked Molecular Design for Fluorescence-Like Narrow Emission in Deep Blue Thermally Activated Delayed Fluorescent Emitters. *Chemistry of Materials* **2016**, *28*, 5400-5405.
- (11) Ansari, R.; Shao, W.; Yoon, S.-J.; Kim, J.; Kieffer, J. Charge Transfer as the Key Parameter Affecting the Color Purity of Thermally Activated Delayed Fluorescence Emitters. *ACS Applied Materials & Interfaces* **2021**, *13*, 28529-28537.
- (12) Tang, C. W.; VanSlyke, S. A. Organic Electroluminescent Diodes. *Applied physics letters* **1987**, *51*, 913-915.
- (13) Zhou, G.; Wong, W.; Yang, X. New Design Tactics in Oleds Using Functionalized 2-phenylpyridine-type Cyclometalates of Iridium (Iii) and Platinum (Ii). *Chemistry—An Asian Journal* **2011**, *6*, 1706-1727.
- (14) Baldo, M. A.; Lamansky, S.; Burrows, P. E.; Thompson, M. E.; Forrest, S. R. Very High-Efficiency Green Organic Light-Emitting Devices Based on Electrophosphorescence. *Applied Physics Letters* **1999**, *75*, 4-6.
- (15) Baldo, M. A.; O'Brien, D. F.; You, Y.; Shoustikov, A.; Sibley, S.; Thompson, M. E.; Forrest, S. R. Highly Efficient Phosphorescent Emission From Organic Electroluminescent Devices. *Nature* **1998**, *395*, 151-154.
- (16) Siegbahn, P. E. M. Trends of Metal-Carbon Bond Strengths in Transition Metal Complexes. *The Journal of Physical Chemistry* **1995**, *99*, 12723-12729.
- (17) Wang, S.; Yuan, W. Z.; Zhang, Y. Pure Organic Luminogens With Room Temperature Phosphorescence. **2016**, *Aggregation-Induced Emission: Materials and Applications Volume 2*, 1-26.
- (18) Bolton, O.; Lee, K.; Kim, H.-J.; Lin, K. Y.; Kim, J. Activating Efficient Phosphorescence From Purely Organic Materials By Crystal Design. *Nature chemistry* **2011**, *3*, 205-210.
- (19) Ansari, R.; Hashemi, D.; Kieffer, J. The Role of Halogen Bonding in Metal Free Phosphors. *Physical Chemistry Chemical Physics* **2021**, *23*, 23351-23359.
- (20) Du, M.; Feng, Y.; Zhu, D.; Peng, T.; Liu, Y.; Wang, Y.; Bryce, M. R. Novel Emitting System Based on a Multifunctional Bipolar Phosphor: An Effective Approach for Highly Efficient Warm-white Light-emitting Devices With High Color .... *Advanced Materials* **2016**, *28*, 5963-5968.
- (21) Farinola, G. M.; Ragni, R. Electroluminescent Materials for White Organic Light Emitting Diodes. *Chemical Society Reviews* **2011**, *40*, 3467-3482.
- (22) Han, M.; Tian, Y.; Yuan, Z.; Zhu..., L. A Phosphorescent Molecular “Butterfly” That Undergoes a Photoinduced Structural Change Allowing Temperature Sensing and White Emission. *Angewandte Chemie International Edition* **2014**, *53*, 10908-10912.
- (23) Mao, Z.; Yang, Z.; Mu, Y.; Zhang, Y.; Wang, Y. F.; Chi, Z.; Lo, C. C.; Lio, S.; Lien, A.; Xu, J. Linearly Tunable Emission Colors Obtained From a Fluorescent–Phosphorescent Dual-emission Compound By Mechanical Stimuli. *Angewandte Chemie* **2015**, *127*, 6368-6371.

- (24) Sun, Y.; Giebink, N. C.; Kanno, H.; Ma, B.; Thompson, M. E.; Forrest, S. R. Management of Singlet and Triplet Excitons for Efficient White Organic Light-Emitting Devices. *Nature* **2006**, *440*, 908-912.
- (25) Shao, S.; Ding, J.; Wang, L.; Jing, X.; Wang, F. White Electroluminescence From All-Phosphorescent Single Polymers on a Fluorinated Poly (Arylene Ether Phosphine Oxide) Backbone Simultaneously Grafted With Blue .... *Journal of the American Chemical Society* **2012**, *134*, 20290-20293.
- (26) Sun, C. Y.; Wang, X. L.; Zhang, X.; Qin, C.; Li, P.; Su, Z. M.; Zhu, D. X.; Shan, G. G.; Shao, K. Z.; Wu, H.; Li, J. Efficient and Tunable White-Light Emission of Metal–Organic Frameworks By Iridium-Complex Encapsulation. *Nature Communications* **2013**, *4*, 2717.
- (27) Wu, Y. S.; Hwang, S. W.; Chen, H. H.; Lee, M. T.; Shen, W. J.; Chen, C. H. Efficient White Organic Light Emitting Devices With Dual Emitting Layers. *Thin solid films* **2005**, *488*, 265-269.
- (28) He, Z.; Zhao, W.; Lam, J. W. Y.; Peng, Q.; Ma, H.; Liang, G.; Shuai, Z.; Tang, B. Z. White Light Emission From a Single Organic Molecule With Dual Phosphorescence At Room Temperature. *Nature Communications* **2017**, *8*, 416.
- (29) Yang, Q. Y.; Lehn, J. M. Bright White-light Emission From a Single Organic Compound in the Solid State. *Angewandte Chemie International Edition* **2014**, *53*, 4572-4577.
- (30) Jung, J. Enhancing Room Temperature Phosphorescence From Organic Molecules By Internal Heavy Atom Effect and External Agents [Doctoral Dissertation, University of Michigan, Ann Arbor]. **2018**,
- (31) Alhalaweh, A.; Roy, L.; Rodríguez-Hornedo, N.; Velaga, S. P. Ph-Dependent Solubility of Indomethacin–Saccharin and Carbamazepine–Saccharin Cocrystals in Aqueous Media. *Molecular Pharmaceutics* **2012**, *9*, 2605–2612.
- (32) Arnett, E. M.; Bentrude, W. G.; Burke, J. J.; Duggleby, P. M. Solvent Effects in Organic Chemistry. V. Molecules, Ions, and Transition States in Aqueous Ethanol<sup>1</sup>. *Journal of the American Chemical Society* **1965**, *87*, 1541-1553.
- (33) Chremos, A.; Douglas, J. F. Polyelectrolyte Association and Solvation. *The Journal of chemical physics* **2018**, *149*, 163305.
- (34) Steed, J. W.; Atwood, J. L. *Supramolecular chemistry*; 2013;
- (35) Butler, K. T.; Davies, D. W.; Cartwright, H.; Isayev, O.; Walsh, A. Machine Learning for Molecular and Materials Science. *Nature* **2018**, *559*, 547-555.
- (36) Sanchez-Lengeling, B.; Aspuru-Guzik, A. Inverse Molecular Design Using Machine Learning: Generative Models for Matter Engineering. *Science* **2018**, *361*, 360-365.
- (37) Coley, C. W.; Jin, W.; Rogers, L.; Jamison, T. F.; Jaakkola, T. S.; Green, W. H.; Barzilay, R.; Jensen, K. F. A Graph-Convolutional Neural Network Model for the Prediction of Chemical Reactivity. *Chemical science* **2019**, *10*, 370-377.
- (38) Zhou, J.; Cui, G.; Hu, S.; Zhang, Z.; Yang, C.; Liu, Z.; Wang, L.; Li, C.; Sun, M. Graph Neural Networks: A Review of Methods and Applications. *AI Open* **2020**, *1*, 57-81.

## Chapter 2 Charge Transfer as the Key Parameter Affecting the Color Purity of TADF Emitters

### 2.1 Introduction

In an organic light emitting diode (OLED), electrically injected charge carriers form singlet and triplet excitons at a 1:3 ratio.<sup>1-4</sup> To overcome the energy conversion limitation imposed by forbidden emissive transitions from triplet states,<sup>5</sup> the focus has been primarily on organometallic and metal-free organic phosphors, owing to their efficient photon generation from triplet excitons by means of the heavy atom effect.<sup>6-9</sup> As an alternative, thermally activated delayed fluorescence (TADF) has been extensively studied. In this approach, high internal quantum efficiencies (IQEs) without using metals are achieved by promoting the T<sub>1</sub> to S<sub>1</sub> reverse intersystem crossing (rISC) in organic molecules designed to exhibit small energy gaps between S<sub>1</sub> and T<sub>1</sub> levels ( $\Delta E_{ST}$ ).<sup>10-16</sup> Small  $\Delta E_{ST}$  (< 0.1 eV) allow for non-radiative triplet excitons to be up-converted to singlet excitons before decaying radiatively. Therefore, 100% IQE can theoretically be realized. The prevailing molecular design strategy to minimize  $\Delta E_{ST}$  is to configure conjugated organic groups into electron donor-acceptor (D-A) alternation with a large dihedral angle (Figure 2-1). This causes, the highest occupied molecular orbital (HOMO) and the lowest unoccupied molecular orbital (LUMO) to be localized on the donor and acceptor moieties, respectively, leading to small HOMO and LUMO orbital overlap.  $\Delta E_{ST}$  amounts to twice the electron exchange energy,  $J$ , which is determined by the extent of spatial overlap of HOMO and LUMO.<sup>17</sup>

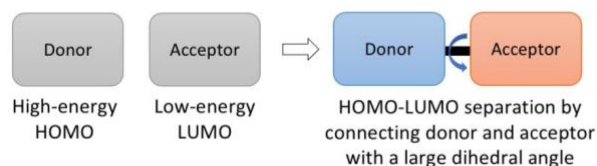


Figure 2-1. Conventional TADF molecular design. Donor and Acceptor groups can rotate around D-A connection which enhances the structural relaxation in the excited states, resulting in large Stokes shift and a broad emission. However, in this contribution we systematically demonstrate that the molecular rotation is not the major cause of the broad emission of TADF.

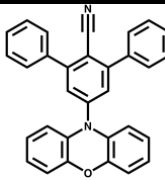
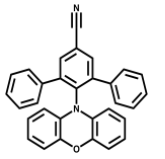
Hence, the smaller the HOMO-LUMO overlap, the easier it is to achieve comparable energy levels for  $S_1$  and  $T_1$ , resulting in small  $\Delta E_{ST}$  values.<sup>18,19</sup> Accordingly, spatially separating HOMO and LUMO orbitals, leading to so-called charge transfer (CT) excited states, is perceived as essential for TADF, and constitutes the conventional design principle for such emitters. Unfortunately, it is also typically observed that CT states exhibit broader emission spectra than locally excited (LE) states (referring to transitions between HOMO and LUMO orbitals with substantial overlap).

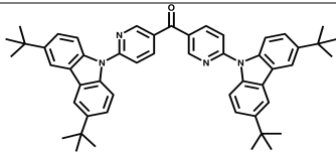
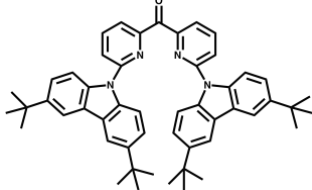
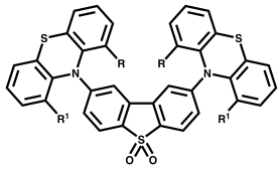
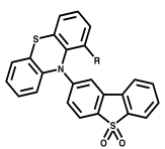
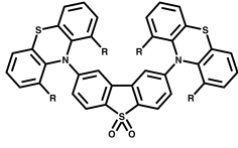
In the literature, the prevalent explanation for this spectral broadening is that excitations across an apportioned D-A configuration causes molecular rotation around the D-A connecting bond (Figure 2-1), resulting in large Stokes shifts and emission spectra with a full-width at half-maximum (FWHM) between 70 and 100 nm.<sup>20</sup> Such broad emission adversely affects color purity, requiring color filters to achieve the color standard requirements when TADF emitters are used in OLED displays.<sup>21,22</sup> The use of color filters is undesirable as it significantly reduces the EQE of OLED displays.

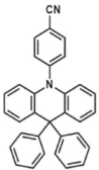
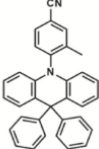
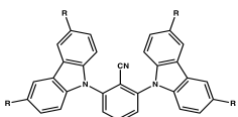
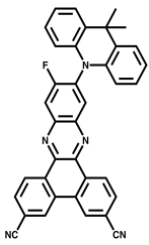
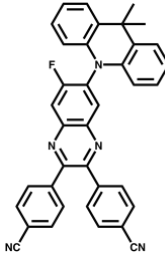
Since the conventional TADF molecular design based on the spatial D-A separation is associated with the combined occurrence of CT and easily excitable torsional rotation between the D-A groups, the question remains whether CT, molecular rotation, or both are responsible for the broad emission characteristics. Rotation between donor and acceptor ensues from the large

dihedral angle that is introduced in conventional TADF designs to facilitate twisted intramolecular charge transfer (TICT). To eliminate this potential energy coupling mechanism, molecular interlocking strategies have been developed where added bulky side chains block the rotational motion between donor and acceptor (Table 2-1).<sup>20,23-28</sup> Assessing whether this approach is indeed effective depends on the clarity of the analysis. We first point out that comparing the FWHM in the wavelength vs. energy domains is ambiguous. Because of the scale inversion, the same peak may appear narrower or broader depending on the absolute emission peak position. Presumably, spectral broadening mechanisms involve interactions between electronic and vibronic excitations, and since dispersion of photons and phonons is described by different physical laws, it is preferable to compare conserved quantities such as momenta or energies to better discern the mechanisms that underlie the shaping of the emission line. Interestingly, converting the reported FWHM of some molecules listed in Table 2-1 into eV dispels the notion that restricting rotation by large steric hindrances would prevent emission broadening. The FWHM on the eV scale does not change, and even a reverse trend is found.

Table 2-1. Molecular structures and emission bandwidth of some of the TADF emitters. <sup>a</sup> Measured FWHM in nm, as reported in the references. <sup>b</sup> Converted to eV using the reported emission spectrum in the references

Compounds	Emitter	FWHM (nm) <sup>a</sup>	FWHM (eV) <sup>b</sup>	Ref.
<b>1</b> 	oPTC	97	0.469	20
<b>2</b> 	mPTC	86	0.442	20

3		3DPyM-pDTC	62	0.347	25
4		2DPyM-mDTC	89	0.420	25
5		R=H R <sup>1</sup> =H Compound1	140	0.457	26
6		R=Me R <sup>1</sup> =H Compound2	130	0.477	26
7		R= <i>i</i> -Pr R <sup>1</sup> =H Compound3	128	0.493	26
8		R=Me R <sup>1</sup> =Me Compound5	110	0.399	26
9		R=H Compound6	100	0.391	26
10		R=Me Compound7	110	0.416	26
11		R=H 1a	95	0.435	27
12		R=Me 3a	100	0.481	27

13		p-ACN	65	0.433	24
14		p-CAN-Me1	65	0.444	24
15		R=H DCzBN1	55	0.41	23
16		R=Me DCzBN2	59	0.40	23
17		R=t-Bu DCzBN3	59	0.41	23
18		R=MeO	79	0.44	23
19		FBPCNAc	96	0.324	28
20		FDQCNAc	86	0.346	28

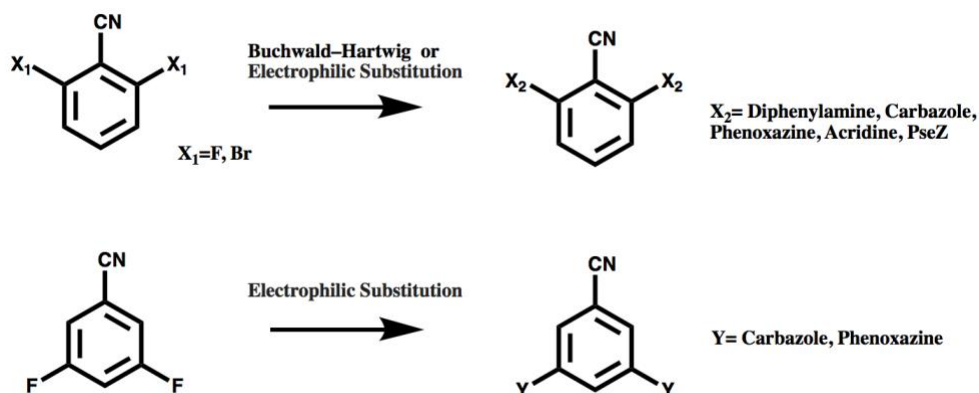
## 2.2 Methodologies

### 2.2.1 Experimental Section

All reactions were conducted under argon atmosphere. All reactants and reagents were obtained from Sigma-Aldrich, unless noted otherwise. Selenium dioxide and sulfolane were purchased from Fisher Scientific. 9,9-Dimethyl-9,10-dihydroacridine was purchased from

Ambeed. NMR spectra were obtained on Varian MR-400. UV-visible absorption spectra of all materials were taken on a Varian Cary 50 Bio spectrometer and photoluminescence emission spectra were conducted using a Horiba PTI QuantaMaster 400.  $\Delta E_{ST}$  has been measured by comparing the fluorescence and phosphorescence spectra at liquid nitrogen temperature.

### 2.2.2 Synthesis of Molecules

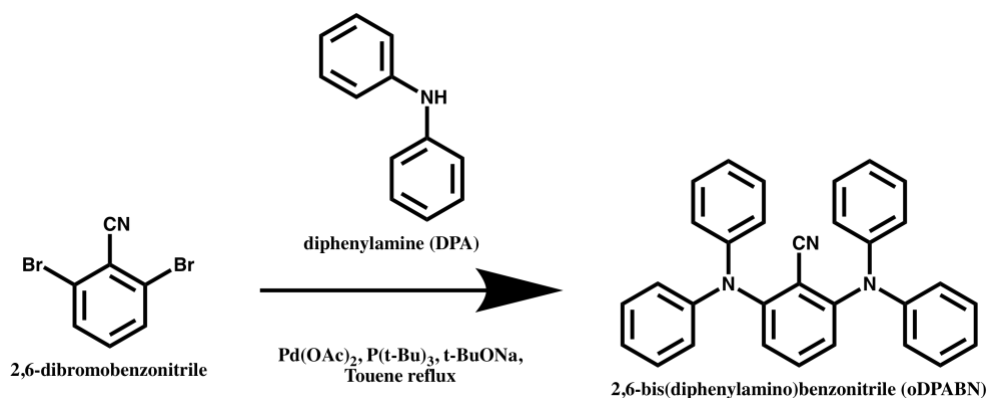


Scheme 2-1. Synthetic routes of the molecules investigated in this work.

Synthetic routes of the molecules investigated in this work are shown in Scheme 2-1. For oDPABN and oPSeZBN, Buchwald-Hartwig cross coupling reaction was employed, and the other molecules were synthesized through electrophilic substitution reaction. The chemical structures of the target compounds were fully characterized and confirmed using nuclear magnetic resonance (NMR) spectroscopy and mass spectrometry (MS). For more information on the synthesis for each molecule please see Schemes 2-2 to 2-9.

#### 2,6-Di(diphenylamine)benzonitrile (oDPABN):

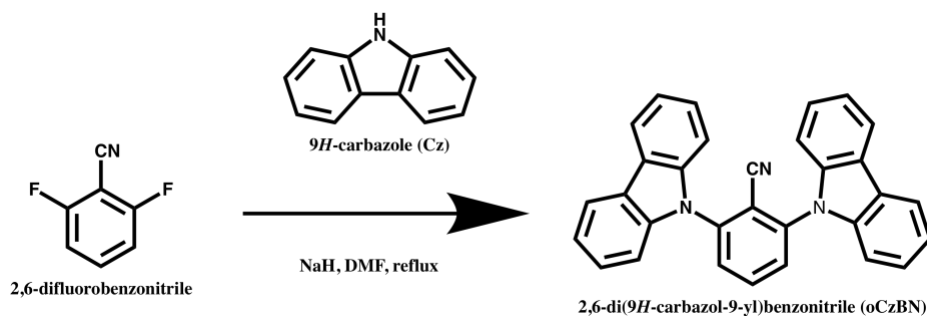




Scheme 2-2. Synthesis of oDPABN.

2,6-Dibromobenzonitrile (0.500 g, 1.916 mmol) and diphenylamine (0.979 g, 5.749 mmol) were dissolved in anhydrous toluene (32 mL). To the solution was added sodium *tert*-butoxide (t-BuONa, 0.5159g, 5.366 mmol), P(t-Bu)<sub>3</sub> (0.22g, 0.767 mmol), and Pd(OAc)<sub>2</sub> (0.0865 g, 0.383 mmol) and the solution degassed by bubbling through argon for 15 min. The mixture heated at 110 °C under argon for 12 h. Filtration is done by washing with methylene chloride (MC) and then evaporate the solvent. Crude product was further purified using column (MC:Hexane 1:3) chromatography (0.54 g, 65 % yield). <sup>1</sup>H NMR (400 MHz, DMSO-*d*<sub>6</sub>) δ 7.57 (t, *J*=8.2 Hz, 1H), 7.36 – 7.21 (m, 8H), 7.08 – 6.90 (m, 14H).

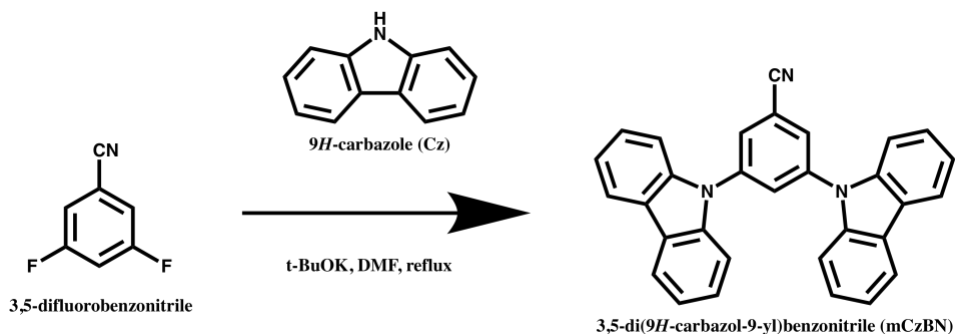
### 2,6-Di(carbazole)benzonitrile (oCzBN):



Scheme 2-3. Synthesis of oCzBN.

Under argon atmosphere, 9H-carbazole (501 mg, 3 mmol) was dissolved in dry N,N-dimethylformamide (30 mL) in a two-neck round-bottom flask equipped with a condenser. The reaction mixture was cooled to 0 °C, then NaH (120 mg, 3 mmol) was added. The reaction mixture was slowly warmed to room temperature and stirred for half an hour. After that, 2,6-difluorobenzonitrile (0.261 g, 1 mmol) was added and the reaction was heated to 150 °C for 16 hours. The reaction was quenched with water and the precipitate was filtered off. The crude product was purified by column chromatography. The white product was obtained as a powder (0.393 g, 70% yield). <sup>1</sup>H NMR (500 MHz, Chloroform-*d*) δ 8.20 – 8.14 (m, 4H), 8.02 (t, *J*=8.1 Hz, 1H), 7.79 (d, *J*=8.1 Hz, 2H), 7.50 (td, *J*=7.5, 7.0, 1.3 Hz, 4H), 7.39 – 7.34 (m, 8H).

### 3,5-Di(carbazole)benzonitrile (mCzBN):

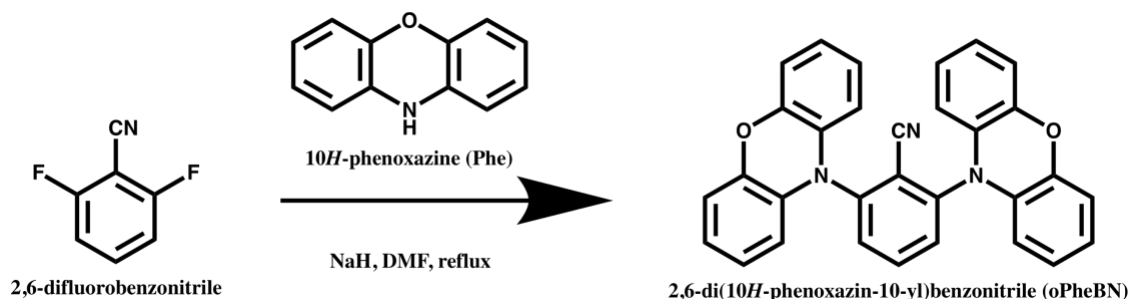


Scheme 2-4. Synthesis of mCzBN.

Under argon atmosphere, 9H-carbazole (0.502 g, 3 mmol) in dehydrated N,N-dimethylformamide (10 ml) was added dropwise into a dehydrated N,N-dimethylformamide (10 ml) solution containing t-BuOK (0.449 g, 4 mmol Mw=112.21) for 15 min and stirred for 3 h. Then, 3,5-difluorobenzonitrile (0.181 g, 1.3 mmol), in dehydrated N,N-dimethylformamide (5 ml) was added dropwise for 15 min. Then the solution was stirred for 10h at 80 °C. The reaction was quenched by adding 300 ml water and the white precipitate was filtered and dried in

vacuum. The crude product was purified by reprecipitation with acetone and the white product was obtained as a powder (0.405 g, 72% yield).  $^1\text{H}$  NMR (400 MHz,  $\text{DMSO-}d_6$ )  $\delta$  8.38 (d,  $J=1.9$  Hz, 2H), 8.29 – 8.23 (m, 5H), 7.63 (d,  $J=8.2$  Hz, 4H), 7.49 (ddd,  $J=8.4, 7.2, 1.3$  Hz, 4H), 7.36 – 7.31 (m, 4H).

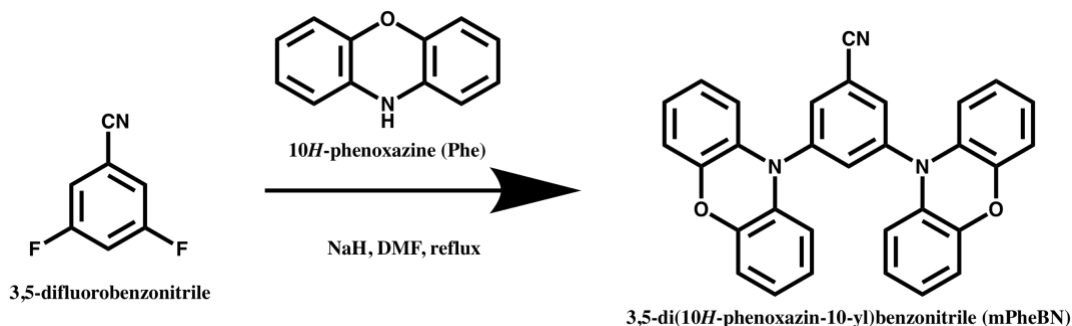
**2,6-Di(10*H*-phenoxazin-10-yl)benzotrile (oPheBN):**



Scheme 2-5. Synthesis of oPheBN.

Mineral oil dispersion of sodium hydride (60 %, 0.23 g) was washed with hexane three times. After vacuum drying for 2 h, it was stirred in DMF (25 mL) under an argon atmosphere. After 10 min, phenoxazine (0.8 g, 4.4 mmol) was added followed by addition of 2,6-difluorobenzonitrile (0.29 g, 2.1 mmol). The mixture was stirred for 10 h and poured into iced water and filtered. After filtration, the greenish product was obtained as a powder (0.80 g, 82 % yield). The crude product was further purified by sublimation.  $^1\text{H}$  NMR (500 MHz,  $\text{CDCl}_3$ ):  $\delta=8.08$  (t,  $J=8.0$  Hz, 1 H), 7.69 (d,  $J=8.5$  Hz, 2 H), 6.78–6.68 (m, 12 H), 5.91 ppm (d,  $J=9$  Hz, 4 H);  $^{13}\text{C}$  NMR (125 MHz,  $\text{CDCl}_3$ ):  $\delta=145.3, 144.2, 137.7, 133.1, 132.8, 123.7, 123.0, 116.5, 113.1, 112.8$  ppm; HRMS (FAB):  $m/z$  calcd for  $\text{C}_{31}\text{H}_{19}\text{N}_3\text{O}_2$ : 465.1477; found: 465.1477.

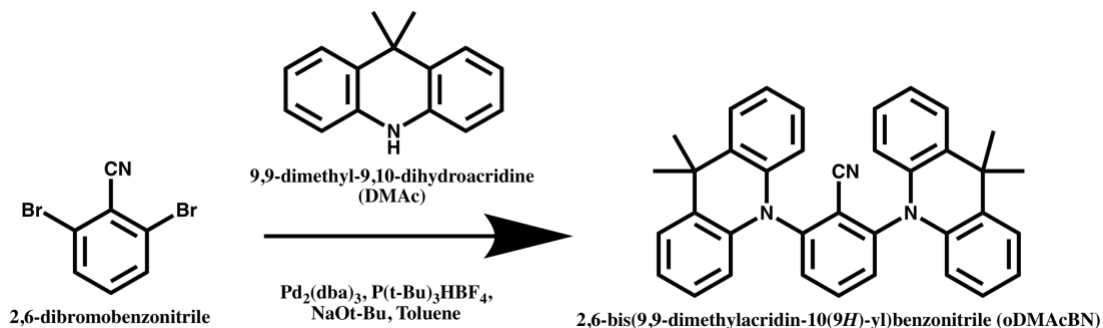
### 3,5-Di(10*H*-phenoxazin-10-yl)benzonitrile (mPheBN):



Scheme 2-6. Synthesis of mPheBN.

*mPheBN* was synthesized according to the synthetic procedure used for *oPheBN* (0.70 g, 72 % yield). The final product was further purified by sublimation. <sup>1</sup>H NMR (500 MHz, CDCl<sub>3</sub>): δ=7.77 (m, 2 H), 7.70 (m, 1 H), 6.75–6.67 (m, 12 H), 5.98 ppm (d, *J*=7.5 Hz, 4 H); <sup>13</sup>C NMR (125 MHz, CDCl<sub>3</sub>): δ=144.3, 143.7, 139.4, 134.6, 133.2, 123.7, 123.0, 118.0, 116.9, 116.4, 113.5 ppm; HRMS (FAB): *m/z* calcd for C<sub>31</sub>H<sub>19</sub>N<sub>3</sub>O<sub>2</sub>: 465.1477; found: 465.1477.

### 2,6-Di(9,9-dimethylacridane)benzonitrile (oDMAcBN):



Scheme 2-7. Synthesis of oDMAcBN.

A mixture of 2,6-dibromobenzonitrile (0.100 g, 0.383 mmol), 9,9-dimethylacridane (0.185 g, 0.882 mmol, Mw=209.29), tris(dibenzylideneacetone)dipalladium (0.0915 g, 0.100

mmol, Mw=915.72), tri-*tert*-butylphosphonium tetrafluoroborate (0.1907 g, 0.657 mmol, Mw=290.13) and sodium *tert*-butoxide (0.1263 g, 1.3145 mmol, Mw=96.10) in 8 ml of toluene was heated and stirred at 110°C. After refluxing for 24 hours, the resulting mixture was diluted by toluene, and then filtered through Celite. The crude product was dried *in vacuo* and then purified by reprecipitation. More purification has been done using column machine chromatography (silica gel, CH<sub>2</sub>Cl<sub>2</sub>: *n*-hexane=1:1 v/v) to yield the title compound as a yellow solid (0.021g, 11%). <sup>1</sup>H NMR (400 MHz, Chloroform-*d*) δ 8.14 (t, *J* = 8.0 Hz, 1H), 7.73 (d, *J*=8.1 Hz, 2H), 7.50 (dd, *J*=7.7, 1.6 Hz, 4H), 7.07 (td, *J*=7.7, 1.6 Hz, 4H), 7.00 (td, *J*=7.5, 1.3 Hz, 4H), 6.29 (dd, *J*=8.0, 1.3 Hz, 4H), 1.70 (s, 12H).

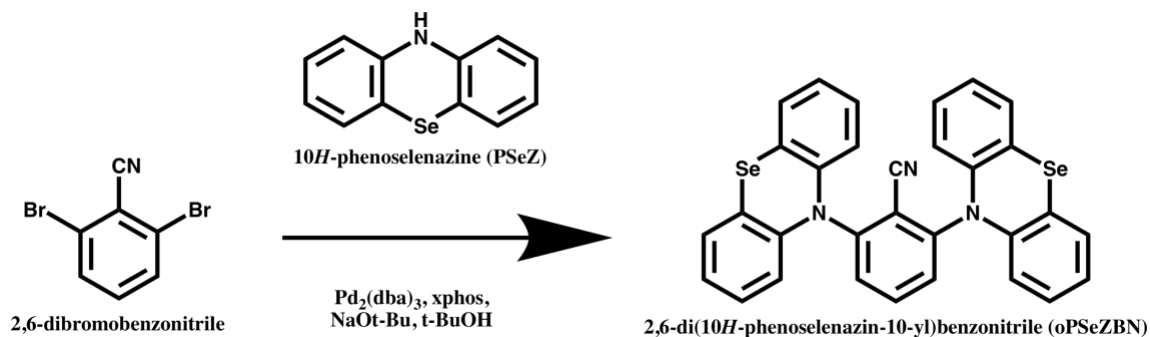
#### 10H-Phenoselenazine (PSeZ):



Scheme 2-8. Synthesis of 10H-Phenoselenazine.

To a mixture of selenium (1.00 g, 12.79 mmol) in sulfolane (5 mL) diphenylamine (2 eq. 25.58 mmol, 4.329g), selenium dioxide (1.20 eq., 15.348mmol, 1.703g) and iodine (0.1 eq., 1.279 mmol, 0.3246g) were added. The reaction mixture was sealed in a 100 mL pressure vial with a Teflon bushing and placed in an oil bath at 150 °C for 5 hours. Upon completion, the reaction mixture was cooled to room temperature and was filtered through a Celite plug using dichloromethane (DCM). The solvent was evaporated *in vacuo* and recrystallized using EtOH and then subsequently purified twice or thrice by flash chromatography using *n*-hexane: ethyl acetate 5:1 to yield a yellow solid (1.01 g, 33%). <sup>1</sup>H NMR (400 MHz, DMSO-*d*<sub>6</sub>) δ 8.58 (s, 1H), 7.11 – 7.00 (m, 4H), 6.79 – 6.73 (m, 4H).

### 2,6-Di(10H-Phenoselenazine )benzonitrile (oPSeZBN):



Scheme 2-9. Synthesis of oPSeZBN.

2,6-Dibromobenzonitrile (0.0783 g, 0.3 mmol) and PSeZ (0.1772 g, 0.72 mmol) were dissolved in anhydrous toluene (20 mL) and the solution degassed by bubbling through argon for 15 min. To the solution was added tert-butanol (1.5 mL), Pd<sub>2</sub>(dba)<sub>3</sub> (0.010 g, 3 mol%) and 2-Dicyclohexylphosphino-2',4',6'-triisopropylbiphenyl (xphos) (0.018 g, 10 mol%) and degassing continued for an additional 15 min. Sodium tert-butoxide (0.108 g, 1.12 mmol) was added and the mixture heated at 110 °C under argon for 28 h. Upon cooling to room temperature, water (~150 mL) was added and the organic products extracted into DCM. The solvent was evaporated in vacuo and recrystallized using acetone and then subsequently purified by column chromatography using hexane: ethyl acetate 4:1 to yield a yellow solid (0.10 g, 57%). <sup>1</sup>H NMR (300 MHz, Chloroform-d) δ 8.01 (s, 1H), 7.80 (d, J=8.0 Hz, 2H), 6.97 (dt, J=22.7, 7.3 Hz, 11H), 6.48 (d, J=8.2 Hz, 5H).

### 2.2.3 Computational Method

First, we performed quantum mechanical electronic structure calculations, using Gaussian 16, for the molecules that we have synthesized in this work and for all the molecules

listed in Table 2-1, which have been developed and experimentally characterized by other investigators, as described in the literature. We endeavor to better understand the nature and role of the frontier orbitals. We used B3LYP and CAM-B3LYP functional with 6-31G(d,p) basis set. Previous studies have shown hybrid functionals like B3LYP with low HF% underestimate the vertical transition energies for TADF molecules. However, functionals like CAM-B3LYP with high HF% can obtain quite accurate results for TADF compounds with high charge transfer characteristic. Here we have used both of the functionals for the sake of comparison. The CAM-B3LYP computational results have been presented in this chapter and B3LYP in the appendix A (Supporting Information for Chapter 2).

The optimized ground state geometries ( $S_0$ ) are obtained followed by an analysis of normal modes of atomic motion to confirm the stability of the optimized structures. The electronic populations of the HOMO and the LUMO orbitals are calculated to show the position of electron populations. Time-dependent density functional theory (TD-DFT) are carried out to study the excited state properties, including transition compositions, vertical excitation energies, nature of the states, and oscillator strength. Furthermore, natural transition orbitals (NTOs) are calculated using TD-DFT to analyze the electronic configuration of the low-lying singlet and triplet states. The effect of solvent was incorporate by self-consistent reaction field method using polarizable continuum model (PCM) as implemented in Gaussian 16.

To quantify the charge transfer characteristics of the excitations, i.e., the percentage of CT vs. LE states, we determined the degree of overlap between the natural transition orbitals before and after electron migration, which are closely delineated by the HOMO and LUMO, respectively. Essentially, the lower the amount of overlap, the larger the separation of the center of charge when electrons transition between HOMO and LUMO, and hence, the more substantial

is the charge transfer. HOMO-LUMO overlap integrals are calculated using multiwfn package for obtaining a CT amount from the donor to the acceptor.

## 2.3 Results and Discussion

To identify the key factor that determines the emission bandwidth of TADF emitters, we review the pertinent literature, summarized in Table 2-1, include several reported compounds in our computational analysis,<sup>20,23</sup> and expand our investigation with a targeted series of new molecules. In 2016, Chen et al. proposed rotational constraint as an effective strategy to improve color purity, based on comparing the emission characteristics of two TADF molecules, mPTC and oPTC (compounds **1** and **2** in Table 2-1).<sup>20</sup> Of these, mPTC has the larger rotational barrier due to meta-placement of two additional phenyl groups on the benzonitrile acceptor, and it indeed shows a narrower emission band (FWHM = 86 nm) compared to oPTC (FWHM = 97 nm). However, this difference in FWHM is small, especially when expressed in terms of energies, i.e., 0.442 and 0.469 eV for mPTC and oPTC, respectively. Moreover, our calculations show that changing the phenyl substitution position from ortho (oPTC) to meta (mPTC) decreases the charge transfer characteristics of the molecule, since the phenyl groups become less involved in the LUMO orbital, which also results in a narrower emission spectrum. The HOMO-LUMO overlap coefficients for mPTC and oPTC are 0.2531 and 0.1975, respectively. Therefore, mPTC is equally expected to have a narrower emission spectrum based on its weaker charge transfer character. Hence, whether the rotation restriction is really responsible for the narrower emission of mPTC is ambiguous.

The emission band of compound **3** in Table 2.1 is narrower than that of compound **4**.<sup>25</sup> The authors imply that this is because the rotation between the donor and acceptor group about the C-C bond is prevented for compound **3**. However, they did not provide any computational or



experimental proof for this hypothesis. Since CH $\cdots$ N hydrogen bonding is present in both compounds, a comparable restricting effect should ensue. Hence, we expect similar torsional potential energy barriers for the rotation between the donor and acceptor groups in both compounds. In the series of compounds **5-12** in Table 2.1,<sup>26,27</sup> the emission spectra become narrower as the side chains become bulkier, from hydrogen, methyl, to the isopropyl group. Here as well, the authors attribute the sharper emission spectra to the increased rotational barrier imposed by steric hindrance. However, converting the FWHM from nm to eV reveals that the FWHM are essentially the same, or even the reverse trend is observed. Compounds **13** and **14**<sup>24</sup> have about the same FWHM, even though rotation should be more suppressed in **14**, as an additional methyl group is attached to the acceptor. Compounds **15-18**, in which the R group is H, Me, t-Bu, and MeO, respectively, have the same rotational barrier since the side group does not affect the rotation of the carbazole donor. While the FWHM of these compounds are largely different on the wavelength scale, once convert to energies, the FWHM values are almost the same (0.41, 0.40, 0.41, and 0.44 eV), which provides credence to the choice of energy as the proper spectral scale. Furthermore, our DFT calculations yield similar HOMO/LUMO overlap coefficients for these four molecules ( $\sim 0.31$ ), essentially unaffected by the extra R(=Me, t-Bu, and MeO) groups. In compound **19**,<sup>28</sup> the two phenyl rings are connected to each other, making it harder for this bulkier group to rotate than in compound **20**, where the phenyl rings can rotate almost freely. Interestingly, the rigidified compound **19** has a broader FWHM than compound **20** (96 nm and 86 nm, respectively). However, converting the FWHM to eV shows that both molecules have about the same emission bandwidth, suggesting that molecular rotation restriction negligibly affects the FWHM. These observations are in line with our hypothesis that charge transfer characteristics dominantly affects the color purity of TADF emitters.

Finally, Hatakeyama et al.<sup>29,30</sup> recently reported organoboron-based planar TADF emitters with small  $\Delta E_{ST}$  and excellent color purity. Their design separates HOMO and LUMO based on the multiple resonance effect, without D-A alternation. They exhibit ultrapure TADF color with a FWHM of 28 nm. Following their novel molecular design, Adachi et. al.<sup>31</sup> report another TADF emitter with a FWHM of 34 nm. These sharp TADF emitters all show localized HOMO and LUMO orbitals and their first singlet state ( $S_1$ ) has LE characteristic rather than CT.

To verify our conjecture, we designed and characterized a series of donor-acceptor twisted intramolecular charge transfer (TICT) molecules, in which the charge transfer character and ability to impede intramolecular rotation is systematically varied (Figure 2-2). Benzonitrile (BN) serves as the acceptor common to all molecules, and the donors include diphenylamine (DPA), carbazole (Cz), phenoxazine (Phe), 9,10-dihydro-9,9-dimethyl-acridine (DMAc), and phenoselenazine (PSeZ).<sup>32,33</sup> oPheBN and mPheBN have previously been investigated in our group,<sup>34-36</sup> and oCzBN and mCzBN have been reported in the literature;<sup>23,37,38</sup> all other molecules are synthesized and characterized for the first time in this work. Using electronic structure calculations, we explore the HOMO and LUMO electron densities and spatial overlap of transition orbitals before and after electron migration. The amount of charge transfer can be assessed based on the degree of spatial overlap between the HOMO and LUMO orbitals. Therefore, to affect the charge transfer we must control the frontier orbitals of a molecule's ground and excited states.

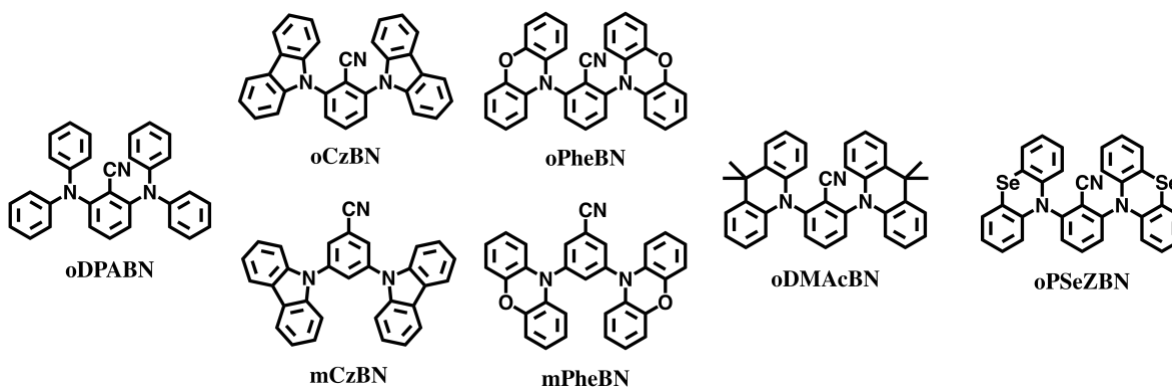


Figure 2-2. D-A-D TADF molecules investigated in this study.

As shown in Figure 2-3, in general the HOMO and LUMO orbital overlap gradually decreases as the donor strength increases in this series except for oDPABN and oCzBN because diphenylamine is known to be a stronger donor than carbazole. Even though diphenylamine is a stronger donor, carbazole induces a stronger HOMO and LUMO separation compare to diphenylamine. We believe that disconnected two phenyl rings differently contribute to HOMO electron density than the fused ring donors. Since carbazole is a fused planar ring structure, the dihedral angle between carbazole and the cyanophenyl acceptor is almost 90 degree. This prevents the conjugation of the HOMO orbital from extending to the acceptor, and thereby the HOMO orbital is present mainly on the carbazole group. On the contrary, the two phenyl rings are not connected in diphenylamine, and the HOMO orbital is extended to the acceptor unit, resulting in a larger HOMO and LUMO overlap, despite diphenylamine's stronger donor strength.

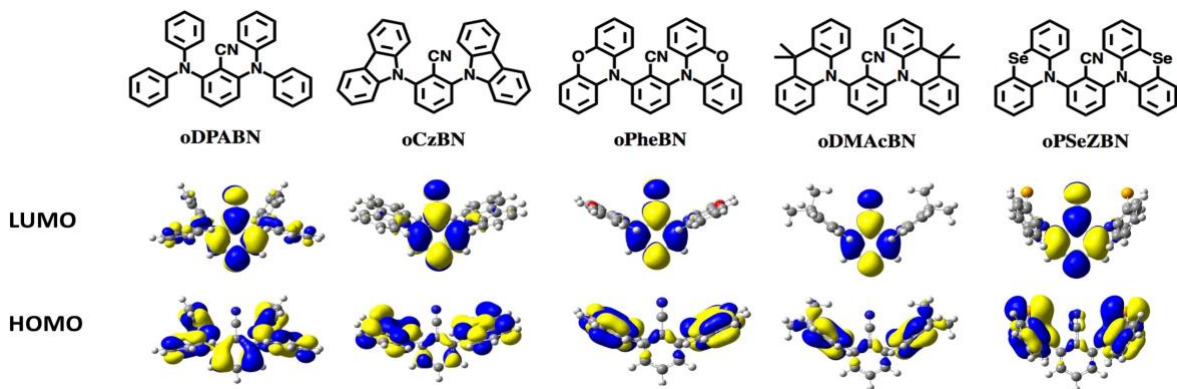


Figure 2-3. Chemical structures and calculated distributions of HOMOs and LUMOs using CAM-B3LYP/6-31g(d,p) level in vacuum. Stronger donor results in more separated HOMO and LUMO.

Furthermore, we have measured the photoluminescence spectra of oDPABN and oCzBN in various solvents and calculated the degree of red-shifted photoluminescence by solvatochromism. As can be seen in Figures S3 and S4 in supporting information, the emission peak of oDPABN shifts from 420 nm in hexane (less polar solvent) to 458 nm in methanol (more polar solvent), whereas that of oCzBN shifts from 381 nm in hexane to 449 nm in methanol. Accordingly, oCzBN shows a more remarkable red shift with increasing solvent polarity. This is in good agreement with the CT character of the emitting state where a large solvatochromic shift indicates a prominent CT state,<sup>39-42</sup> suggesting a stronger CT character in oCzBN than in oDPABN.

With the least HOMO-LUMO overlap, oPSeZBN has the strongest charge transfer character. The normalized HOMO-LUMO overlap integrals yields a coefficient that quantifies the charge-transfer character of a molecule. These overlap coefficients are listed in Table 2-2 along with a summary comparison of computational and experimental results. Ultraviolet-visible absorption and photoluminescence spectra of the investigated molecules that were measured in toluene solutions at room temperature are also depicted in Appendix A (Figure A-1 and A-2).

Table 2-2. Summary of key computational and experimental results. Energy of first singlet ( $S_1$ ), oscillator strength ( $f$ ) energy of first triplet states ( $T_1$ ), and energy gap between  $S_1$  and  $T_1$  ( $\Delta E_{ST}$ ) were calculated using DFT at the B3LYP/6-31g(d,p) level in vacuum; overlap integral between HOMO and LUMO were calculated at the CAM-B3LYP/6-31g(d,p) level using multiwfn,<sup>43</sup> the experimental  $\Delta E_{ST}$  and emission FWHM were measured in  $10^{-5}$  M toluene solution at 25 °C

Compound	Electron Donor	$S_1^{[a]}$ (eV)	$f^{[a]}$	$T_1^{[a]}$ (eV)	$\Delta E_{ST}^{[a]}$ (eV)	$\Delta E_{ST}^{[b, c]}$ (eV)	H/L <sup>[a]</sup> overlap	FWHM <sup>[b]</sup> (nm)	FWHM <sup>[b]</sup> (eV)	
1	oDPABN	Diphenylamine	3.15	0.1863	2.81	0.34	0.313	0.4912	45.7	0.296
2	oCzBN	Carbazole	3.08	0.0856	2.95	0.13	0.192	0.3097	51.8	0.381
3	oPheBN	Phenoxazine	2.21	0.0000	2.19	0.02	0.00	0.2234	105.7	0.443
4	oDMAcBN	Acridine	2.50	0.0000	2.48	0.02	0.00	0.2072	79.9	0.422
5	oDPSeZBN	Phenoselenazine	2.63	0.0000	2.62	0.01	0.00	0.1795	119.1	0.473

[a] Computational results

[b] Experimental results

[c]  $\Delta E_{ST}$  has been measured by comparing the fluorescence and phosphorescence spectra at liquid nitrogen temperature.

As expected, the calculated  $\Delta E_{ST}$  decreases as the donor strength increases. Similarly, the lack of orbital overlap, when spatially separating the HOMO and LUMO involved in the excitation reduces mixing of electronic wavefunctions, e.g.  $\langle n|\pi^* \rangle$  or CT state, results in a small  $\Delta E_{ST}$  but also weak oscillator strength. Therefore, oDPABN, with the largest overlap between the orbitals involved in the  $S_1$  transition, has the highest oscillator strength. This value decreases in this series as we increase the donor strength, while the HOMO-LUMO overlap coefficient decreases. The experimental  $\Delta E_{ST}$  values are consistent with the calculated  $\Delta E_{ST}$ , suggesting that our DFT model works well for this system.

Since the  $S_1$  transition in these molecules are >97% HOMO $\rightarrow$ LUMO (Table A-2 Appendix A), the HOMO/LUMO overlap coefficient has been used for  $S_1$  transition. However, natural transition orbitals (NTOs) are calculated as well by using TD-DFT to analyze the electronic configuration of the  $S_1$  state. In Figure A-6 and Table A-2 in Appendix A one can see HONTO (highest occupied natural transition orbital) and LUNTO (lowest unoccupied natural transition orbital) distributions and overlap extents of the first singlet ( $S_1$ ) state for exciton

transformation. The HOMO/LUMO overlap coefficient has also been given for comparison. As evident, the HONTO/LUNTO overlap coefficient is almost the same as HOMO/LUMO overlap. Therefore, the HOMO/LUMO overlap coefficient has been used for the analysis in this work.

Significant emission broadening is observed as the charge-transfer character increases from DPA to PSeZ, thus reducing the overlap between HOMO and LUMO (Figure 3 & Table 2). In this series, the substitution position remains unchanged; only the donor strength is varied, which is accompanied by a change in dihedral angle. As evident in Figure 2-4, we observe a linear correlation between FWHM and the HOMO-LUMO overlap coefficient.

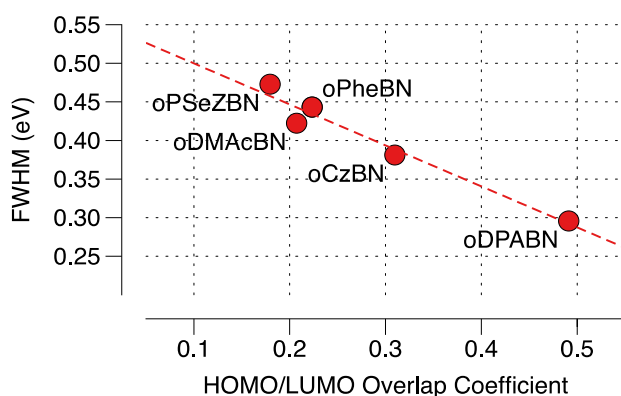


Figure 2-4. Correlation between measured FWHM and calculated HOMO/LUMO overlap.

If rotation of the donor group made the emission broader, one would expect that oDPABN has a broader bandwidth than oCzBN. In the latter, the two phenyl rings in the carbazole unit are connected to each other, making it harder for this bulkier carbazole to rotate. By contrast, the phenyl rings on the diphenylamine group can rotate almost freely, as substantiated by the low torsional potential energy barrier shown in Figure 2-5. However, the TADF emission spectrum of oDPABN is much sharper than that of oCzBN; 0.296 eV compared to 0.381 eV. oCzBN has stronger charge transfer character (lower HOMO-LUMO overlap, see Table 2-2), which results in a broader emission bandwidth compared to oDPABN. This is strong

evidence that charge transfer character controls the emission bandwidth of TADF compounds, while rotation has a negligible effect.

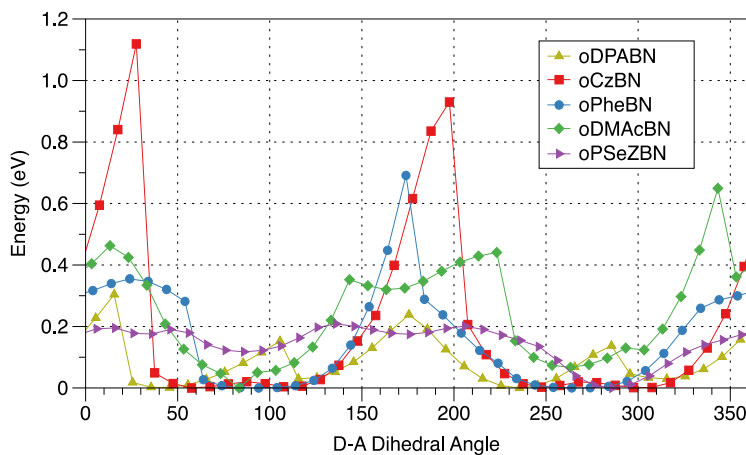


Figure 2-5. Torsional potential energy of investigated molecules (ortho position) as a function of donor-acceptor dihedral angle from DFT calculations at the CAM-B3LYP/6-31g(d,p) level.

We also synthesized the meta version of the carbazole (mCzBN) and phenoxazine (mPheBN) compounds. The meta position is farther away from the cyano group than the ortho position. Ortho and meta substituted molecules have about the same charge transfer characteristic, since their donor strength is the same; only the position of the donor is different. We analyzed the optimized molecular structures in both  $S_0$  and  $S_1$  states, using quantum mechanical calculations (Figure 2-6(a)). As designed, oPheBN and mPheBN adopt nearly orthogonal D-A-D conformations between the Phe and the BN units, with dihedral angles of  $93.9^\circ$  and  $99.6^\circ$ , respectively, in the  $S_0$  state, while these dihedral angles are  $87.3^\circ$  and  $84.1^\circ$  in the  $S_1$  state. With  $6.6^\circ$  compared to  $15.5^\circ$ , geometric differences between the ground and excited states are smaller for oPheBN than for mPheBN. Furthermore, quantum mechanical calculations reveal that mPheBN has a much lower energy barrier for torsional motion between donor (Phe) and acceptor (BN) than oPheBN (Figure 2-6(b)). Accordingly, oPheBN is rigid upon photoexcitation due to the steric hindrance imposed by the cyano group. Conversely, mPheBN is more flexible with the Phe groups at meta positions, where their rotation is less encumbered by

the cyano group. The same behavior is observed for oCzBN and mCzBN (Figure 2-6(b)). The torsional potential barrier for carbazole compounds are higher than phenoxazine because the carbazole group has a five-membered ring that cannot bend out of plane, while the central ring in phenoxazine bends to lower the molecule's energy when the dihedral angle is raised.

The HOMO-LUMO overlap coefficients for oPheBN and mPheBN are 0.2234 and 0.2304, which is why they have similar charge transfer character. Despite the different rotational restriction caused by the cyano group in oPheBN, both exhibit about the same FWHM: 0.443 eV for oPheBN and 0.459 eV for mPheBN. Also, they both exhibit minimal emission broadening ( $<0.005$  eV) upon thermally activating rotation the temperature range between  $5^{\circ}\text{C}$  and  $80^{\circ}\text{C}$  (Figure 2-6(c)). Since the rotational barrier is small for mPheBN, increasing the temperature should provide the Phe group with enough energy to overcome the rotational barrier and broaden the emission. However, this is not the case. oCzBN and mCzBN exhibit the same trend (Figure 2-6(b,c)). The torsional barrier for oCzBN is higher than for mCzBN, because of the interference with the cyano group. Similar to the phenoxazines, both show minimal emission broadening upon raising the temperature. This strongly supports that D-A rotation negligibly affects the emission bandwidth of TADF compounds, while charge transfer plays the major role.



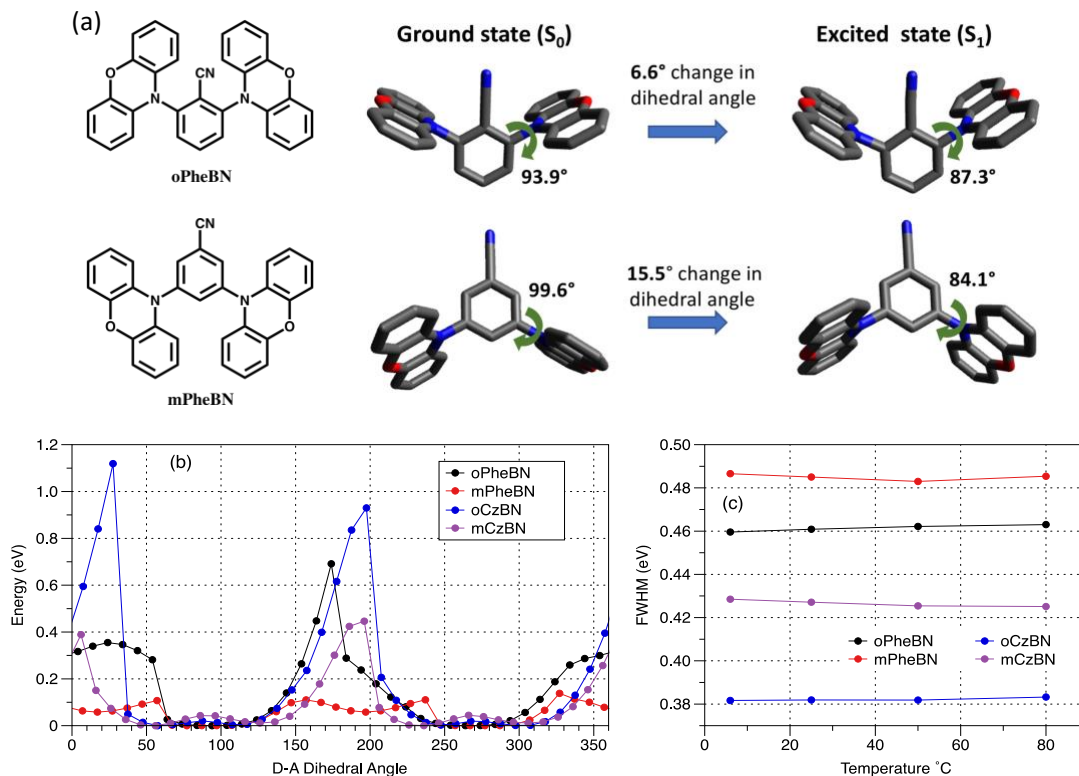


Figure 2-6. Chemical structures of oPheBN and mPheBN and the differences in the differences in the optimized geometries between the ground and first singlet excited states, hydrogens are not shown for clarity. oPheBN shows 6.6° change in the dihedral angles between the donor and acceptor, however, mPheBN shows a higher dihedral angle change of 15.5°. (b) Torsional potential energy of of oPheBN (black), mPheBN (red), oCzBN (blue), and mCzBN (purple) as a function of donor-acceptor dihedral angle from DFT calculations at the CAM-B3LYP/6-31G(d,p) level. (c) Temperature dependence FWHM of oPheBN (black), mPheBN (red), oCzBN (blue), and mCzBN (purple) in 10<sup>-5</sup> M toluene solution (The FWHM discrepancy between (c) and table 2-1 is because different fluorimeters were used, but measurements are consistent within each data set).

We also measured the steady state photoluminescence spectra of oCzBN in various solvents ranging from hexane (lowest polarity) to methanol (highest polarity). Positive solvatochromism has been observed as expected. The emission peak red shifts from 381 nm in hexane to 449 nm in methanol (Figure A-4(a) Appendix A). Significant emission broadening is observed as the polarity of the solvent increases. We have also converted the abscissa unit from nm to eV (Figure A-4(b) Appendix A). Converting the FWHM to eV reveals that the FWHM still gets broader as the solvents polarity increases (Figure A-5 Appendix A). In other words, the same compound, oCzBN, shows different FWHM depending on the solvent choice. We used the polarizable continuum model (PCM) at CAM-B3LYP/6-31G(d,p) to incorporate the solvent

effect. As it is evident in Table A-1 (see Appendix A), our DFT results show that the HOMO-LUMO overlap coefficient of oCzBN decreases as the polarity of the solvent increases. This is exactly the same trend that we observed from ortho substituted molecules in Figure 2-4.

However, we believe that the PCM model underestimates the solvent effect and changing the polarity of solvent would have resulted in a noteworthy change in the HOMO-LUMO overlap coefficients, making the overlap coefficients of oCzBN in various solvents are close to each other.

Having observed the drastic emission broadening by increasing charge transfer character, and that restricting molecular rotational has a minimal effect on the color purity of TADF emitters, LE transitions seem to be the only effective way to improve the color purity. However, molecules with LE emitter states tend to have rather large  $\Delta E_{ST}$ , making up-conversion challenging. As a result, TADF becomes a matter of optimizing molecular designs so that  $\Delta E_{ST}$  is small enough for efficient TADF and the emission is still sharp.

Separating HOMO and LUMO via multiple resonance effect, suggested by Hatakeyama et al.,<sup>29,30</sup> which results in an LE state, is so far the most promising route for high color purity TADF emission. The molecular resonance TADF molecules presented by Hatakeyama et al, DABNA1 and DABNA2, have the HOMO/LUMO overlap coefficient of 0.6038 and 0.5869, respectively (calculation done in this work; using B3LYP/6-31G(d,p)), implying their LE characteristics. As a matter of fact, they have a higher LE characteristic than TADF emitters with weak donors (like oDPABN), narrowing FWHM as small as 14 nm. However, the carbon-boron bond in these compounds causes poor stability, resulting in significant roll-off in OLED applications. Moreover, the work by Dias et. al.,<sup>44</sup> has shown that even with  $\Delta E_{ST}$  as large as 0.3 eV, 100% TADF efficiency is achievable by introducing a  $^3n\pi^*$  triplet state. Also,

Higginbotham et. al.<sup>45</sup> were able to increase the rISC rate to a near 2 orders of magnitude by mixing the  $n\pi^*$  with the donor  $\pi$  orbitals, whereas the singlet-triplet splitting,  $\Delta E_{ST}$ , remains unaffected. Therefore, future efforts are directed towards designing TADF molecules with weak donors, resulting in higher HOMO-LUMO overlap and a narrower emission bandwidth. A presence of the  $^3n\pi^*$  triplet state is necessary to enhance rISC and compensate for the relatively large singlet-triplet energy gap.

## 2.4 Conclusions

In summary, we designed and synthesized a series of D-A-D type TADF emitters and altered the charge transfer characteristics and rotational restrictions in these molecules. Compounds with the same rotational barrier show a large increase in FWHM when the charge transfer character gets stronger. However, even with increased rotational restrictions caused by the cyano group, emitters showed minimal change in their FWHM. If increased restriction of the molecular rotation were effective in improving color purity, one would expect broader emission spectra upon increasing the temperature, since the molecules gain energy to overcome the rotation barrier. However, temperature has minimal effect on color purity. These results, along with examining data for various compounds described in the literature, strongly suggest that molecular rotation restriction negligibly affects the FWHM and that the intrinsic TADF emission bandwidth is mainly controlled by the charge transfer character. Our combined experimental and computational results provide understanding about rational molecular design of TADF molecules with a narrow emission spectrum.

## 2.5 References

(1) Baldo, M. A.; O'Brien, D. F.; Thompson, M. E.; Forrest, S. R. Excitonic Singlet-Triplet Ratio in a Semiconducting Organic Thin Film. *Phys. Rev. B* **1999**, *60*, 14422.

- (2) Segal, M.; Baldo, M. A.; Holmes, R. J.; Forrest, S. R.; Soos, Z. G. Excitonic Singlet-Triplet Ratios in Molecular and Polymeric Organic Materials. *Phys. Rev. B* **2003**, *68*, 075211.
- (3) Tsutsui, T. Progress in Electroluminescent Devices Using Molecular Thin Films. *MRS Bull.* **1997**, *22*, 39-45.
- (4) Wallikewitz, B. H.; Kabra, D.; Gélinas, S.; Friend, R. H. Triplet Dynamics in Fluorescent Polymer Light-Emitting Diodes. *Phys. Rev. B* **2012**, *85*, 045209.
- (5) Adachi, C.; Baldo, M. A.; Thompson, M. E.; Forrest, S. R. Nearly 100% Internal Phosphorescence Efficiency in an Organic Light-Emitting Device. *J. Appl. Phys.* **2001**, *90*, 5048-5051.
- (6) Shizu, K.; Noda, H.; Tanaka, H.; Taneda, M.; Uejima, M.; Sato, T.; Tanaka, K.; Kaji, H.; Adachi, C. Highly Efficient Blue Electroluminescence Using Delayed-Fluorescence Emitters With Large Overlap Density Between Luminescent and Ground States. *J. Phys. Chem. C* **2015**, *119*, 26283-26289.
- (7) Yook, K. S.; Lee, J. Y. Organic Materials for Deep Blue Phosphorescent Organic Light-emitting Diodes. *Adv. Mater.* **2012**, *24*, 3169.
- (8) Song, B.; Shao, W.; Jung, J.; Yoon, S.-J.; Kim, J. Organic Light-Emitting Diode Employing Metal-Free Organic Phosphor. *ACS Appl. Mater. Interfaces* **2020**, *12*, 6137-6143.
- (9) Kido, J.; Okamoto, Y. Organo Lanthanide Metal Complexes for Electroluminescent Materials. *Chem. Rev.* **2002**, *102*, 2357-2368.
- (10) Goushi, K.; Yoshida, K.; Sato, K.; Adachi, C. Organic Light-Emitting Diodes Employing Efficient Reverse Intersystem Crossing for Triplet-to-singlet State Conversion. *Nat. Photonics* **2012**, *6*, 253 - 258.
- (11) Sun, J. W.; Lee, J. H.; Moon, C. K.; Kim, K. H.; Shin, H.; Kim, J. J. A Fluorescent Organic Light-emitting Diode With 30% External Quantum Efficiency. *Adv. Mater.* **2014**, *26*, 5684.
- (12) Uoyama, H.; Goushi, K.; Shizu, K.; Nomura, H.; Adachi, C. Highly Efficient Organic Light-Emitting Diodes From Delayed Fluorescence. *Nature* **2012**, *492*, 234-238.
- (13) Im, Y.; Kim, M.; Cho, Y. J.; Seo, J.-A.; Yook, K. S.; Lee, J. Y. Molecular Design Strategy of Organic Thermally Activated Delayed Fluorescence Emitters. *Chem. Mater.* **2017**, *29*, 1946-1963.
- (14) Sarma, M.; Wong, K.-T. Exciplex: An Intermolecular Charge-Transfer Approach for Tadf. *ACS Appl. Mater. Interfaces* **2018**, *10*, 19279-19304.
- (15) Nakanotani, H.; Higuchi, T.; Furukawa, T.; Masui, K.; Morimoto, K.; Numata, M.; Tanaka, H.; Sagara, Y.; Yasuda, T.; Adachi, C. High-Efficiency Organic Light-Emitting Diodes With Fluorescent Emitters. *Nat. Commun.* **2014**, *5*, 1-7.
- (16) Zhang, D.; Duan, L.; Li, C.; Li, Y.; Li, H.; Zhang, D.; Qiu, Y. High-efficiency Fluorescent Organic Light-emitting Devices Using Sensitizing Hosts With a Small Singlet-Triplet Exchange Energy. *Adv. Mater.* **2014**, *26*, 5050-5055.
- (17) Endo, A.; Ogasawara, M.; Takahashi, A.; Yokoyama, D.; Kato, Y.; Adachi, C. Thermally Activated Delayed Fluorescence From Sn<sup>4+</sup>-Porphyrin Complexes and Their Application to

Organic Light Emitting Diodes—a Novel Mechanism for Electroluminescence. *Adv. Mater.* **2009**, *21*, 4802-4806.

(18) Chen, T.; Zheng, L.; Yuan, J.; An, Z.; Chen, R.; Tao, Y.; Li, H.; Xie, X.; Huang, W. Understanding the Control of Singlet-Triplet Splitting for Organic Exciton Manipulating: A Combined Theoretical and Experimental Approach. *Sci. Rep.* **2015**, *5*, 10923.

(19) Rajamalli, P.; Senthilkumar, N.; Gandeepan, P.; Ren-Wu, C.-C.; Lin, H.-W.; Cheng, C.-H. A Method for Reducing the Singlet-Triplet Energy Gaps of Tadf Materials for Improving the Blue Oled Efficiency. *ACS Appl. Mater. Interfaces* **2016**, *8*, 27026-27034.

(20) Chen, D.-Y.; Liu, W.; Zheng, C.-J.; Wang, K.; Li, F.; Tao, S. L.; Ou, X.-M.; Zhang, X.-H. Isomeric Thermally Activated Delayed Fluorescence Emitters for Color Purity-Improved Emission in Organic Light-Emitting Devices. *ACS Appl. Mater. Interfaces* **2016**, *8*, 16791-16798.

(21) Cho, T.-Y.; Lin, C.-L.; Wu, C.-C. Microcavity Two-Unit Tandem Organic Light-Emitting Devices Having a High Efficiency. *Appl. Phys. Lett.* **2006**, *88*, 111106.

(22) Poitras, D.; Kuo, C.-C.; Py, C. Design of High-Contrast Oleds With Microcavity Effect. *Opt. Express* **2008**, *16*, 8003-8015.

(23) Chan, C.; Cui, L.; Kim, J. U.; Nakanotani, H.; Adachi, C. Rational Molecular Design for Deep-blue Thermally Activated Delayed Fluorescence Emitters. *Adv. Funct. Mater.* **2018**, *28*, 1706023.

(24) Noda, H.; Kabe, R.; Adachi, C. Blue Thermally Activated Delayed Fluorescence Molecule Having Acridane and Cyanobenzene Units. *Chem. Lett.* **2016**, *45*, 1463-1466.

(25) Rajamalli, P.; Senthilkumar, N.; Huang, P.-Y.; Ren-Wu, C.-C.; Lin, H.-W.; Cheng, C.-H. New Molecular Design Concurrently Providing Superior Pure Blue, Thermally Activated Delayed Fluorescence and Optical Out-Coupling Efficiencies. *J. Am. Chem. Soc.* **2017**, *139*, 10948-10951.

(26) Ward, J. S.; Nobuyasu, R. S.; Batsanov, A. S.; Data, P.; Monkman, A. P.; Dias, F. B.; Bryce, M. R. The Interplay of Thermally Activated Delayed Fluorescence (Tadf) and Room Temperature Organic Phosphorescence in Sterically-Constrained Donor-Acceptor Charge-Transfer Molecules. *ChemComm* **2016**, *52*, 2612-2615.

(27) Ward, J. S.; Nobuyasu, R. S.; Fox, M. A.; Aguilar, J. A.; Hall, D.; Batsanov, A. S.; Ren, Z.; Dias, F. B.; Bryce, M. R. Impact of Methoxy Substituents on Thermally Activated Delayed Fluorescence and Room-Temperature Phosphorescence in All-Organic Donor-Acceptor Systems. *J. Org. Chem.* **2019**, *84*, 3801-3816.

(28) Kothavale, S.; Chung, W. J.; Lee, J. Y. Rational Molecular Design of Highly Efficient Yellow-Red Thermally Activated Delayed Fluorescent Emitters: A Combined Effect of Auxiliary Fluorine and Rigidified Acceptor Unit. *ACS Appl. Mater. Interfaces* **2020**, *12*, 18730-18738.

(29) Hatakeyama, T.; Shiren, K.; Nakajima, K.; Nomura, S.; Nakatsuka, S.; Kinoshita, K.; Ni, J.; Ono, Y.; Ikuta, T. Ultrapure Blue Thermally Activated Delayed Fluorescence Molecules: Efficient Homo-Lumo Separation By the Multiple Resonance Effect. *Adv. Mater.* **2016**, *28*, 2777-2781.

(30) Matsui, K.; Oda, S.; Yoshiura, K.; Nakajima, K.; Yasuda, N.; Hatakeyama, T. One-Shot Multiple Borylation Toward Bn-Doped Nanographenes. *J. Am. Chem. Soc.* **2018**, *140*, 1195-1198.

- (31) Li, X.; Shi, Y.-Z.; Wang, K.; Zhang, M.; Zheng, C.-J.; Sun, D.-M.; Dai, G.-L.; Fan, X.-C.; Wang, D.-Q.; Liu, W.; Li, Y.-Q.; Yu, J.; Ou, X.-M.; Adachi, C.; Zhang, X.-H. Thermally Activated Delayed Fluorescence Carbonyl Derivatives for Organic Light-Emitting Diodes With Extremely Narrow Full Width At Half-Maximum. *ACS Appl. Mater. Interfaces* **2019**, *11*, 13472-13480.
- (32) de Sa Pereira, D.; Lee, D. R.; Kukhta, N. A.; Lee, K. H.; Kim, C. L.; Batsanov, A. S.; Lee, J. Y.; Monkman, A. P. The Effect of a Heavy Atom on the Radiative Pathways of an Emitter With Dual Conformation, Thermally-Activated Delayed Fluorescence and Room Temperature Phosphorescence. *J. Mater. Chem. C* **2019**, *7*, 10481-10490.
- (33) Tin, G.; Mohamed, T.; Gondora, N.; Beazely, M. A.; Rao, P. P. N. Tricyclic Phenothiazine and Phenoselenazine Derivatives as Potential Multi-Targeting Agents to Treat Alzheimer's Disease. *Med. Chem. Comm.* **2015**, *6*, 1930-1941.
- (34) Ansari, R.; Kim, M.; Yoon, S. J.; Hashemi, D.; Kim, J.; Kieffer, J. A Novel Design of Thermally Activated Delayed Fluorescence Molecules: Experimental and Computational Studies. *Bull. Am. Phys. Soc.* **2018**, *63*,
- (35) Hashemi, D.; Ma, X.; Ansari, R.; Kim, J.; Kieffer, J. Design Principles for the Energy Level Tuning in Donor/acceptor Conjugated Polymers. *Phys. Chem. Chem. Phys.* **2019**, *21*, 789-799.
- (36) Kim, M.; Yoon, S.; Han, S. H.; Ansari, R.; Kieffer, J.; Lee, J. Y.; Kim, J. Molecular Design Approach Managing Molecular Orbital Superposition for High Efficiency Without Color Shift in Thermally Activated Delayed Fluorescent Organic Light-emitting Diodes. *Chem. Eur. J.* **2019**, *25*, 1829-1834.
- (37) Zhang, D.; Cai, M.; Bin, Z.; Zhang, Y.; Zhang, D.; Duan, L. Highly Efficient Blue Thermally Activated Delayed Fluorescent Oleds With Record-Low Driving Voltages Utilizing High Triplet Energy Hosts With Small Singlet-Triplet Splittings. *Chem. Sci* **2016**, *7*, 3355-3363.
- (38) Li, S.-W.; Yu, C.-H.; Ko, C.-L.; Chatterjee, T.; Hung, W.-Y.; Wong, K.-T. Cyanopyrimidine-Carbazole Hybrid Host Materials for High-Efficiency and Low-Efficiency Roll-Off Tadf Oleds. *ACS Appl. Mater. Interfaces* **2018**, *10*, 12930-12936.
- (39) Reichardt, C. Solvatochromic Dyes as Solvent Polarity Indicators. *Chem. Rev.* **1994**, *94*, 2319-2358.
- (40) Carlotti, B.; Elisei, F.; Mazzucato, U.; Spalletti, A. Unusual High Fluorescence of Two Nitro-Distyrylbenzene-like Compounds Induced By Ct Processes Affecting the Fluorescence/intersystem-Crossing Competition. *Phys. Chem. Chem. Phys.* **2015**, *17*, 14740-14749.
- (41) Tanaka, H.; Shizu, K.; Nakanotani, H.; Adachi, C. Twisted Intramolecular Charge Transfer State for Long-Wavelength Thermally Activated Delayed Fluorescence. *Chem. Mater.* **2013**, *25*, 3766-3771.
- (42) Yao, L.; Zhang, S.; Wang, R.; Li, W.; Shen, F.; Yang, B.; Ma, Y. Highly Efficient Near-infrared Organic Light-emitting Diode Based on a Butterfly-shaped Donor-Acceptor Chromophore With Strong Solid-state Fluorescence and a Large Proportion of Radiative Excitons. *Angew. Chem.* **2014**, *53*, 2119-2123.
- (43) Lu, T.; Chen, F. Multiwfn: A Multifunctional Wavefunction Analyzer. *J. Comput. Chem.* **2012**, *33*, 580-592.

- (44) Dias, F. B.; Bourdakos, K. N.; Jankus, V.; Moss, K. C.; Kamtekar, K. T.; Bhalla, V.; Santos, J.; Bryce, M. R.; Monkman, A. P. Triplet Harvesting With 100% Efficiency By Way of Thermally Activated Delayed Fluorescence in Charge Transfer Oled Emitters. *Adv. Mater.* **2013**, *25*, 3707-3714.
- (45) Higginbotham, H. F.; Yi, C.-L.; Monkman, A. P.; Wong, K.-T. Effects of Ortho-Phenyl Substitution on the Risc Rate of D-a Type Tadf Molecules. *J. Phys. Chem. C* **2018**, *122*, 7627-7634.

## Chapter 3 The Role of Halogen Bonding in Metal Free Phosphors

### 3.1 Introduction

Organic light emitting diodes (OLEDs) based on transition metal complexes have been widely investigated over recent decades for their display and solid-state lighting applications.<sup>1,2</sup> Increasing attention is devoted to phosphorescence materials because they can theoretically achieve threefold higher internal quantum efficiency than fluorescent alternatives, by harvesting triplet excitons through intersystem crossing (ISC).<sup>3-6</sup> Most candidates for efficient phosphorescence are based on heavy element complexes because the presence of a heavy atom enhances spin-orbit coupling (SOC) interactions,<sup>7</sup> which, in turn, augment the rate of the spin forbidden process. Although organometallic materials have high quantum efficiency, they require expensive and rare elements such as iridium<sup>8</sup> and platinum.<sup>9</sup> Organometallic materials also exhibit short operating lifetimes due to the degradation of weak and unstable metal-ligand bonds.<sup>10</sup>

Unlike organometallics, purely organic materials are less costly, lighter, readily functionalized, and easily processed. Until now, only a few examples of purely organic molecules with high phosphorescence quantum yield have been reported.<sup>11</sup> This scarcity is related to the fact that purely organic phosphors often exhibit long-lived triplet states that are easily dissipated by vibrational effects before emissive decay can take place.<sup>7</sup> To be competitive with organometallic OLEDs, in purely organic materials one must (1) suppress vibrations that could cause non-radiative decays and (2) elevate intersystem crossing rates by increasing spin-orbit coupling interactions.



To suppress vibrational relaxation of the triplet manifold, several approaches have been pursued. In 2011, Bolton et al.<sup>1</sup> reported enhanced room-temperature phosphorescence (RTP) from pure organic luminogens utilizing mixed crystals and halogen bonding. They designed chromophores that contain triplet-producing aromatic aldehyde and triplet-promoting bromine, and diluted them into the crystal of a bi-halogenated non-carbonyl analogue. One of the crystals they made is 2,5-dihexyloxy-4-bromobenzaldehyde (Figure 3-1). 2,5-dihexyloxy-1,4-dibromobenzene (Br6) is a bi-halogenated analogue to Br6A. Br6 is the same as Br6A, but with a second bromine in place of its aldehyde. The resulting mixed crystals exhibit green phosphorescence with a much higher quantum yield compared to pure Br6A crystals. The ambient phosphorescence quantum yield for the resulting crystal reached 55%. Using this finding, they designed a series of purely organic phosphors that emit blue, green, yellow and orange light. Follow-up studies by Lee et al.<sup>12</sup> explored embedding Br6A molecules into a glassy PMMA polymer film, which exhibits a bright 7.5% phosphorescence quantum yield due to strong halogen bonding between the bromine of Br6A molecules and the oxygen of PMMA polymer. Kwon et al.<sup>13</sup> designed a purely organic RTP system with an amorphous polymer matrix by exploiting strong noncovalent interactions such as hydrogen and halogen bonds, which effectively suppressed vibrational triplet decay and achieved a high phosphorescence quantum yield of 24%.

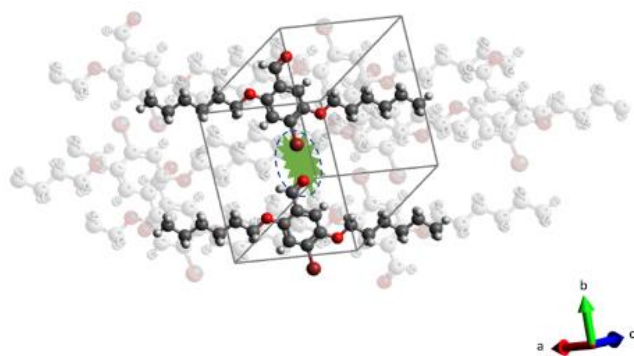


Figure 3-1. The unit cell structure of the Br6A crystal. The a lattice constant is along the x axis, the b lattice constant is along the y axis, and the c lattice constant is along the z axis.

Furthermore, in 2013, Bergamini et al.<sup>14</sup> reported outstanding phosphorescence emission in some environments that impart rigidity. While no phosphorescence is recorded in solution at room temperature, the reported organic molecule shows a very bright phosphorescence in the solid state and at low temperature. In another work, Gao et al.<sup>15–17</sup> developed phosphorescence co-crystals based on halogen and hydrogen bonding. This peculiar behavior of phosphorescence emission in rigid environment is mainly attributed to the suppression of conformational mobility and bond rotation. However, it is unclear to what extent the halogen bonding contributes to efficient room temperature phosphorescence and how different halides affect the emission properties. Therefore, determining their relative influences provides better guidance for future metal-free organic phosphor development.

To promote ISC rates, a common molecular design for metal-free phosphors involves addition of a heavy atom to enhance the SOC interactions, which is either part of,<sup>18, 19</sup> or external to<sup>20–22</sup> the excited molecule. The enhanced SOC interactions promotes spin-forbidden processes including singlet to triplet ISC and radiative decay from the triplet to the singlet ground state. Halides, mostly bromine, have been widely used for the heavy atom effect in metal-free organic phosphors. The heavy atom effect is not the only factor that promotes ISC rates. The presence of

aromatic carbonyl groups can also enhance the ISC process. The generation of the  $n\pi^*$  state in aromatic carbonyls enhances ISC rates from an  $n\pi^*$  singlet state to a  $\pi\pi^*$  triplet state, or vice versa, based on the El-Sayed's rule.<sup>23, 24</sup> Furthermore, a small energy gap between first singlet state and the nearest triplet state also enhances ISC process.

In this chapter, we computationally corroborate the existence of halogen bonding between the halogen and the carbonyl oxygen atoms of adjacent Br6A and other derivatives of this molecule. Strong halogen bonding in Br6A and its derivatives strongly suppresses vibrational dissipation and enables RTP with high quantum yields. This peculiar behavior is attributed to the restriction of bond rotation and conformational mobility of the molecule, which slows down the non-radiative deactivation processes of the phosphorescent excited state. The underlying mechanism of purely organic phosphor candidates is examined by means of a detailed computational study based on density functional theory (DFT) and time dependant DFT (TD-DFT) calculations, revealing the role of halogen bonding. Halogen substituted derivatives of Br6A as well as different Br6A conformations are investigated. The calculated density of states (DOS) is used to substantiate the halogen bonding interaction. This paper is organized as follows: section 2 describes the details of our DFT calculations; in section 3 the results are discussed; a conclusion and summary are given in section 4.

### **3.2 Methodologies**

Four different Br6A systems are studied: isolated molecules, dimers, chains formed along the y-axis, which coincides with the halogen bond direction, and three-dimensional crystals. Isolated molecules are compared with dimers and chains in order to investigate the halogen bonding effect. All calculations are performed using plane-wave DFT as implemented in the Vienna ab-initio simulation package (VASP).<sup>25, 26</sup> The exchange-correlation energy and

potential are described by Perdew, Burke and Ernzerhof (PBE) potentials.<sup>27</sup> The electron-ion interaction is described by the projector-augmented wave (PAW) scheme,<sup>28,29</sup> and the electronic wave functions are expanded by plane waves up to a kinetic energy of 500 eV. The Brillouin zones are sampled using a  $2 \times 2 \times 2$  Monkhorst-Pack mesh for the crystal case<sup>30</sup> and Gamma point for the isolated and dimer cases, since in this case there is no interaction between neighbor cells. The convergence of the calculated properties with respect to the number of k points and supercell size is ascertained. The many body dispersion method of Tkatchenko et al.<sup>31</sup> is used to account for van der Waals interactions. The spin-orbit coupling (SOC) was used within the noncollinear approach as implemented in VASP (see Ref. <sup>32</sup>).

The calculations have been carried out with and without taking the van der Waals interactions, spin polarization, and SOC interactions into account. Consequently, the relative weight of each interaction and its compounding effect in the overall behavior has been established. The experimental XRD data is only available for Br6A crystal.<sup>1</sup> However, for the other halogenated versions of this molecule (aka F6A, Cl6A and I6A), no experimental data is available. The electronic configurations of the halogens are similar; only their size and electronegativity are different. They do not create any additional dangling bonds nor missing bonds when substituted. Therefore, it is to be expected that with only one atom exchanged, the halogen, F6A, Cl6A, and I6A have unit cell structures similar to that of Br6A, and that the most significant changes are manifest in the lattice constants. Hence, using the atomic positions and orientations of Br6A as the starting coordinates for the new molecules, stable crystalline structures are derived based on accurate total energy minimization. The lattice constants for each compound can be determined by varying them independently along all 3 dimensions, and identifying the combination of  $a$ ,  $b$ , and  $c$  values that result in the lowest energy. To validate this

approach, we submit a slightly perturbed Br6A configuration to the minimization procedure. The experimental and calculated lattice constants are summarized in Table 3-1. Optimized lattice parameters of Br6A are found to be 9.51 Å, 9.64 Å and 10.85 Å, while the corresponding experimental values are 9.51 Å, 9.69 Å and 10.95 Å, respectively. The lattice mismatch between the two is less than 1 percent for any lattice constant. After judiciously calculating the lattice constants for the other halogenated version of this molecule, we have analyzed the halogen bond formation of the X6A (X=F, Cl, Br, and I) molecules using the density of states (DOS), the real space charge density and the crystal orbital Hamilton population (COHP) analysis, which can provide important information about the local chemistry of the species.

The TD-DFT calculations were performed using Gaussian 16<sup>33</sup> for the molecular dimers. We used the B3LYP functional with the 6-31G(d,p) basis set, except that for Iodine atom we used the 3-21G basis set. Optimization of the ground state geometries is followed by an analysis of normal modes of atomic motion to confirm the stability of the optimized structures. The TD-DFT calculations are then carried out to study the nature of the low-lying excited states. Furthermore, the natural bond orbital (NBO) analysis is performed on molecular dimers in order to calculate the second-order E(2) interaction energies.

### 3.3 Results and Discussion

Single-crystal X-ray diffraction (XRD) data for Br6A molecules indicates close proximity between the carbonyl oxygen and the bromine of the neighboring molecule. The measured value of 2.86 Å for the bromine–oxygen halogen bond length is among the shortest halogen bonds reported<sup>34</sup> and suggests definite electronic interaction between the two atoms. Moreover, phosphorescence from Br6A crystals is strong, but cannot be detected when Br6A is in solution. These experimental findings strongly suggest that halogen bonding is the prevalent

reason for the remarkably efficient phosphorescence of Br6A. A halogen bond occurs when there is a net attractive interaction between an electrophilic region associated with a halogen atom in a molecular entity and a nucleophilic region in another, or the same molecular entity.<sup>35</sup> To investigate the existence of halogen bonding, DFT calculations are performed for Br6A dimers in which the spacing between the Br atom of one of the molecules and the aldehyde group of the other, i.e., the two moieties expected to form the halogen bond, is systematically varied. When simulations are carried out without accounting for van der Waals interactions, the minimum energy of the system occurs at a halogen bond length of 3.025 Å. By contrast, when including van der Waals interactions the molecules of the dimer approach closer to each other and the equilibrium halogen bond length drops to 2.976 Å. Since our system is not spin polarized, taking spin polarization into account has no effect on the halogen bond length. However, accounting for SOC interactions shortens to the halogen bond length to 2.936 Å. This trend highlights the interaction between the carbonyl oxygen and the bromine of the neighboring molecule. Moreover, performing the same calculations for a chain of Br6A molecules shows the same decreasing trend and clearly reveals the energy-lowering electronic interaction between the two atoms (Figure 3-1).

The unit cell structure of the Br6A crystal, as derived from experimental XRD data,<sup>1</sup> is shown in Figure 3-1. The structures of the other derivatives of this molecule, F6A, Cl6A and I6A, obtained using the approach described above, are geometrically similar, except for the differences in the unit cell parameters, which are reported in Table 3-1.

Table 3-1. Calculated and experimental lattice constants for F6A, Cl6A, Br6A, and I6A

Lattice Constants	F6A <sup>1</sup>	Cl6A <sup>1</sup>	Br6A <sup>1</sup>	Br6A <sup>2</sup> (error)	I6A <sup>1</sup>
a	9.51 Å	9.51 Å	9.51 Å	9.51 Å (0%)	9.51 Å
b	9.49 Å	9.59 Å	9.69 Å	9.64 Å (0.52%)	9.79 Å
c	10.95 Å	10.95 Å	10.95 Å	10.85 Å (0.91%)	11.05 Å

<sup>1</sup> Calculated lattice constants<sup>2</sup> Experimental lattice constants

All four halogen species are capable of acting as halogen bond donors and follow a general trend in terms of bond strength: F < Cl < Br < I, with iodine normally forming the strongest interactions.<sup>36</sup> When the halogen is bonded to an electron-withdrawing moiety, like phenyl, it is more likely to form stronger halogen bonds.<sup>37</sup> According to our calculations, the halogen bond distance in X6A molecules is 3.15 Å, 2.86 Å, 2.81 Å and 2.77 Å for X=F, Cl, Br and I, respectively, which follows the same trend as in the literature, and indicates that iodine forms the strongest and fluorine the weakest interaction. We have also calculated the formation energy of the halogen bonds. The formation energy is the amount of energy released upon the formation of a bond. Therefore, bond formation is always an exothermic process. As it can be seen from table 3-2, the bond formation energy for Cl, Br, and I are exothermic, which suggests formation of a strong halogen bond. In these molecules halogen and oxygen are located in close proximity, closer than the sum of the van der Waals radii (Table 3-2). These anomalously short intermolecular distances are among the strongest halogen bonds ever reported.

Table 3-2. Calculated properties of halogen bond interaction for F6A, Cl6A, Br6A, and I6A

Crystal	F6A	Cl6A	Br6A	I6A
Halogen Bond Length (Å)	3.15	2.86	2.81	2.77
Sum of the van der Waals radius of oxygen and halogen (Å)	2.75	3.20	3.35	3.55
NBO charge on halogen	-0.339	+0.049	+0.103	+0.202
Formation energy of the halogen bond (eV)	+0.0225	-0.0612	-0.1097	-0.1773
Second-order E(2) interaction energy (kcal/mol)	0.06	2.13	4.39	10.12

The standard procedure of handling halogen interactions is using sigma-hole and lone-pair to sigma\* interactions.<sup>38</sup> Therefore, We have carried out a natural bond order B3LYP analysis of the molecular dimers. As can be seen in table 3-2 (NBO charge on halogen), our results show the presence of a positive electrostatic region on the outermost portion of the halogen's surface known as a  $\sigma$ -hole<sup>38</sup> for the Cl, Br and I derivatives. However, fluorine has a negative electronic charge on the outermost portion of its surface, which substantiates the positive value of the halogen bond formation energy. These findings indicate that the interaction between F and the neighboring oxygen is repulsive.

The second-order E(2) interaction energies we calculated are reported in Table 3-2. This analysis is carried out by examining all possible interactions between filled Lewis-type NBOs and empty non-Lewis NBOs, estimating their energetic importance via 2<sup>nd</sup>-order perturbation theory. The strongest interaction is identified for the interaction of the lone-pair orbitals of oxygen with the adjacent sigma\* C-X (X=F, Cl, Br, and I) bonds of the neighboring molecule. As expected, bromine and iodine form the strongest halogen bonds with second-order E(2) interaction energies of 4.39 and 10.12 kcal/mol, respectively.



The excited-state properties and the nature of the singlet and triplet states of X6A molecules have been examined using TD-DFT calculations. All the X6A molecules exhibit  $(n\pi^*) S_1$  and  $(\pi\pi^*) T_3$  states. After excitation to the  $(n\pi^*) S_1$  state it undergoes efficient intersystem crossing to the triplet manifold. The presence of oxygen atom in the aldehyde group generates the  $n\pi^*$  state and leads to strong SOC that facilitates intersystem crossing from  $(n\pi^*) S_1$  to  $(\pi\pi^*) T_3$  according to El-Sayed's rule,<sup>39,40</sup> followed by internal conversion to the  $(\pi\pi^*) T_1$  state.

As mentioned earlier, the relaxation of the Br6A crystal yields a lattice constant of  $b = 9.636 \text{ \AA}$ , and a halogen bond length of  $2.807 \text{ \AA}$ . The  $b$  lattice constant, as well as the halogen bond length are deliberately increased to investigate the effect of halogen bonding on the DOS and the HOMO-LUMO energy gap. As can be seen in Figure 3-2, which shows the DOS near the HOMO-LUMO gap, decreasing the halogen bond length results in a red shift of the LUMO states. We surmise that HOMO and LUMO orbitals include mostly oxygen and bromine interactions, which cause the change in the energy gap. A more precise analysis is provided below. F6A, Cl6A and I6A also exhibit the same trend as Br6A, where I6A exhibits the greatest decrease in the LUMO energies, since it has the strongest halogen bonding interaction.

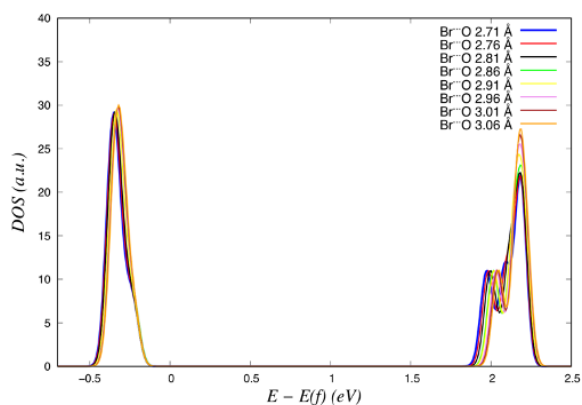


Figure 3-2. Total DOS of Br6A Crystal, with different  $b$  lattice constant. By decreasing  $b$  lattice constant, the halogen bond length decreases accordingly and there is a red shift in the LUMO states. All spectra are aligned relative to the Fermi level.

The projected DOS plot in Figure 3-3 and HOMO-LUMO orbital renders in Figure 3-4 also reveal the contribution of the Br and O in HOMO and LUMO states. It is known that aromatic aldehydes produce triplet states with high quantum yield at room temperature.<sup>41, 42</sup> It is expected that HOMO and LUMO states of Br6A molecule localize on the benzaldehyde group, but as can be seen in Figure 3-4, the bromine atom also contributes to the HOMO and LUMO states. Such a contribution may be useful. The configuration of the oxygen of the aromatic carbonyl group adjacent to a bromine exhibits some degree of spin-orbit coupling. However, because of the heavy atom effect, bromine shows stronger spin-orbit coupling interactions. In Br6A molecules, carbonyl oxygen internally, and bromine of the neighboring molecule externally promote singlet-triplet conversion and improve the phosphorescence property of these molecules.

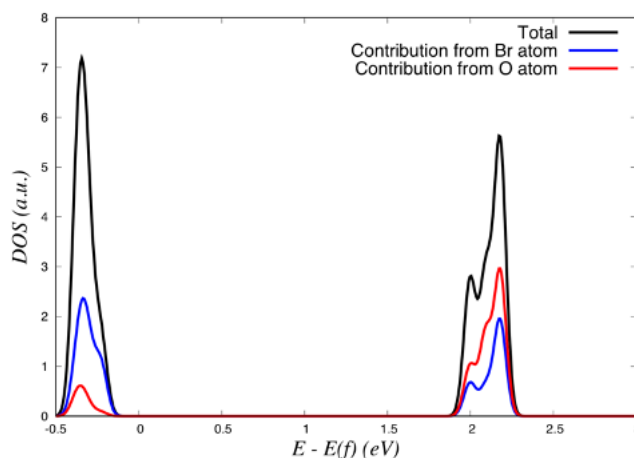


Figure 3-3. Site projected electronic density of states of Crystal Br6A. Bromine in crystal (blue trace), oxygen in crystal (red trace), total density of states of Br6A crystal (black trace). All spectra are aligned relative to the Fermi level.

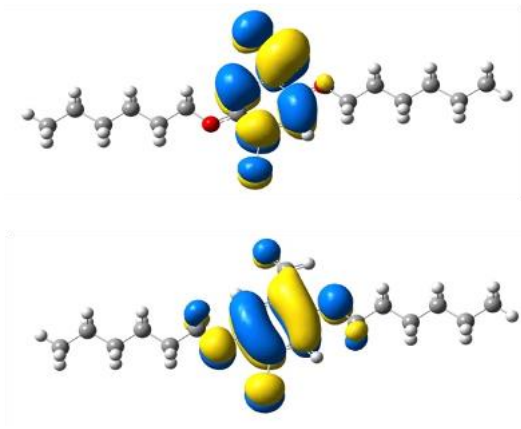


Figure 3-4. Calculated distributions of HOMO (bottom) and LUMO (top) orbitals of the Br6A molecule using B3LYP/6-31g(d,p) level in vacuum

Among the interesting advantages of the triplet-producing aromatic aldehydes is the possibility of generating triplet states from other molecules by direct transfer of energy from carbonyl triplets to a neighboring molecule.<sup>41, 43</sup> As mentioned earlier, the quantum yield of Br6A is enhanced by diluting Br6A into the crystals of Br6. We hypothesize that triplet states produced by Br6A molecules transfer to Br6 molecules and the presence of two bromines in the Br6 molecule increases the spin-orbit coupling interactions, which, in turn, promotes the phosphorescence emission.

To illustrate the detailed nature of the X-O (X=F, Cl, Br, and I) halogen bonding, we illustrate the charge redistribution by means of the electron density difference. The electron density difference,  $\Delta\rho$ , directly reveals where and how much the electron gain and loss take place, and is defined as

$$\Delta\rho = \rho_{dimer} - (\rho_{X6A_1} + \rho_{X6A_2})$$

where  $\rho_{dimer}$  is the electron density of the combined two molecules of X6A (dimer), while  $\rho_{X6A_1}$  and  $\rho_{X6A_2}$  are the electron densities of the isolated individual molecules, which are calculated by freezing the atomic positions of the respective dimer system. It should be noted that  $\Delta\rho$  is a function of the x-, y-, and z-coordinates, and therefore, it is impossible to give a

quantitative three-dimensional representation of it in a single figure. Instead, Figure 3-5 shows the charge density difference plots of X6A with the isosurface level of  $0.0006 \text{ e}\text{\AA}^{-3}$ , where the density differences can be qualitatively assessed. Blue and red regions denote loss (depletion) and gain (accumulation) of charges, respectively.

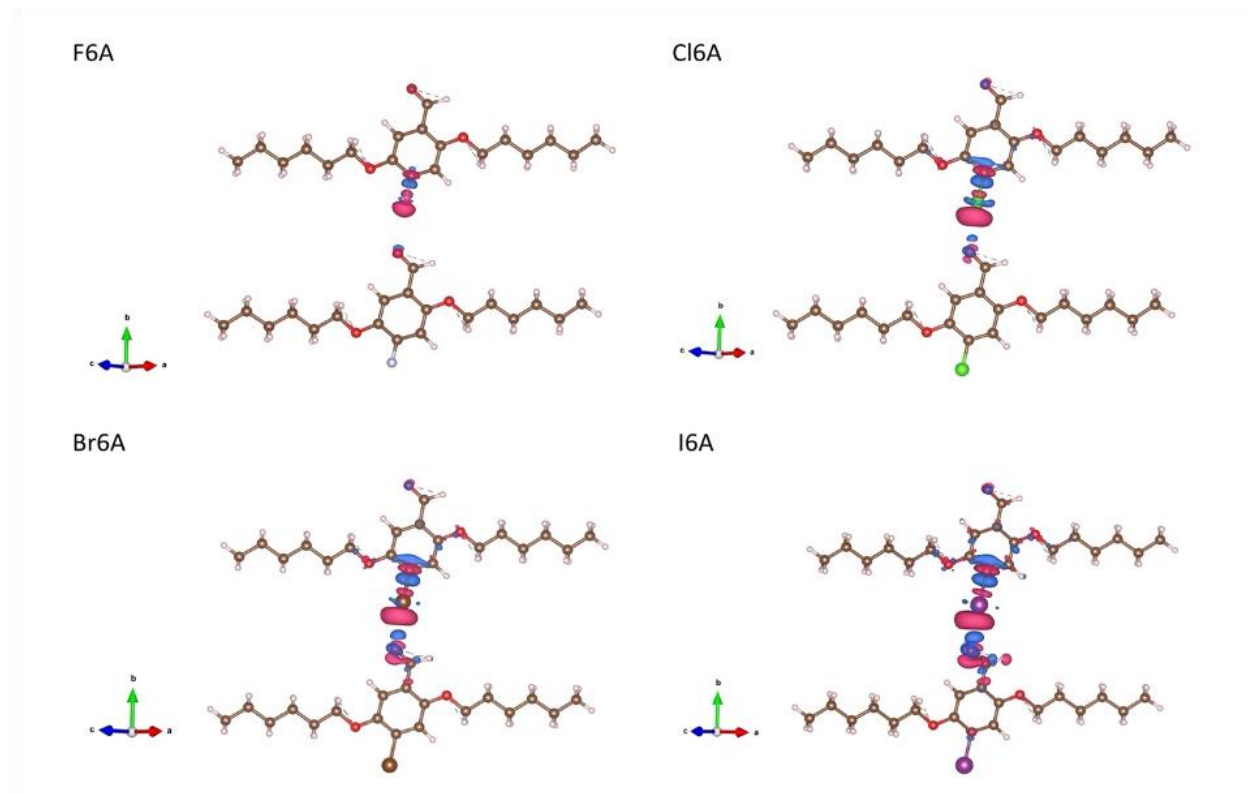


Figure 3-5. Charge density difference plots of X6A with the isosurface level of  $0.0006 \text{ e}\text{\AA}^{-3}$ . Blue and red regions denote loss (depletion) and gain (accumulation) of charges, respectively. a lattice constant is along x axis, b lattice constant is along y axis, and c lattice constant is along z axis.

As in many other works,<sup>44-46</sup> we chose to calculate the plane-averaged electron density difference (PAEDD) along the direction of the halogen bonding, which allows for a quantitative evaluation of electron redistribution upon formation of the halogen bonds. PAEDD is the average of electron density difference ( $\Delta\rho$ ) on a certain plane, which in this work is defined as

$$\sigma(y) = \frac{1}{A} \iint_A \Delta\rho(r) dx dz,$$

where  $\Delta\rho(r)$  is the electron density difference at point  $r$  and  $A$  is the area of  $x$ - $z$ -plane, perpendicular to the hydrogen bonding direction ( $y$ -direction).

Figure 3-6 shows the plane-averaged electron density difference (PAEDD) along the direction of the halogen bonding, which allows for a quantitative evaluation of electron redistribution upon formation of these halogen bonds. This figure reveals the nature of halogen bonding between the halogen  $X$  ( $X$ =F, Cl, Br, and I) and the oxygen of the nearest molecule. Solid lines represent a charge accumulation region and dotted lines represent charge depletion regions. Accumulation of more charge along the  $X$ -O ( $X$ =F, Cl, Br, and I) signifies an enhancement of halogen bonding. Evaluation of the integrals of  $\Delta\sigma$  suggested that the charge accumulation for the X6As are as follows: F 0.0653 e, Cl 0.103 e, Br 0.139 e, I 0.195 e. As expected, I6A exhibits the most accumulation of charge, which is consistent with it forming the strongest halogen bond, while F6A incurs the least accumulation of charge.

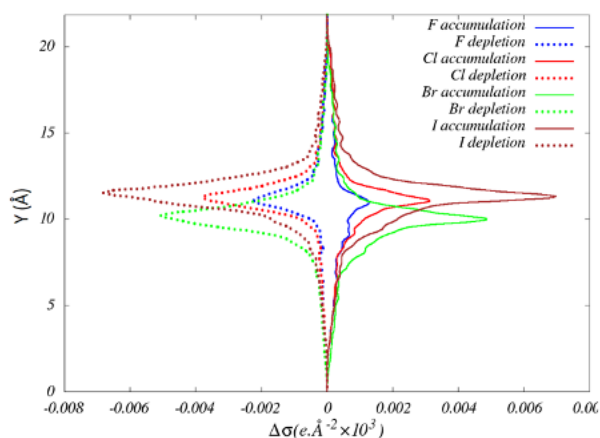


Figure 3-6. Plot of the plane-averaged electron density difference along the direction of the halogen bonding. The solid and dotted line represent charge accumulation and depletion, respectively.

The above discussion of charge redistribution into hybrid states is a global view of overall orbital types and energies. The nature of the halogen bonds can be understood by considering the crystal orbital Hamilton populations (COHP) analysis.<sup>47, 48</sup> The DOS analysis

shows where the electrons are, but nothing about their bonding character. However, a COHP diagram shows the bonding (positive values) and antibonding (negative values) contributions to the band-structure energy. It divides the band-structure energy into orbital-pair interactions; in other words, it is a bond-weighted DOS between a pair of adjacent atoms. Figure 3-7 shows the COHP analyses, obtained with the LOBSTER (Local Orbital Basis Suite Towards Electronic-Structure Reconstruction) code.<sup>49</sup> These are normalized by the number of bonds and are represented with reversed sign, so that positive values of the COHP represent bonding, and negative values antibonding contributions.

We carried out COHP analyses for different combinations of  $s$ ,  $p_x$ ,  $p_y$ , and  $p_z$  orbitals between halogen and the oxygen of the neighboring molecule for X6A (X=F, Cl, Br, I). Since the halogen bonding is in  $y$ -direction, we find that only  $s$  and  $p_y$  orbitals have large COHP peaks. Therefore, here, we have only presented the COHP diagrams of the  $s$  and  $p_y$  orbitals. In Figure 3-7, for F6A, we notice strong bonding contributions from F2 $p_y$ -O2 $p_y$  in the interval from -11 eV to -7 eV, but also some antibonding contributions in the intervals from -6 eV to -4 eV and from -1 eV to 0 eV. However, COHP strength is significantly reduced compared to the other halogens, which also indicates weak halogen bonding strength in F6A case.

On the other hand, we observe substantial bonding contributions from X-O (X=Cl, Br, and I) in the interval from -9 eV to -1 eV, accompanied by smaller antibonding contributions in the interval from -5 eV to -1 eV. The larger footprint of X-O bonding contributions noticed in the COHP for I-O in comparison to X-Br(Cl), compounded with the bonding charge density of X-O bonds described earlier, suggests that the bonding contributions increase from Cl, Br, and I, respectively.

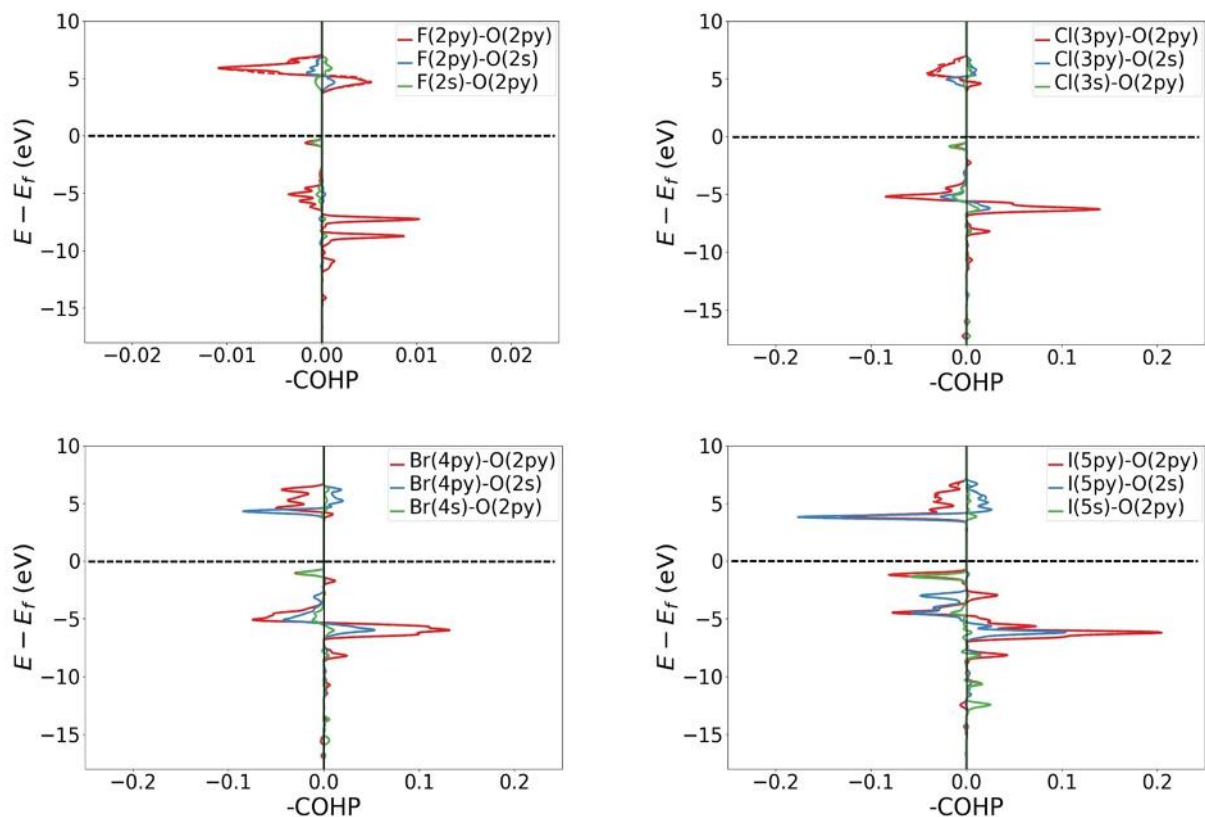


Figure 3-7. COHP analysis for halogen and Oxygen orbitals. The various components show the dominating orbital interactions in each case. Note that x axis for F is ten times smaller than others. All spectra are aligned relative to the Fermi level.

### 3.4 Conclusions

We report a first-principles quantum mechanical investigation of Br6A and its derivatives based on DFT and TD-DFT methods, in order to explain experimentally observed properties and to provide guidance for the design of purely organic phosphorescence compounds. The presence of halogen bonding in Br6A and other derivatives of this molecule are demonstrated. It is revealed that iodine forms the strongest halogen bonding interaction and fluorine forms the weakest interaction. The strong halogen bonding present in crystals of Br6A and I6A more effectively suppress vibrations and prevent non-radiative decays compared to F and Cl derivatives. Along with suppression of vibration-induced losses, for heavy atoms, spin-orbit

coupling is large and a change in spin is thus more favorable. Consequently, triplet to singlet transitions are most common in molecules containing iodine and bromine. This work also highlights that there is a decrease in electrical energy band gap as larger halogens are involved. The dependence of energy band gap on the halogen species is important in the context of tuning molecules for their emission colors. For device fabrication, film forming materials, like polymers and amorphous solids are preferred. Although these molecules are very promising for developing purely organic phosphors, they still cannot be used for practical applications because they require crystalline materials. However, the insights gained from computational analyses can serve to develop materials design strategies for suppressing vibrational losses in polymers and amorphous solids.

### 3.5 References

- (1) O. Bolton, K. Lee, H.-J. Kim, K. Y. Lin and J. Kim, Activating efficient phosphorescence from purely organic materials by crystal design, *Nature chemistry*, 2011, 3, 205-210.
- (2) C. W. Tang and S. A. VanSlyke, Organic electroluminescent diodes, *Applied physics letters*, 1987, 51, 913-915.
- (3) C. Adachi, M. A. Baldo, M. E. Thompson and S. R. Forrest, Nearly 100% internal phosphorescence efficiency in an organic light-emitting device, *Journal of Applied Physics*, 2001, 90, 5048-5051.
- (4) R. Ansari, W. Shao, S.-J. Yoon, J. Kim and J. Kieffer, Charge Transfer as the Key Parameter Affecting the Color Purity of Thermally Activated Delayed Fluorescence Emitters, *ACS Applied Materials & Interfaces*, 2021, 13, 28529-28537.
- (5) S. Kappaun, C. Slugovc and E. J. List, Phosphorescent organic light-emitting devices: working principle and iridium based emitter materials., *Int J Mol Sci*, 2008, 9, 1527-1547.
- (6) M. Kim, S. Yoon, S. H. Han, R. Ansari, J. Kieffer, J. Y. Lee and J. Kim, Molecular Design Approach Managing Molecular Orbital Superposition for High Efficiency without Color Shift in Thermally Activated Delayed Fluorescent Organic Light-Emitting Diodes, *Chemistry–A European Journal*, 2019, 25, 1829-1834.
- (7) G. Zhou, W. Wong and X. Yang, New Design Tactics in OLEDs Using Functionalized 2-Phenylpyridine-Type Cyclometalates of Iridium (III) and Platinum (II), *Chemistry–An Asian Journal*, 2011, 6, 1706-1727.



- (8) M. A. Baldo, S. Lamansky, P. E. Burrows, M. E. Thompson and S. R. Forrest, Very high-efficiency green organic light-emitting devices based on electrophosphorescence, *Applied Physics Letters*, 1999, 75, 4-6.
- (9) M. A. Baldo, D. F. O'Brien, Y. You, A. Shoustikov, S. Sibley, M. E. Thompson and S. R. Forrest, Highly efficient phosphorescent emission from organic electroluminescent devices, *Nature*, 1998, 395, 151-154.
- (10) P. E. M. Siegbahn, Trends of metal-carbon bond strengths in transition metal complexes, *The Journal of Physical Chemistry*, 1995, 99, 12723-12729.
- (11) Wang, S., Yuan, W. Z. and Zhang, Y. (2016) in *Aggregation-Induced Emission: Materials and Applications Volume 2* Eds.), pp. 1-26, ACS Publications,
- (12) D. Lee, O. Bolton, B. C. Kim, J. H. Youk, S. Takayama and J. Kim, Room temperature phosphorescence of metal-free organic materials in amorphous polymer matrices, *Journal of the American Chemical Society*, 2013, 135, 6325-6329.
- (13) M. S. Kwon, D. Lee, S. Seo, J. Jung and J. Kim, Tailoring intermolecular interactions for efficient room-temperature phosphorescence from purely organic materials in amorphous polymer matrices, *Angewandte Chemie*, 2014, 126, 11359-11363.
- (14) G. Bergamini, A. Fermi, C. Botta, U. Giovanella, S. Di Motta, F. Negri, R. Peresutti, M. Gingras and P. Ceroni, A persulfurated benzene molecule exhibits outstanding phosphorescence in rigid environments: from computational study to organic nanocrystals and OLED applications, *Journal of Materials Chemistry C*, 2013, 1, 2717-2724.
- (15) H. Y. Gao, Q. J. Shen, X. R. Zhao, X. Q. Yan, X. Pang and W. J. Jin, Phosphorescent cocrystal assembled by 1, 4-diiodotetrafluorobenzene with carbazole based on C-I...  $\pi$  halogen bonding, *Journal of Materials Chemistry*, 2012, 22, 5336-5343.
- (16) H. Y. Gao, X. R. Zhao, H. Wang, X. Pang and W. J. Jin, Phosphorescent cocrystals assembled by 1, 4-diiodotetrafluorobenzene and fluorene and its heterocyclic analogues based on C-I...  $\pi$  halogen bonding, *Crystal growth & design*, 2012, 12, 4377-4387.
- (17) Y. J. Gao, C. Li, R. Liu and W. J. Jin, Phosphorescence of several cocrystals assembled by diiodotetrafluorobenzene and three ring angular diazaphenanthrenes via Cl... N halogen bond, *Spectrochimica Acta Part A: Molecular and Biomolecular Spectroscopy*, 2017, 173, 792-799.
- (18) S. Sarkar, H. P. Hendrickson, D. Lee, F. DeVine, J. Jung, E. Geva, J. Kim and B. D. Dunietz, Phosphorescence in bromobenzaldehyde can be enhanced through intramolecular heavy atom effect, *The Journal of Physical Chemistry C*, 2017, 121, 3771-3777.
- (19) H. Saigusa and T. Azumi, Internal heavy atom effect on the triplet spin sublevels of the lowest triplet state of naphthalene. I. Radiative and nonradiative decays of the spin sublevels of 1-halonaphthalenes, *The Journal of Chemical Physics*, 1979, 71, 1408-1413.
- (20) G. G. Giachino and D. R. Kearns, Nature of the external heavy-atom effect on radiative and nonradiative singlet-triplet transitions, *The Journal of Chemical Physics*, 1970, 52, 2964-2974.

- (21) S. P. McGlynn, R. Sunseri and N. Christodouleas, External Heavy-Atom Spin-Orbital Coupling Effect. I. The Nature of the Interaction, *The Journal of Chemical Physics*, 1962, 37, 1818-1824.
- (22) P. G. Seybold and W. White, Room temperature phosphorescence analysis. Use of the external heavy-atom effect, *Analytical Chemistry*, 1975, 47, 1199-1200.
- (23) Glossary of Terms Used in Photochemistry, 3rd Edition (IUPAC Recommendations 2006), 2007, 331.
- (24) D. W. Oxtoby, H. P. Gillis and N. H. Nachtrieb, *Principles of Modern Chemistry*, 1999,
- (25) G. Kresse and J. Hafner, Ab initio molecular-dynamics simulation of the liquid-metal–amorphous-semiconductor transition in germanium, *Physical Review B*, 1994, 49, 14251.
- (26) G. Kresse and J. Furthmüller, Efficiency of ab-initio total energy calculations for metals and semiconductors using a plane-wave basis set, *Computational materials science*, 1996, 6, 15-50.
- (27) J. P. Perdew, K. Burke and M. Ernzerhof, Generalized gradient approximation made simple, *Physical review letters*, 1996, 77, 3865.
- (28) P. E. Blöchl, Projector augmented-wave method, *Physical review B*, 1994, 50, 17953.
- (29) G. Kresse and D. Joubert, From ultrasoft pseudopotentials to the projector augmented-wave method, *Physical review b*, 1999, 59, 1758.
- (30) H. J. Monkhorst and J. D. Pack, Special points for Brillouin-zone integrations, *Physical review B*, 1976, 13, 5188.
- (31) A. Tkatchenko, R. A. DiStasio Jr, R. Car and M. Scheffler, Accurate and efficient method for many-body van der Waals interactions, *Physical review letters*, 2012, 108, 236402.
- (32) S. Steiner, S. Khmelevskiy, M. Marsmann and G. Kresse, Calculation of the magnetic anisotropy with projected-augmented-wave methodology and the case study of disordered Fe<sub>1-x</sub>Co<sub>x</sub> alloys, *Physical Review B*, 2016, 93, 224425.
- (33) M. J. Frisch, G. W. Trucks, H. B. Schlegel, G. E. Scuseria, M. A. Robb, J. R. Cheeseman, G. Scalmani, V. Barone, G. A. Petersson, H. Nakatsuji, X. Li, M. Caricato, A. V. Marenich, J. Bloino, B. G. Janesko, R. Gomperts, B. Mennucci, H. P. Hratchian, J. V. Ortiz, A. F. Izmaylov, J. L. Sonnenberg, Williams, F. Ding, F. Lipparini, F. Egidi, J. Goings, B. Peng, A. Petrone, T. Henderson, D. Ranasinghe, V. G. Zakrzewski, J. Gao, N. Rega, G. Zheng, W. Liang, M. Hada, M. Ehara, K. Toyota, R. Fukuda, J. Hasegawa, M. Ishida, T. Nakajima, Y. Honda, O. Kitao, H. Nakai, T. Vreven, K. Throssell, J. A. Montgomery Jr., J. E. Peralta, F. Ogliaro, M. J. Bearpark, J. J. Heyd, E. N. Brothers, K. N. Kudin, V. N. Staroverov, T. A. Keith, R. Kobayashi, J. Normand, K. Raghavachari, A. P. Rendell, J. C. Burant, S. S. Iyengar, J. Tomasi, M. Cossi, J. M. Millam, M. Klene, C. Adamo, R. Cammi, J. W. Ochterski, R. L. Martin, K. Morokuma, O. Farkas, J. B. Foresman and D. J. Fox, *Gaussian 16 Rev. C.01*, 2016,
- (34) P. Metrangolo and G. Resnati, Halogen Bonding: A Paradigm in Supramolecular Chemistry, *Chem. Eur. J.*, 2001, 7, 2511-2519.

- (35) G. R. Desiraju, P. S. Ho, L. Kloo, A. C. Legon, R. Marquardt, P. Metrangolo, P. Politzer, G. Resnati and K. Rissanen, Definition of the halogen bond (IUPAC Recommendations 2013), *Pure Appl. Chem*, 2013, 85, 1711-1713.
- (36) P. Politzer, P. Lane, M. C. Concha, Y. Ma and J. S. Murray, An overview of halogen bonding, *Journal of molecular modeling*, 2007, 13, 305-311.
- (37) P. Metrangolo, H. Neukirch, T. Pilati and G. Resnati, Halogen bonding based recognition processes: a world parallel to hydrogen bonding, *Accounts of chemical research*, 2005, 38, 386-395.
- (38) T. Clark, M. Hennemann, J. S. Murray and P. Politzer, Halogen bonding: the  $\sigma$ -hole, *Journal of molecular modeling*, 2007, 13, 291-296.
- (39) M. Baba, Intersystem Crossing in the  $1n\pi^*$  and  $1\pi\pi^*$  States, *The Journal of Physical Chemistry A*, 2011, 115, 9514-9519.
- (40) K. Bhattacharyya and A. Datta, Visible-Light-Mediated Excited State Relaxation in Semi-Synthetic Genetic Alphabet: d5SICS and dNaM, *Chemistry—A European Journal*, 2017, 23, 11494-11498.
- (41) H. L. J. Bäckström and K. Sandros, Transfer of Triplet State Energy in Fluid Solutions, *Acta Chemica Scandinavica*, 1960, 14, 48-62.
- (42) G. S. Hammond and W. M. Moore, The role of a triplet state in the photoreduction of benzophenone, *Journal of the American Chemical Society*, 1959, 81, 6334-6334.
- (43) G. O. Schenck and R. Steinmetz, Neuartige durch Benzophenon photosensibilisierte Additionen von Maleinsäureanhydrid an Benzol und andere Aromaten, *Tetrahedron Letters*, 1960, 1, 1-8.
- (44) B. Meyer and D. Vanderbilt, Ab initio study of BaTiO<sub>3</sub> and PbTiO<sub>3</sub> surfaces in external electric fields, *Physical Review B*, 2001, 63, 205426.
- (45) Y. B. Xue, Y. Y. Shan and H. Xu, The role of boundary conditions in tuning the electronic properties of the (0 0 1) LaAlO<sub>3</sub>/SrTiO<sub>3</sub> interface, *Computational Materials Science*, 2018, 149, 354-359.
- (46) Y. Xue, C. Geng and Y. Guo, Two-Dimensional (001) LaAlO<sub>3</sub>/SrTiO<sub>3</sub> Heterostructures with Adjustable Band Gap and Magnetic Properties, *ACS Applied Materials & Interfaces*, 2019, 12, 3134-3139.
- (47) V. L. Deringer, A. L. Tchougréeff and R. Dronskowski, Crystal orbital Hamilton population (COHP) analysis as projected from plane-wave basis sets, *The journal of physical chemistry A*, 2011, 115, 5461-5466.
- (48) R. Dronskowski and P. E. Blöchl, Crystal orbital Hamilton populations (COHP): energy-resolved visualization of chemical bonding in solids based on density-functional calculations, *The Journal of Physical Chemistry*, 1993, 97, 8617-8624.
- (49) S. Maintz, V. L. Deringer, A. L. Tchougréeff and R. Dronskowski, LOBSTER: A tool to extract chemical bonding from plane-wave based DFT, *Journal of computational chemistry*, 2016, 37, 1030-1035.

## Chapter 4 Molecular Design for Fluorene Based Metal Free White Light Emitters

### 4.1 Introduction

White purely organic light-emitting materials have attracted attention for their practicality with regard to device implementation.<sup>1-6</sup> Most designs reported so far combine multiple emissive layers where two or more emissive materials simultaneously emit electromagnetic radiation that together is perceived as white.<sup>4,7,8</sup> In addition to the emissive layers, this approach requires charge transport layers to minimize the barriers for charge carriers. For example, Wu et al.<sup>9</sup> fabricated an eight-layer white organic light emitting device containing a yellow emissive layer, two blue emissive layers, and multiple charge transport layers with only 3.9% EQE. In contrast, single molecule white light emitters (SMWLEs) exhibit several advantages such as simple device fabrication, higher quantum yield, improved stability, good reproducibility, no color aging, and no phase aggregation.<sup>10</sup> There are three different types of SMWLE devices; (1) pure fluorescent,<sup>11-17</sup> (2) hybrid fluorescent/phosphorescent,<sup>18,19</sup> and (3) purely phosphorescent.<sup>6,20,21</sup> The exploration of hybrid fluorescent/phosphorescent SMWLEs is of great importance and attractive since they are promising energy-efficient choices. However, to date there are a few examples of metal-free hybrid SMWLEs, and they only work under limiting conditions such as being dissolved in a particular solution<sup>19</sup> or subject to mechanical stimuli.<sup>18</sup>

As mentioned earlier, to achieve bright room temperature phosphorescence, collision-based vibrational quenching should be suppressed and singlet to triplet ISC and radiative decay from the triplet to the singlet ground state should be enhanced. The general approach to enhance singlet to triplet ISC is to use heavy halogens (bromine and iodine) attached to the aromatic unit.

The heavy atom effect of the bromine or iodine enhances the SOC interactions and promotes spin-forbidden processes. However, this strategy may not work; for instance, diiodo-boron-dipyrrromethene (diiodo-BODIPY) does not show efficient phosphorescence, even at 77 K, although it has two heavy iodine atoms.<sup>22,23</sup> Moreover, Zhang et. al.<sup>24</sup> studied multiple halide substitution on BODIPY. Phosphorescence occurs when Br substituents are present in BODIPY, but the increase in the number of Br atoms in the BODIPY core does not change the quantum yield very significantly. Studies of naphthalene, phenanthrene, and fluorene show the same results.<sup>25,26</sup> Apparently, enhancing the heavy atom effect in organic molecules is not the only requisite for developing RTP materials.

Thus, controlling the non-radiative deactivation plays a pivotal role in RTP of metal-free phosphors. The main non-radiative deactivation process is the thermal motion and vibrations of the phosphors. Therefore, rigid conditions such as doped-crystal,<sup>27</sup> or embedding phosphors in amorphous matrices such as poly(methyl methacrylate) (PMMA)<sup>28,29</sup> are commonly pursued methods to suppress non-radiative decay.

Based on a rational design concept encompassing heavy atom effect and rigid molecular structure, J. Jung<sup>30</sup> designed a series of metal-free organic phosphors in an amorphous polymer matrix (Figure 4-1). These molecules (Br-FL series) were embedded into atactic poly(methyl methacrylate) (aPMMA) and the phosphorescence and fluorescence properties were calculated. Remarkably, Br-FL3 and Br-FL4 show over 20% fluorescent quantum yield, which is much higher than the rest of the molecules.

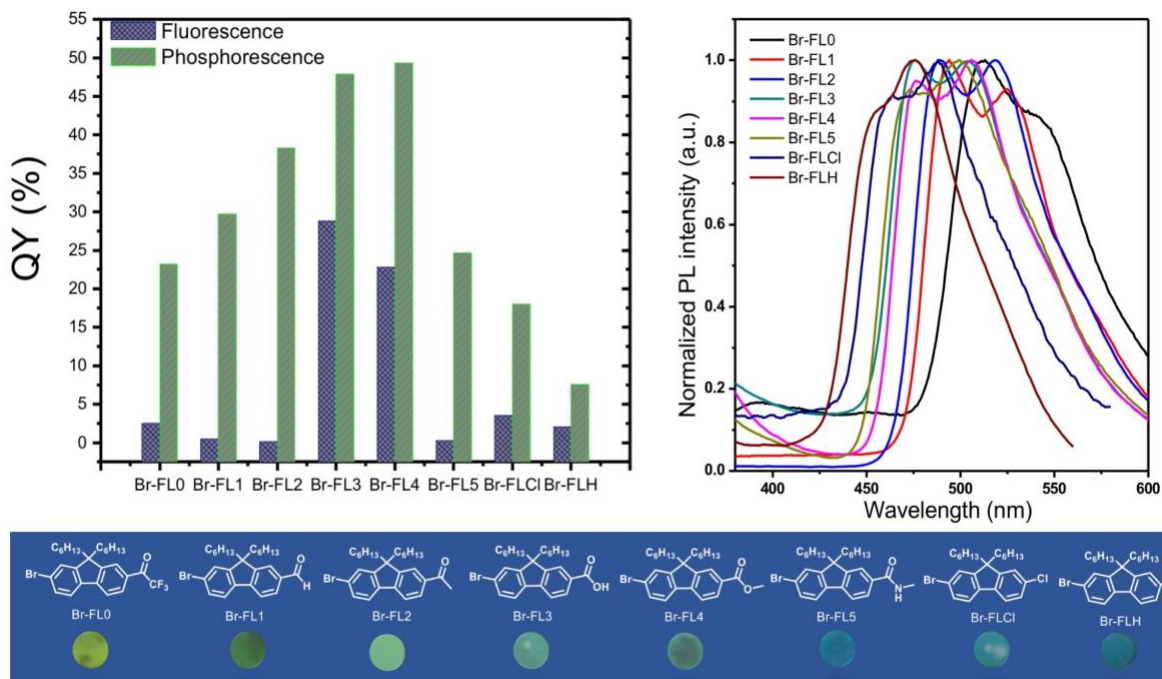


Figure 4-1. Chemical structures of designed phosphors and their phosphorescent color image upon UV irradiation (365nm) under N<sub>2</sub>. Fluorescence and phosphorescence quantum yields of Br-FL compounds (left). Steady state emission spectra of Br-FL compounds in aPMMA films (right). Figure adopted from Jaehun Jung's thesis.<sup>30</sup>

While Br-FL3 and Br-FL4 seem to be good candidates for hybrid SMWLEs because they both exhibit ~25% fluorescent and ~50% phosphorescent (Figure 4-1), the combination of fluorescent and phosphorescent emissions of these molecules is not perceived as white, but more in the blue region. Therefore, a modification of these molecules is indicated that red shifts both fluorescent and phosphorescent emissions without decreasing the quantum yields.

To identify the necessary molecular design changes of SMWLEs, we studied the Br-FL series using first principles calculations, and we were able to gain a quantitative understanding of their structure-property relationships. Our computational analysis shows why BrFL3 and BrFL4 have both high quantum yield Fluorescence and Phosphorescence, but other molecules only have fluorescence emission. Then, we designed new molecules and we were able to shift the fluorescence and phosphorescence peaks so that the combination of both generates white light.

## 4.2 Methodologies

We explored the nature of the frontier orbitals by performing quantum mechanical calculations using Gaussian 16 program. The optimized ground state geometries (S0) are obtained at the B3LYP/6-311+G(d,p) level, followed by an analysis of the atomic vibrational frequencies to confirm the stability of the optimized structures. Time-dependent density functional theory (TD-DFT) are carried out to study the excited state properties, including transition configurations, vertical excitation energies, the nature of these states, and oscillator strength. Furthermore, natural transition orbitals (NTOs) are calculated using TD-DFT to analyze the electronic configuration of the low-lying singlet and triplet states.

## 4.3 Results and Discussion

### 4.3.1 Effect of Modifying the Functional Group on the Non-bonding Electrons of Oxygen and the Fluorescence Quantum Yield

To elucidate the nature of the frontier orbitals, we plotted the HOMO-4 to LUMO orbitals (Figure 4-2). We noticed that the majority of these orbitals are the  $\pi$  and  $\pi^*$  orbitals of the benzene rings. However, one of the frontier orbitals is the non-bonding orbital of oxygen (e.g. HOMO-3 for BrFL0 and HOMO-1 for BrFL1). The inductive effect of electron-withdrawing groups such as CF<sub>3</sub>, O, and N changes the energy level of non-bonding orbital, n, of oxygen atom.

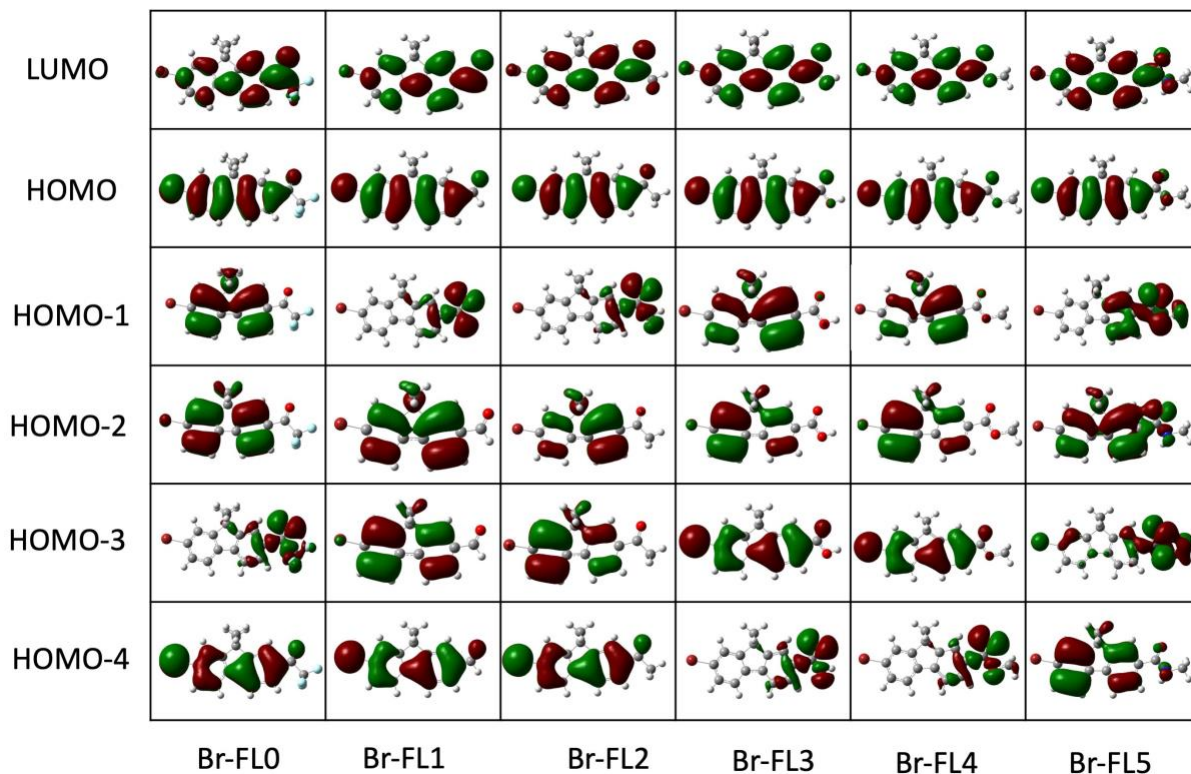


Figure 4-2. HOMO-4 to LUMO orbitals for Br-FL series.

Table 4-1 shows where the non-bonding electrons of the oxygen lie and lists the energy gaps between that orbital and the HOMO. BrFL0, BrFL1 and BrFL5 have a small energy gap between the non-bonding electrons of the oxygen and the HOMO level. However, the non-bonding electrons of oxygen lie at HOMO-4 for BrFL3 and BrFL4 and there is an energy gap of about 1.5 eV for these two molecules. As a result, it is expected that the  $n\pi^*$  transitions of carboxylic acid in BrFL3 and ester in BrFL4 occur at higher energy levels and they are not involved in fluorescence and phosphorescence emissions.



Table 4-1. where the non-bonding electrons of oxygen lie and the energy gaps between that orbital and the HOMO

	Orbital	Energy gap with HOMO level (eV)
Br-FL0	HOMO-3	0.424
Br-FL1	HOMO-1	0.778
Br-FL2	HOMO-1	0.711
Br-FL3	HOMO-4	1.561
Br-FL4	HOMO-4	1.495
Br-FL5	HOMO-1	0.775

The Energy diagram of the ground state and the excited states of these molecules were investigated by using TD-DFT calculations, as shown in Figure 4-3. As expected, the four BrFL0, BrFL1, BrFL2, and BrFL5 molecules have low-lying  $^1n\pi^*$  and  $^3n\pi^*$  states. However, the  $^1n\pi^*$  and  $^3n\pi^*$  states for BrFL3 and BrFL4 molecules lie at  $S_4$  and  $T_8$ . Although the heavy atom effect of bromine enhances the singlet-to-triplet ISC, ISC is not allowed for BrFL3 and BrFL4 according to El-Sayed's rule, which explains the remarkably high fluorescent quantum yields of BrFL3 and BrFL4. However, both the heavy atom effect and El-Sayed's rule allow  $^1\pi\pi^* \leftrightarrow ^3n\pi^*$  transitions simultaneously to be met for BrFL0, BrFL1, BrFL2, and BrFL5. Thus, singlet to triplet ISC is much more efficient, and these molecules are very weakly fluorescent.

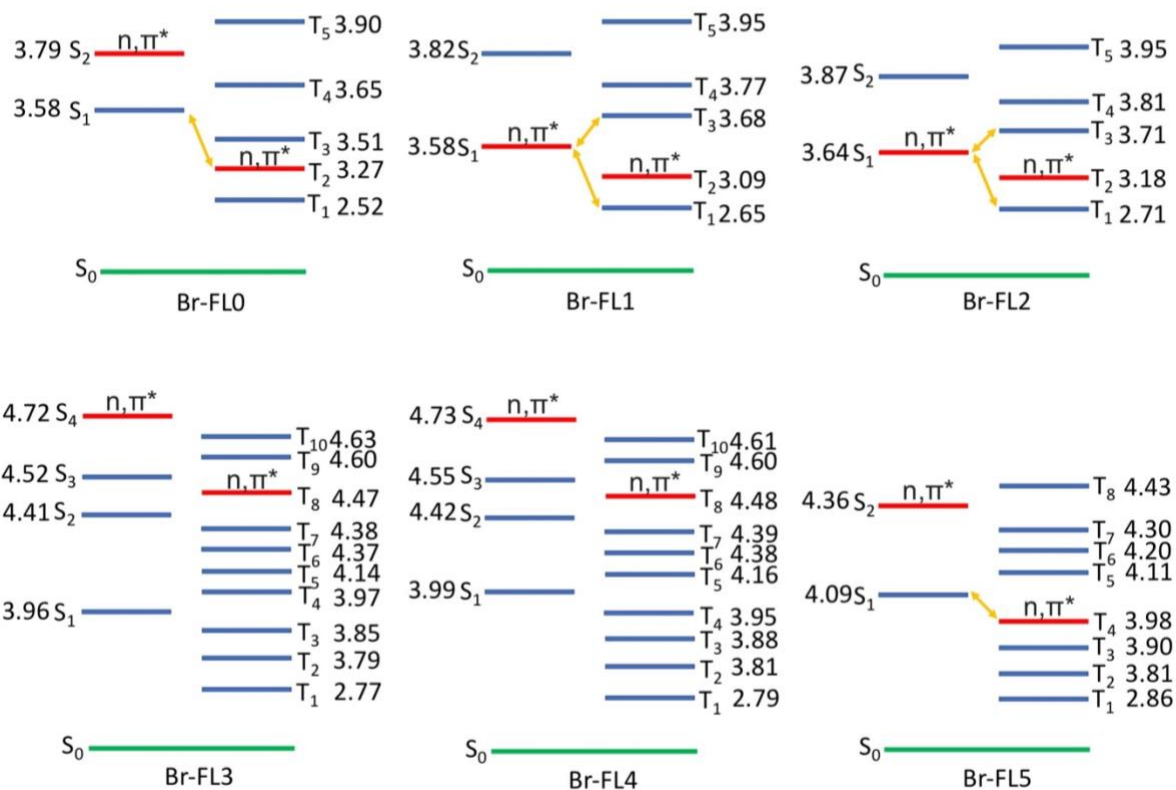


Figure 4-3. The nature of the frontier orbitals for Br-FL molecules. The blue lines show  $\pi, \pi^*$  orbitals and the red lines are  $n, \pi^*$  orbitals. Green lines indicate ground state  $S_0$ . The yellow arrows show the El-Sayed allowed intersystem crossing routes.

### 4.3.2 Effect of Extending the Conjugation on Electronic Transitions

Consider the simple case of molecular hydrogen,  $H_2$ . The molecular orbital (MO) diagram of hydrogen molecule consists of a bonding  $\sigma$  and a higher energy antibonding  $\sigma^*$  orbital (as depicted in Figure 4-4). Each hydrogen atom has one electron, therefore, the  $H_2$  molecule has two electrons. By the Aufbau principle, the two electrons are placed in the bonding  $\sigma$  orbital. If the  $H_2$  molecule was exposed to light with energy of  $\Delta E=258$  kcal/mol an electron transitions from the HOMO orbital to LUMO orbital. However, as can be seen in Figure 4-4, when a double bond molecule such as ethene is exposed to light, a  $\pi-\pi^*$  transition occurs. In this

picture, the two p atomic orbitals combine mathematically to form two  $\pi$  molecular orbitals with different energies. Of these, the bonding  $\pi$  orbital has a lower energy than the p atomic orbitals from which it is formed. Conversely, the antibonding  $\pi^*$  orbital is higher in energy. Because  $\pi$ - $\pi^*$  energy gaps are narrower than  $\sigma$ - $\sigma^*$  gaps, ethene absorbs light with energy of  $\Delta E=173$  kcal/mol.

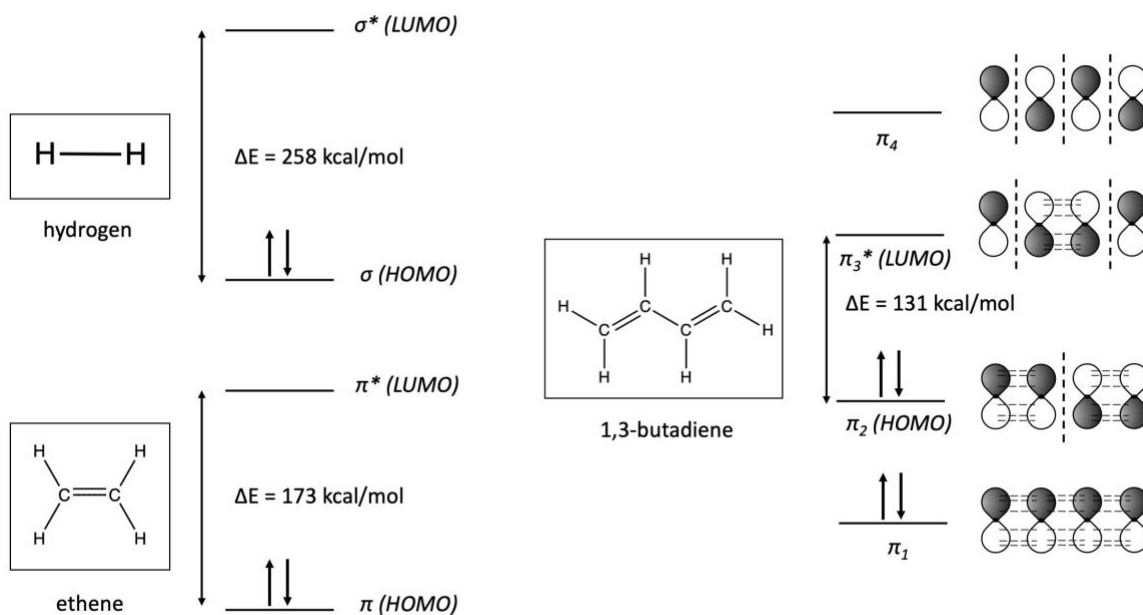


Figure 4-4. Energy diagram for the HOMO and LUMO molecular orbitals of hydrogen, ethene, and 1,3-butadiene.

Now, consider the 1,3-butadiene molecule. In this molecule, the four p atomic orbitals of carbon, designated as C1, C2, C3, and C4 from left to right, combine and form two bonding  $\pi$  and two antibonding  $\pi^*$  orbitals. As can be seen in Figure 4-4, the bonding  $\pi_1$  MO has one constructive interaction and zero nodes. The bonding  $\pi_2$  MO has one node but two constructive interactions. Therefore, it is still a bonding orbital. The antibonding  $\pi_3^*$  MO has two nodes and one constructive interaction, and the antibonding  $\pi_4^*$  MO has 3 nodes and zero constructive interaction. According to the Aufbau principle, the four electrons are placed in the bonding  $\pi_1$  and  $\pi_2$  MO's. Therefore, the  $\pi_1$  and  $\pi_2$  are the HOMO orbitals and  $\pi_3$  and  $\pi_4$  are the LUMOs.

Because  $\pi_1$  includes a constructive interaction between the C2 and C3 atoms, there is a degree of conjugation between these two carbons, which explains its shorter bond length and the barrier to rotation.

1,3-butadiene is the simplest example of a system of conjugated  $\pi$  bonds. In molecules with extended  $\pi$  conjugations, the HOMO-LUMO energy gap becomes smaller, resulting in a redshift of the emission peak. Following this principle,<sup>31,32</sup> we designed new molecules based on the Br-FL series where we extend the conjugation in BrFL3 and BrFL4 molecules.

Therefore, the newly designed molecules, Br-FL4-1 and Br-FL4-1-2, shown in Figure 4-5, might be good alternatives for hybrid fluorescent/phosphorescent white light emission. Indeed, the DFT calculations confirm that extending the conjugation shifts the emission to red. As can be seen in Figure 4-5, Br-FL4-1 and Br-FL4-2 have lower-energy  $S_1$  and  $T_1$  states. Moreover, selenium alternatives (Br-FL3-Se & Br-FL4-Se) also show extended conjugation through the non-bonding electrons of selenium, and they have lower first singlet and triplet energy levels compare to Br-FL3 and Br-FL4. However, due to the heavy atom effect of selenium, SOC interactions of Br-FL3-Se & Br-FL4-Se are about twofold stronger than that of Br-FL3 and Br-FL4 and that might increase the ISC rates, which may result in higher phosphorescence quantum yield and very low fluorescence yield.

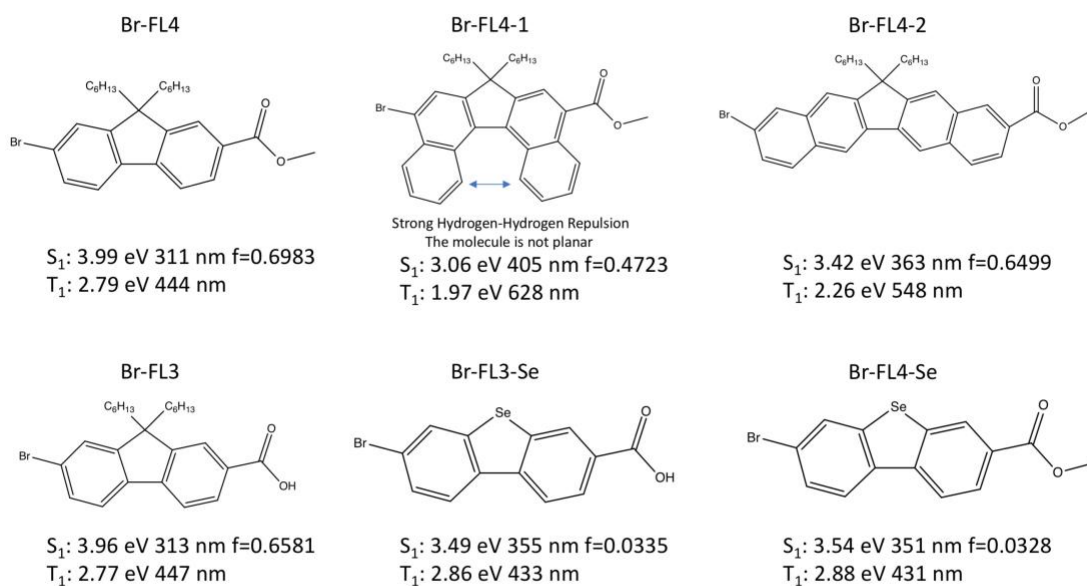


Figure 4-5. Br-FL3, Br-FL4, the newly designed compounds, and their singlet and triplet energy levels. As it can be seen, extending the conjugation redshifts the fluorescence and phosphorescence emission peaks.

We have examined the NTO orbitals of suggested molecules. Both Br-FL4-1 and Br-FL4-2 have a high energy level  $^1n\pi^*$  and  $^3n\pi^*$  states. Therefore, we expect high quantum yield fluorescence and phosphorescence emission for these molecules, similar to what we have seen for Br-FL4 itself. Therefore, we suggest these two molecules as potential candidates for SMWLEs. Further experimental synthesis and measurements are needed to verify the nature of dual fluorescence/phosphorescence emission of these molecules.

#### 4.4 Conclusions and Summary

Luminescent materials are broadly used for imaging and sensing owing to their high sensitivity, facile detection and prompt response. Practical materials for sensing and imaging must achieve intense fluorescence and oxygen sensitive phosphorescence. Therefore, hybrid fluorescent/phosphorescent SMWLEs combine all of these features in one molecular platform, which is desirable. Developing hybrid fluorescent/phosphorescent SMWLEs with high EQE

enables us to design state of the art sensing and imaging devices with one easily tunable molecular platform. Moreover, SMWLEs are useful for lighting application where only one emissive layer is used for fabricating the device saving cost on fabrication expenses. Previously in our group, Jaehun Jung<sup>30</sup> has synthesized a series of fluorene-based phosphors. Interestingly a few of these emitters show high quantum yield fluorescence making them ideal for hybrid fluorescent/phosphorescent SMWLEs. However, the combination of fluorescent and phosphorescent emission of these molecules is not perceived as white but more in the blue region. In this work, we investigated these molecules using DFT calculations and we were able to design some new molecules and shift the emission to red so that the combination of fluorescent and phosphorescent is perceived as white. Our computation-based predictive design yielded promising candidate molecules, with potential applications in sensing, imaging, and lighting.

#### 4.5 References

- (1) Du, M.; Feng, Y.; Zhu, D.; Peng, T.; Liu, Y.; Wang, Y.; Bryce, M. R. Novel Emitting System Based on a Multifunctional Bipolar Phosphor: An Effective Approach for Highly Efficient Warm-white Light-emitting Devices With High Color-rendering Index At High Luminance. *Advanced Materials* **2016**, *28*, 5963-5968.
- (2) Farinola, G. M.; Ragni, R. Electroluminescent Materials for White Organic Light Emitting Diodes. *Chemical Society Reviews* **2011**, *40*, 3467-3482.
- (3) Han, M.; Tian, Y.; Yuan, Z.; Zhu, L.; Ma, B. A Phosphorescent Molecular “Butterfly” That Undergoes a Photoinduced Structural Change Allowing Temperature Sensing and White Emission. *Angewandte Chemie International Edition* **2014**, *53*, 10908-10912.
- (4) Higuchi, T.; Nakanotani, H.; Adachi, C. High-efficiency White Organic Light-emitting Diodes Based on a Blue Thermally Activated Delayed Fluorescent Emitter Combined With Green and Red Fluorescent Emitters. *Advanced Materials* **2015**, *27*, 2019-2023.
- (5) Kamtekar, K. T.; Monkman, A. P.; Bryce, M. R. Recent Advances in White Organic Light-emitting Materials and Devices (Woleds). *Advanced Materials* **2010**, *22*, 572-582.
- (6) Ni, W.; Li, M.; Zheng, J.; Zhan, S.; Qiu, Y.; Ng, S. W.; Li, D. Approaching White-light Emission From a Phosphorescent Trinuclear Gold (I) Cluster By Modulating Its Aggregation Behavior. *Angewandte Chemie International Edition* **2013**, *52*, 13472-13476.

- (7) D'Andrade, B. W.; Forrest, S. R. White Organic Light-emitting Devices for Solid-state Lighting. *Advanced Materials* **2004**, *16*, 1585-1595.
- (8) Sun, Y.; Giebink, N. C.; Kanno, H.; Ma, B.; Thompson, M. E.; Forrest, S. R. Management of Singlet and Triplet Excitons for Efficient White Organic Light-Emitting Devices. *Nature* **2006**, *440*, 908-912.
- (9) Wu, Y. S.; Hwang, S. W.; Chen, H. H.; Lee, M. T.; Shen, W. J.; Chen, C. H. Efficient White Organic Light Emitting Devices With Dual Emitting Layers. *Thin solid films* **2005**, *488*, 265-269.
- (10) He, Z.; Zhao, W.; Lam, J. W. Y.; Peng, Q.; Ma, H.; Liang, G.; Shuai, Z.; Tang, B. Z. White Light Emission From a Single Organic Molecule With Dual Phosphorescence At Room Temperature. *Nature Communications* **2017**, *8*, 416.
- (11) Chen, Y. H.; Tang, K. C.; Chen, Y. T.; Shen, J. Y.; Wu, Y. S.; Liu, S. H.; Lee, C. S.; Chen, C. H.; Lai, T. Y.; Tung, S. H.; Jeng, R. J.; Hung, W. Y.; Jiao, M.; Wu, C. C.; Chou, P. T. Insight Into the Mechanism and Outcoupling Enhancement of Excimer-Associated White Light Generation. *Chemical Science* **2016**, *7*, 3556-3563.
- (12) Tang, K.-C.; Chang, M.-J.; Lin, T.-Y.; Pan, H.-A.; Fang, T.-C.; Chen, K.-Y.; Hung, W.-Y.; Hsu, Y.-H.; Chou, P.-T. Fine Tuning the Energetics of Excited-State Intramolecular Proton Transfer (Esipt): White Light Generation in a Single Esipt System. *Journal of the American Chemical Society* **2011**, *133*, 17738-17745.
- (13) Xie, Z.; Chen, C.; Xu, S.; Li, J.; Zhang, Y.; Liu, S.; Xu, J.; Chi, Z. White-light Emission Strategy of a Single Organic Compound With Aggregation-induced Emission and Delayed Fluorescence Properties. *Angewandte Chemie* **2015**, *127*, 7287-7290.
- (14) Xu, B.; Mu, Y.; Mao, Z.; Xie, Z.; Wu, H.; Zhang, Y.; Jin, C.; Chi, Z.; Liu, S.; Xu, J. Achieving Remarkable Mechanochromism and White-Light Emission With Thermally Activated Delayed Fluorescence Through the Molecular Heredity Principle. *Chemical science* **2016**, *7*, 2201-2206.
- (15) Yang, Q. Y.; Lehn, J. M. Bright White-light Emission From a Single Organic Compound in the Solid State. *Angewandte Chemie International Edition* **2014**, *53*, 4572-4577.
- (16) Yang, Y.; Lowry, M.; Schowalter, C. M.; Fakayode, S. O.; Escobedo, J. O.; Xu, X.; Zhang, H.; Jensen, T. J.; Fronczek, F. R.; Warner, I. M. An Organic White Light-Emitting Fluorophore. *Journal of the American Chemical Society* **2006**, *128*, 14081-14092.
- (17) Zhang, Z.; Wu, Y.-S.; Tang, K.-C.; Chen, C.-L.; Ho, J.-W.; Su, J.; Tian, H.; Chou, P.-T. Excited-State Conformational/electronic Responses of Saddle-Shaped N, N'-Disubstituted-dihydrodibenzo [a, C] Phenazines: Wide-Tuning Emission From Red to Deep Blue and White Light Combination. *Journal of the American Chemical Society* **2015**, *137*, 8509-8520.
- (18) Mao, Z.; Yang, Z.; Mu, Y.; Zhang, Y.; Wang, Y.; Chi, Z.; Lo, C.; Liu, S.; Lien, A.; Xu, J. Linearly Tunable Emission Colors Obtained From a Fluorescent-Phosphorescent Dual-emission Compound By Mechanical Stimuli. *Angewandte Chemie* **2015**, *127*, 6368-6371.
- (19) Shelton, A. H.; Sazanovich, I. V.; Weinstein, J. A.; Ward, M. D. Controllable Three-Component Luminescence From a 1, 8-Naphthalimide/eu (Iii) Complex: White Light Emission From a Single Molecule. *Chemical Communications* **2012**, *48*, 2749-2751.

- (20) Shao, S.; Ding, J.; Wang, L.; Jing, X.; Wang, F. White Electroluminescence From All-Phosphorescent Single Polymers on a Fluorinated Poly (Arylene Ether Phosphine Oxide) Backbone Simultaneously Grafted With Blue and Yellow Phosphors. *Journal of the American Chemical Society* **2012**, *134*, 20290-20293.
- (21) Wong, K. M.-C.; Yam, V. W.-W. Self-Assembly of Luminescent Alkynylplatinum (II) Terpyridyl Complexes: Modulation of Photophysical Properties Through Aggregation Behavior. *Accounts of chemical research* **2011**, *44*, 424-434.
- (22) Kamkaew, A.; Lim, S. H.; Lee, H. B.; Kiew, L. V.; Chung, L. Y.; Burgess, K. Bodipy Dyes in Photodynamic Therapy. *Chemical Society Reviews* **2013**, *42*, 77-88.
- (23) Wu, W.; Guo, H.; Wu, W.; Ji, S.; Zhao, J. Organic Triplet Sensitizer Library Derived From a Single Chromophore (Bodipy) With Long-Lived Triplet Excited State for Triplet-Triplet Annihilation Based Upconversion. *J. Org. Chem* **2011**, *76*, 7056-7064.
- (24) Zhang, X.-F.; Yang, X.; Niu, K.; Geng, H. Phosphorescence of Bodipy Dyes. *Journal of Photochemistry and Photobiology A: Chemistry* **2014**, *285*, 16-20.
- (25) Miller, J. C.; Meek, J. S.; Strickler, S. J. Heavy Atom Effects on the Triplet Lifetimes of Naphthalene and Phenanthrene. *Journal of the American Chemical Society* **1977**, *99*, 8175-8179.
- (26) Xu, J.; Takai, A.; Kobayashi, Y.; Takeuchi, M. Phosphorescence From a Pure Organic Fluorene Derivative in Solution At Room Temperature. *Chemical Communications* **2013**, *49*, 8447-8449.
- (27) Bolton, O.; Lee, K.; Kim, H. J.; Lin, K. Y.; Kim, J. Activating Efficient Phosphorescence From Purely Organic Materials By Crystal Design. *Nature chemistry* **2011**, *3*, 205-210.
- (28) Hirata, S.; Totani, K.; Zhang, J.; Yamashita, T.; Kaji, H.; Marder, S. R.; Watanabe, T.; Adachi, C. Efficient Persistent Room Temperature Phosphorescence in Organic Amorphous Materials Under Ambient Conditions. *Advanced Functional Materials* **2013**, *23*, 3386-3397.
- (29) Kwon, M. S.; Yu, Y.; Coburn, C.; Phillips, A. W.; Chung, K.; Shanker, A.; Jung, J.; Kim, G.; Pipe, K.; Forrest, S. R. Suppressing Molecular Motions for Enhanced Room-Temperature Phosphorescence of Metal-Free Organic Materials. *Nature communications* **2015**, *6*, 1-9.
- (30) Jung, J. Enhancing Room Temperature Phosphorescence From Organic Molecules By Internal Heavy Atom Effect and External Agents [Doctoral Dissertation, University of Michigan, Ann Arbor]. **2016**,
- (31) Kim, B.; Ma, X.; Chen, C.; Je, Y.; Coir, E. W.; Hashemi, H.; Aso, Y.; Green, P. F.; Kieffer, J.; Kim, J. Energy Level Modulation of Homo, LUMO, and Band-gap in Conjugated Polymers for Organic Photovoltaic Applications. *Advanced Functional Materials* **2013**, *23*, 439-445.
- (32) Nagai, A.; Kokado, K.; Nagata, Y.; Chujo, Y. 1, 3-Diketone-based Organoboron Polymers: Emission By Extending  $\pi$ -Conjugation Along a Polymeric Ligand. *Macromolecules* **2008**, *41*, 8295-8298.



## **Chapter 5 Accurate Prediction of Free Solvation Energy of Organic Molecules via Graph Based Machine Learning Models from Pairwise Atomistic Interactions**

### **5.1 Introduction**

The ability to predict physiochemical and biological properties of organic compounds is important for developing new materials with specific desired properties. It allows us to compute properties without time-consuming and costly experiments as well as to discover novel compounds with extraordinary characteristics. Common strategies to predict such properties are ab initio quantum mechanical simulations like Hartree-Fock (HF),<sup>1</sup> density functional theory (DFT),<sup>2,3</sup> molecular dynamics (MD),<sup>4,5</sup> and hybrid quantum mechanics/molecular mechanics (QM/MM).<sup>6,7</sup> Traditionally, these methods have been widely used to calculate various molecular properties without requiring input from experiments. High-performance computational screening based on these approaches has become routine, giving researchers the ability to simulate the properties of thousands of chemical compounds as part of a single study. However, their applications in practice may be limited considering the high computational cost of running these advanced methods, as well as the relatively large margin of error associated with them, especially for large systems.<sup>8</sup> As a result, the use of machine learning models has become more widespread as they are computationally efficient and more accurate.

Recent developments in machine learning (ML), specifically deep learning (DL), have enabled researchers to predict the structure and properties of complex materials with an accuracy comparable to computational chemistry methods.<sup>9,10</sup> A supervised ML algorithm trains a predictive model using a training set of input-output pairs so that the model is able to predict the

output given the input. Deep learning models have enabled the use of large datasets where instead of using hand-crafted features, the models are able to identify hidden patterns in the data by themselves. In materials science, machine learning is helpful in areas such as new material discovery and material property prediction.<sup>11, 12</sup> Computational chemistry simulations and experimental measurements are two conventional methods that are widely adopted in the field of materials science. However, it is difficult to use these two methods to accelerate materials discovery and design because they are often time consuming and inefficient. With the launch of the Materials Genome Initiative, a large effort has been made by material scientists to collect extensive datasets of materials properties, including pre-existing computational simulation results and experimental measurements. Machine learning techniques are then used for finding patterns in these high-dimensional data, providing a fast and reliable approach for predicting the inherent properties of a large number of candidate molecules. In recent years, ML algorithms have been widely used for material property prediction. They are often used in combination with quantum chemistry simulations such as DFT and MD for applications such as excited state dynamics,<sup>13-17</sup> solubility of organic molecules,<sup>18-21</sup> bandgap of inorganic compounds,<sup>22</sup> and thermodynamic stability.<sup>23</sup>

Using ab initio methods or MD simulations, the set of Cartesian coordinates corresponding to the atomic positions in 3D space serve as a fundamental identifier of molecules and materials structures. It is a long-recognized tenet of this discipline to relate materials properties to the geometry and energy of a molecular system, which has been amply demonstrated by solving the Schrodinger equation or Newton's equation of motion in conjunction with the formalisms of statistical thermodynamics. However, when using ML algorithms, the atomic positions in 3D space are not the only identifiers of a molecule from

which to derive its properties. In recent years, scientists have come up with various molecular representations for material property prediction.<sup>12</sup> Some of these different molecular representations are: (1) SMILES<sup>24, 25</sup> that uses short character strings to describe the structure of chemical species; (2) Extended Connectivity Fingerprints (ECFPs)<sup>26, 27</sup> that breaks molecules into local neighborhoods and hashes them into a bit vector of an specified size; (3) Electronic density<sup>28, 29</sup> which is the measure of the probability of an electron being present at an infinitesimal element of space; (4) Coulomb matrix<sup>10</sup> which reflect the forces between each pair of atoms; (5) 3D geometry which is similar to inputs for DFT and MD simulations; (6) Bag of bonds and fragments; (7) Chemical environments;<sup>30</sup> and etc. The advantage of ML algorithms is that they can utilize a variety of molecular representations, giving scientists the ability to select the best representation for the property of interest. In addition to the references cited above, we recommend references<sup>31-33</sup> for readers interested in these topics.

Among the possible choices, molecules can be expressed in the form of graphs, with the inclusion of the chemical information. Graphs provide a natural way of describing molecular structures, e.g., representing atoms by nodes and chemical bonds by edges. In addition, basic chemical information can be encoded in the molecular graphs. This chemical information includes atomic features such as atom type and ionic radius, bond features such as bond type and conjugation, and molecular features such as polarity and molecular weight. Then, a graph-based DL procedure such as Graph Neural Network (GNN) can be used to train a model. Graph theoretical approaches have been widely used to analyze chemical compounds,<sup>34</sup> crystal structures, and even for the representation of reactions.<sup>35</sup>

Solvation free energy is the free energy change associated with the transfer of a solute molecule from ideal gas to a solvent at specific pressure and temperature. Solvation free energy,

which describes the interaction between solvent and dissolved molecules, is an important index in the fields of organic synthesis,<sup>36, 37</sup> medicinal chemistry,<sup>38, 39</sup> drug delivery,<sup>40</sup> electrochemical redox reactions,<sup>41, 42</sup> biological processes such as DNA and protein interaction,<sup>43</sup> protein folding,<sup>44</sup> electronic and vibrational properties of biomolecules,<sup>45, 46</sup> etc. Accurate solvation free energy determination is a time-consuming and costly process. It would be particularly useful to assess solvation free energy in the absence of a physical sample as some molecules can be difficult or time-consuming to synthesize. ML models can predict multiple molecular properties prior to synthesis, avoiding the process entirely for molecules that do not demonstrate the desired properties. This can be helpful for many material design applications including developing metal-free organic emissive materials.

Recent studies demonstrated that ML models can successfully predict the solvation free energy of solutes in aqueous solutions (aka hydration free energy).<sup>20, 21, 47</sup> Most of these ML models show an accuracy better than or comparable to ab initio simulations. ML models also require much shorter calculation time than computer simulations. While computational chemistry simulations can take up to a day for a single calculation, ML models can predict the solvation free energy of thousands of molecules in a few hours using a personal computer. Unfortunately, most ML models for solvation have been limited to aqueous solutions.

In the present work, we introduce a novel approach for predicting solvation free energy of solvent-solute pairs. Herein, we have used the graph-based models: Message Passing Neural Network (MPNN) and Graph Attention Network (GAT). The results demonstrate that our graph-based models outperform the descriptor-based models and other graph-based models in the literature in terms of prediction accuracy and computational efficiency. The novelty of our model is that we take pair-wise interactions of solute and solvent into consideration. We believe

this methodology can be applied in other molecular property prediction beyond solvation free energy.

This chapter is organized as follows: section 2 describes the embedding method for graph representation of molecules, a brief introduction on how MPNN and GAT models work, and feature aggregation. In section 3, the model architecture, our results, and the performance of each approach are demonstrated in detail. In section 4, we discuss the novelty of our models, their sources of error, and compare their performance with both MD and DFT simulation, as well as other ML models. In the last section, we conclude our work and discuss directions for future work.

## 5.2 Methods

### 5.2.1 Graph Representation of Molecules

In graph neural networks, the first step is to encode the molecule as a graph. In graph representation of molecule, the atoms and bonds that make up a molecule are mapped into sets of nodes and edges. The graph is then augmented by the given information of the molecule which is stored as node (atom) features and edge (bond) features.

**Node Features:** We use 8 features for each node where, after converting categorical features to one-hot vectors, each node is represented by a 31-dimensional vector. These 8 features are:

1. The type of the atom is encoded as a 10-dimensional one-hot vector where the 10 choices are: Carbon, Nitrogen, Oxygen, Fluorine, Phosphorus, Sulfur, Chlorine, Bromine, Iodine, or other atoms.
2. The formal charge of the atom represented as an integer.

3. Hybridization of the atom encoded as a 3-dimensional one-hot vector with categories “sp,” “sp2,” and “sp3.”
4. Hydrogen bonding: A one-hot vector of whether this atom is a hydrogen bond donor or acceptor.
5. Aromatic: A one-hot vector of whether the atom belongs to an aromatic ring.
6. Degree: A one-hot vector of the degree (0-5) of the atom. Degree is the number of bonded neighbors.
7. Number of Hydrogens: A one-hot vector of the number of hydrogens (0-4) to which the atom is connected.
8. Calculated Partial charge.

Edge features: Each edge between the nodes in the graph contains 4 features. After converting the categorical features to one-hot vectors, each edge is represented by a 11-dimensional vector. These 4 features are:

1. Bond type: A one-hot vector of the bond type, “single,” “double,” “triple,” or “aromatic.”
2. Same ring: A one-hot vector of whether the atoms in the pair are in the same ring.
3. Conjugated: A one-hot vector of whether the bond is conjugated or not.
4. Stereo: A one-hot vector of the stereo configuration of a bond.

In Figure 5-1 we have shown the molecule 2-Nitrotoluene as an example. It can be noted that the features are either numerical or categorical. The categorical features are encoded as one-hot vectors, e.g., if there are five possible categories and the atom (or edge) is of category three, that feature is represented by a 5-dimensional vector where the third element is one and the rest is zero.

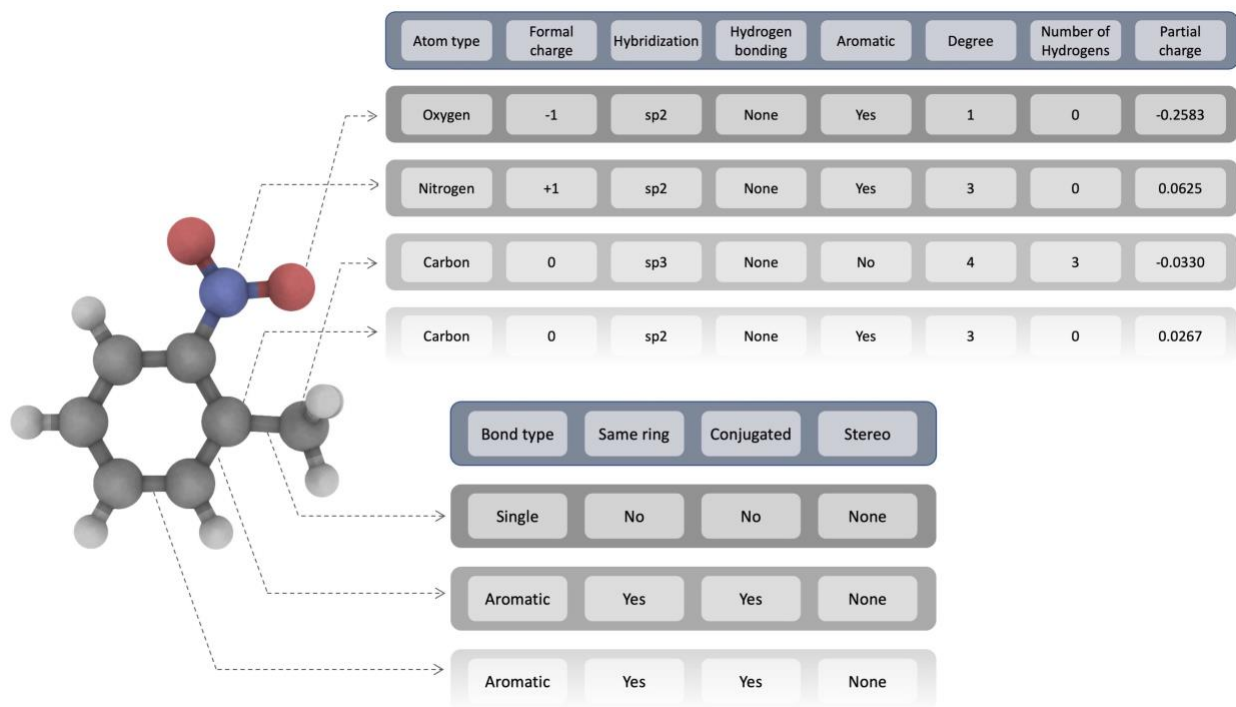


Figure 5-1. Example of node (atom) and edge (bond) features for a sample molecule, 2-Nitrotoluene.

Once the molecule is transformed into its graph representation, it is fed into the encoder layer of the model. As we detail below, we use two different encoder models: MPNN and GAT. Each of these models take the graph object as input and output a learned representation of it such that the information of different atoms and edges are aggregated.

### 5.2.2 Message Passing Neural Network (MPNN)

In this work, we utilize and train an MPNN<sup>48, 49</sup> architecture to generate vectors representing solvent and solute molecules. In this section we describe the MPNN framework in more detail. Let  $G$  be the graph representation of a molecule (solute or solvent), where for each node  $v$  we have its feature vector  $h_v^0$ , and for each edge  $w$  we have its feature vector  $e_{vw}$ . The MPNN model goes through a number of message passing steps where at each step  $t$ , the node  $v$ 's feature vector is updated to. The update rule is:

$$m_v^{t+1} = \sum_{w \in N(v)} M_t(h_v^t, h_w^t, e_{vw})$$

$$h_v^{t+1} = U_t(h_v^t, m_v^{t+1})$$

where  $N(v)$  denotes to the  $v$ 's neighboring nodes in  $G$ , and  $M_t$  and  $U_t$  are arbitrary functions that depends on hidden states and edges of the neighbouring nodes. For readers interested in further reading on this we recommend references cited above.

As mentioned above, the size of the vectors in our problem is 31 (the number of the features after converting categorical features to one-hot vectors). However, the size of the feature vectors after message passing phase is set to be 64. This is a hyperparameter that can be tuned. The message passing phase runs for  $t = 6$  iteration steps which is defined as the number of times we update the output vector representation for each node.

### 5.2.3 Graph Attention Network (GAT)

Introduced in reference [50], the GAT model is made of graph attention layers. A graph attention layer maps a set of node features to a new set of node features using a soft-attention mechanism. In short, for a given node, the graph attention layer outputs a weighted average of it and its neighbors' features where the weights are not fixed and are input-dependent. More specifically, for a given node  $v$  and its feature-vector  $h_v \in \mathbb{R}^F$ , the graph attention mechanism outputs  $h'_v \in \mathbb{R}^{F'}$  where:

$$h'_v = \sum_{w \in N(v)} \alpha_{vw} W h_w$$

where  $w \in \mathbb{R}^{F' \times F}$  is a projection matrix and  $F'$  is the dimension of hidden features. In many cases, a non-linearity is also applied to the linear combination. The attention mechanism works



such that the weights  $\alpha_{vw}$  are determined based on the graph features. To make sure the weights are normalized, they are computed using a softmax formula:

$$\alpha_{vi} = \frac{e^{l(a^T [Wh_v || Wh_i])}}{\sum_{w \in N(v)} e^{l(a^T [Wh_v || Wh_w])}}$$

where  $l$  is an activation function (we use the LeakyReLU function),  $||$  stands for concatenation, and  $a$  is a parameter vector in  $\mathbb{R}^{2F}$ . The extension of a graph attention layer to multi-head attention is performed by using several projection matrices and then concatenating the resulting hidden features.

Looking at the above formulas, it is clear that the attention mechanism adds a large amount of flexibility to the model architecture; unlike graph convolutional layers, the attention layer is capable of assigning different levels of importance to each of the neighboring nodes in a dynamic fashion. Furthermore, it adds interpretability to the model as one can investigate the neighbors that get the highest weight. In our exploration, we use a GAT model with two attention layers for the solvent and solute encoders with  $F' = 42$  for both layers of the solvent encoder and  $F' = 12$  for both layers of the solute model. We use multi-headed attention with 4 heads in all layers of both models.

#### 5.2.4 Feature Aggregation

After passing the molecule graph through GAT or MPNN models, the encoded output is a matrix with a size of [number of nodes  $\times$  64]. The main problem is that different molecules will be encoded into representations of different sizes, since different molecules have different number of nodes. To be able to feed this representation into existing neural network architectures (e.g. feed-forward layer), it is necessary to aggregate the information in the encoded graph representations of different size into a feature-vector with a fixed size. To provide this capability,

we use the set2set by Vinyals et al.,<sup>51</sup> and weightedsum&max (as implemented in DGL package<sup>52</sup>) readout functions for MPNN and GAT models, respectively. Given the encoded graph, the set2set (or weightedsum&max) layer computes a feature-vector for the whole graph using a readout function R:

$$\hat{y} = R(\{h_v^T | v \in G\}).$$

Further using the MPNN (or GAT) model, the input graph is encoded into a graph represented by a matrix with a size of [number of nodes  $\times$  64]. The set2set (or weightedsum&max) layer maps this matrix into a vector size of 128.

The final step is to aggregate the information of the solvent and solute molecules and make a prediction. This is done by simply concatenating the two molecules' feature vectors and then passing it through a multilayer perceptron (MLP) layer. The MLP layer then outputs the predicted solvation energy. The overall flow of the model is shown in Figure 5-2. Note that the message function Mt, update function Ut, graph attention mechanism, and the readout functions are all learned differentiable functions.

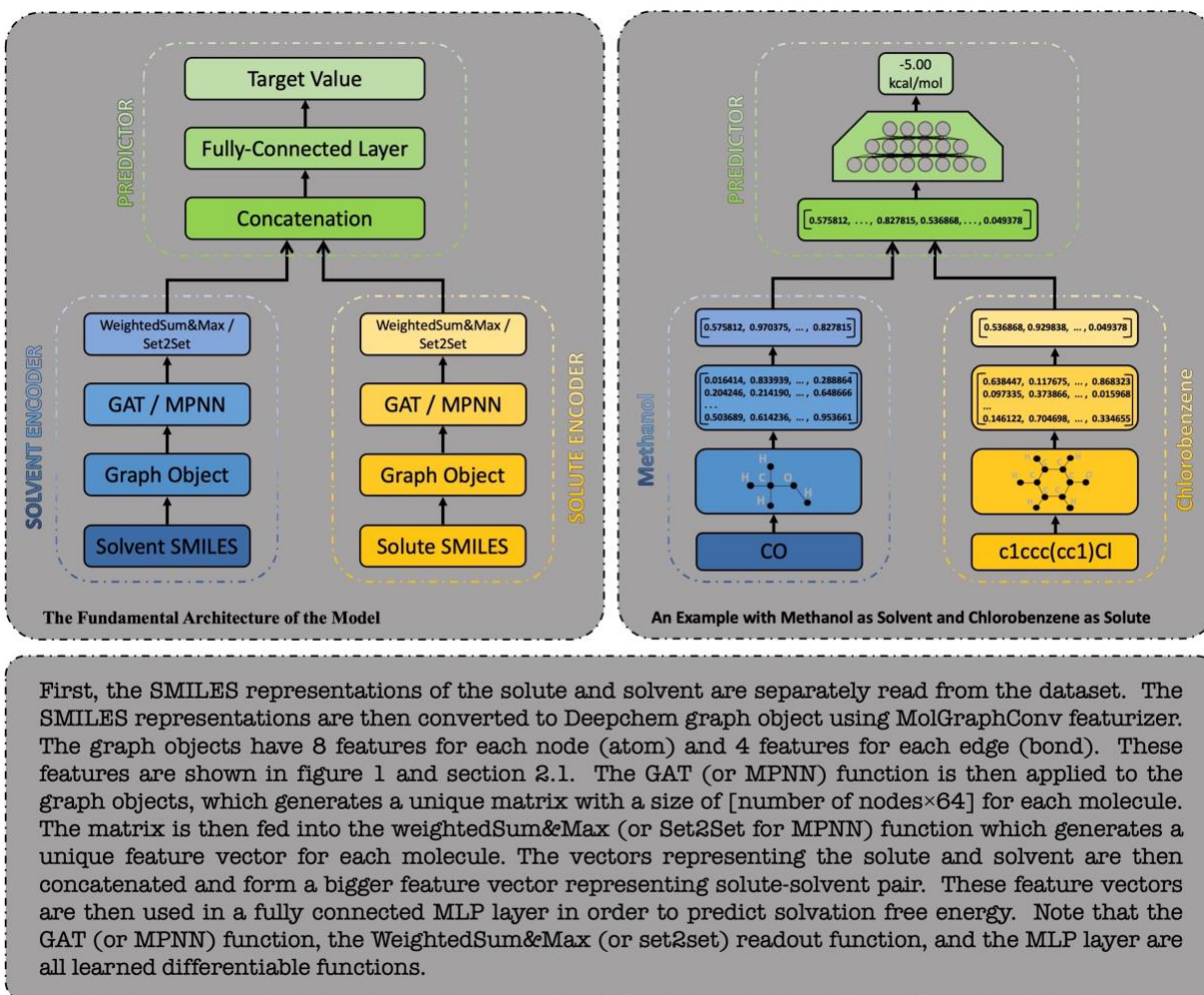


Figure 5-2. The fundamental architecture of the model (top left), an example of the model with methanol as the solvent and chlorobenzene as the solute (top right), and an explanation describing how the model works (bottom).

### 5.3 Computational Setup and Results

In this study, 5,952 data points for non-aqueous solvents are collected from the Solv@TUM database version 1.0.<sup>53-56</sup> This dataset contains a collection of experimentally measured partition coefficients for a large number of molecular solutes in non-aqueous solvents. There are 657 unique organic solvents and 146 unique organic solutes. The partition coefficients are then converted to solvation free energies in kcal/mol. Finally, the SMILES representation of 5,952 solute-solvent pairs and their solvation free energy in kcal/mol are prepared for the machine learning input. Because the Solv@TUM dataset only contains common names of the

solvents, an automated search is performed using PubChemPy<sup>57</sup> library in order to obtain the SMILES strings of the compounds. For a small fraction of molecules, less than 1%, whose compound names are not valid in PubChem database, their SMILES strings are manually added to the dataset.

For implementation of the neural network, we use PyTorch framework. At the very first stage (Figure 2), the SMILES representations are converted to a Deepchem graph object using the MolGraphConv<sup>58</sup> featurizer as implemented in Deepchem.<sup>59</sup> The graph objects have 8 features for each node (atom) and 4 features for each edge (bond). The MPNN (or GAT) function is then applied to the graph objects, which generates a unique matrix for each molecule. The resulting matrix is then fed into a readout phase which computes a feature vector for the whole graph using a given readout function (MPNN uses set2set and GAT uses WeightedSumAndMax). Then we concatenate the vectors representing each solute and solvent pair. The resulting vector is then used in a MLP model to predict the solvation free energy. The MLP consists of 3 hidden layers, with 256, 256, and 128 hidden neurons, respectively.

The dataset is split into train, validation, and test sets in an 8:1:1 ratio. The train set has been used for training the models, while the validation set is used to give an estimate of model accuracy while tuning the model's hyperparameters. We perform an extensive grid search for tuning hyperparameters: learning rates, learning algorithms, and dimensions of hidden layers. We choose the stochastic gradient descent (SGD) algorithm with Nesterov momentum, whose learning rate is 0.02, and 0.005 and momentum is 0.9, and 0.9 for the MPNN and GAT models, respectively. We also added a cosine annealing scheduler<sup>60</sup> to the optimizer. The test set is then used to give an unbiased estimate of the accuracy of the final tuned model. To minimize the variance of the test runs we take an average of results over 10 independent runs.

The performance of the two proposed models is shown in Figure 5-3. For comparison, the performances of two other ML models proposed by Lim & Jung<sup>25, 61</sup> are also shown in this figure. We can see that both of our novel models perform better than the two example models proposed in the literature. Moreover, from Figure 5-3, we can also see that the prediction errors for the MPNN model are 0.38 kcal/mol in RMSE and 0.22 kcal/mol in MAE, while results from the GAT model have an error of 0.25 kcal/mol in RMSE and 0.14 kcal/mol in MAE. Together, these results indicate that the GAT architecture is the more suitable novel model for free solvation energy prediction. Our GAT model has the lowest error obtained in any classical, quantum-mechanical, or ML based model for free solvation energy prediction.

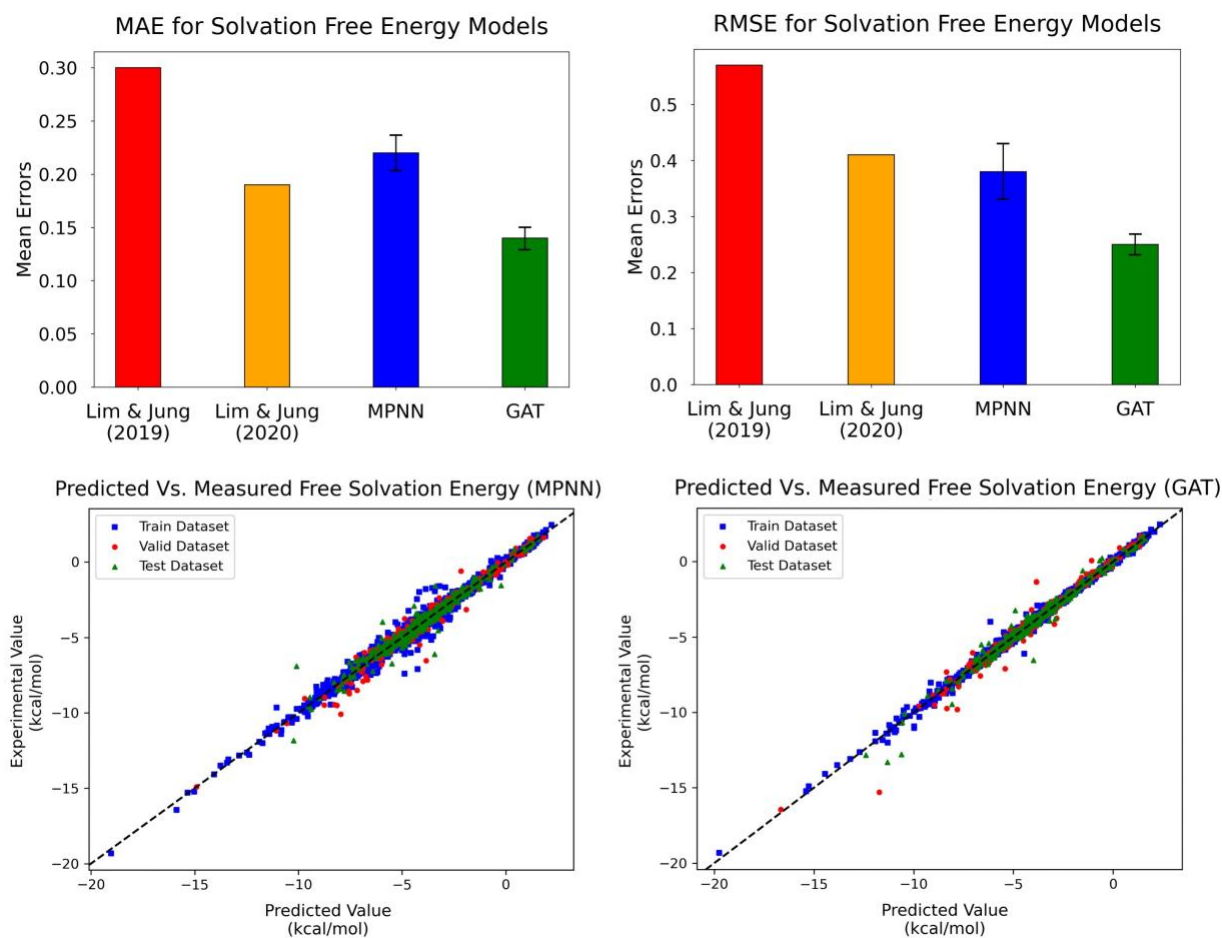


Figure 5-3. Figure 3: MAE (top left) and RMSE (top right) for Solvation free energy models for test dataset. MPNN and GAT are done in this study. Scatter plot for true (y-axis) and ML predicted (x-axis) values of solvation energies for MPNN (bottom left), and GAT (bottom right). All results are averaged over 10 independent runs.

## 5.4 Discussion

In recent years, researchers have been widely used DFT,<sup>62, 63</sup> MD,<sup>64</sup> and QM/MM<sup>65</sup> simulations to predict the solvation free energy of organic molecules in various solvents. Despite the initial success of these methods, they are computationally expensive, often taking days to process one calculation. Additionally, they are complicated to set up even for experts; one needs to benchmark a variety of functional and basis sets (for DFT simulations), and force fields (for MD simulations) to find the best hyperparameters for the simulations. Furthermore, these hyperparameters are usually different from molecule to molecule, meaning that new hyperparameters must be set for every molecular system. Finally, these computational chemistry methods show a low accuracy with a mean absolute error (MAE) in the range of 0.6-1.0 kcal/mol.<sup>23</sup> However, our GAT and MPNN models are computationally cheaper and easier to set up with a much lower MAE of 0.14 and 0.22 kcal/mol, respectively.

Figure 5-4 shows the MAE and the number of compounds in the dataset for different solvents. The MAE is calculated based on the prediction of the test dataset. As can be seen from this figure, the MAE tends to be larger for the solvents that present less in the dataset. For example, the solvents 2-Ethylhexanol, M-cresol, and 2-Picoline only represent 2, 5, and 6 of the total number of compounds in the dataset and have an average absolute error of 3.51, 1.43, and 0.73 kcal/mol, respectively. Clearly, the more data points that are available for each solvent, the lower the mean absolute error. To lower the MAE for all solvents to more equitable levels, we must gather more extensive data for each solvent.

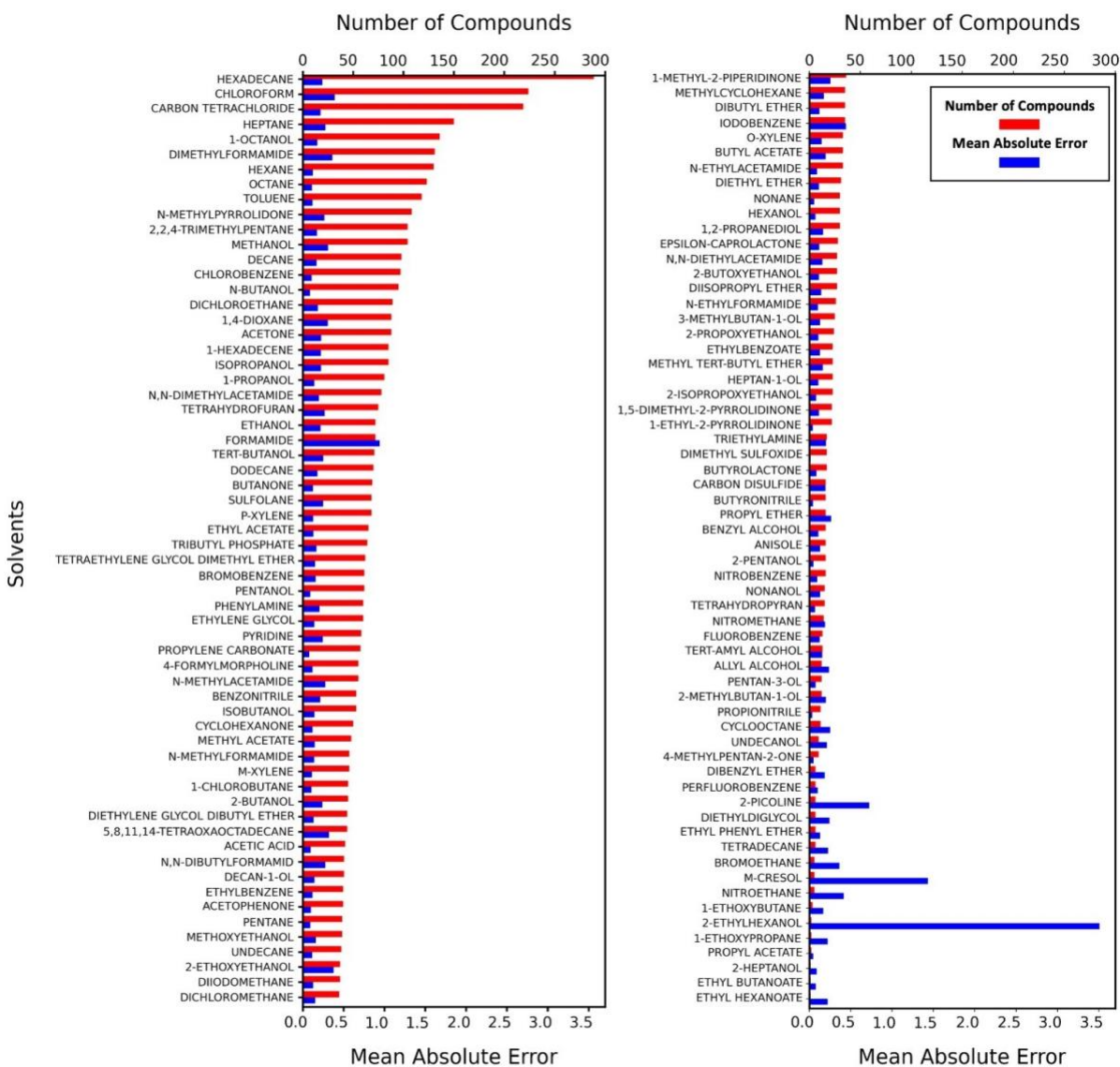


Figure 5-4. The mean absolute error and the number of compounds in the dataset for different solvents. The mean absolute error is calculated based on the prediction of the test dataset. The mean absolute error tends to be larger for the solvents that present less in the dataset.

The Solv@TUM database contains a collection of experimentally measured solvation free energy of solutes in non-aqueous solvents. The data has been compiled from the works of at least 68 references. It is apparent that each entry has been measured in somewhat different experimental conditions, with different equipment. Moreover, each entry has been measured by different researchers and it is obvious that there might be some procedural error in the

experimental values as well. We believe that since our model is trained based on this dirty and coarse data, the small MAE of 0.14 kcal/mol for the GAT model is somewhat inevitable. Moreover, our model's error is in the range of the measurement errors of experimentally measured solvation free energies. Thus, it would not be realistic to have a lower prediction error.

A validation dataset is a sample of data held back from model training that is used to give an estimate of model accuracy, while it simultaneously serves to tuning the model's hyperparameters. The test dataset is also held back from the model training but, in contrast, it is used to give an unbiased estimate of the accuracy of the final tuned model. There has been a trend in literature, especially in material property prediction, that researchers disregard validation datasets and use test datasets for both hyperparameter tuning and reporting the accuracy of the final tuned model. We believe that for an unbiased model training, it is crucial for any ML study to have validation and test datasets. Unlike the work done by Lim & Jung<sup>25, 61</sup> for solvation free energy prediction and some other studies for material property prediction, we used the validation dataset for hyperparameter tuning and we reported the accuracy of the model using the test dataset. We believe that this approach should also be employed by other researchers so that an unbiased estimate of the skill of the final tuned model could be computed.

There exist descriptor-based ML models, which rather than encoding the structure of a compound as a graph, instead the physicochemical, structural, and electronic properties of compounds are separately calculated and manually added to the model.<sup>66</sup> The Dragon software,<sup>67</sup> for example, can calculate 5,270 molecular descriptors. These molecular descriptors are then used as input features to predict the property of interest. However, having this many features may not be effective, as they increase the complexity of the model while it may not help much to improve the prediction accuracy. Moreover, the descriptors could be strongly



correlated; for example, adding atomic mass as an additional feature might not be useful since it is straightforwardly mapped to the atom types and thus already reflected in the atom type information. Moreover, some of the features might be irrelevant to determining the property of interest, and therefore negatively impact model performance. For example, in the free solvation energy prediction features like "ring bridge count" might be totally extraneous. Therefore, researchers should extensively search and find those features which contribute most to the prediction variable in which we are interested in, while at the same time try to reduce overfitting, improve accuracy, and reduce training time. This makes setting up the ML model so difficult and exclusive to the prediction output. On the other hand, the graph molecular representation used in this work, only requires 8 and 4 features for each atom and bond, respectively. The graph-based models are capable of generating and evaluating the physicochemical, structural, and electronic properties of the compounds using this minimal number of features. Using the graph structure and the given atom and bond features, these models directly compute a feature vector of desired size, which perfectly predicts the property of interest with a significantly low error. This makes the ML setup so easy, fast, and, more importantly, flexible so that it can be used for any desired molecular property prediction.

## 5.5 Conclusions

In this study, two novel deep learning architectures, MPNN and GAT, are applied for free solvation energy predictions. Each solute-solvent pair molecule is first converted to graph objects. Each node (atom) has 8 atomic features: atom types, formal charges, hybridization, hydrogen bonding, aromaticity, degree, number of hydrogens, and partial charge. Each edge (bond) has 4 features: bond type, same ring, conjugation, and stereo configuration. Then MPNN (or GAT) are applied to the solute and solvent pair separately. The resulting vector feature

representing solute and solvent are then concatenated and used in an MLP layer to predict the solvation free energy. Our deep learning architectures show better prediction than state of the art deep learning and quantum mechanical methods in terms of RMSE and MAE. The MPNN model has an error of 0.38 kcal/mol in RMSE and 0.22 kcal/mol in MAE, while results from the GAT model show an error of 0.25 kcal/mol in RMSE and 0.14 kcal/mol in MAE. This is the most accurate free solvation energy calculation in the literature to the best of our knowledge.

Most of the deep learning methods for solubility and solvation free energy only consider one solvent. The novelty of our neural network model is that we take pair-wise interaction of solute and solvent into consideration. We believe our architecture can be used for pair-wise interactions such as solvent-solute, protein-ligand, etc. Also, unlike chemical descriptor-based models, our neural network architecture can find the physicochemical and molecular properties needed for solvation free energy calculations with only a few atom and bond features. This makes our model so flexible that can be used to learn and predict various molecular properties. This methodology can be applied in other molecular property predictions beyond solvation free energy. We believe such promising predictive models will be applicable to enhancing the efficiency of the screening of drug molecules, essentially as a useful tool to promote the development of molecular pharmaceuticals.

## 5.6 References

- (1) Pablo Echenique and José Luis Alonso. A mathematical and computational review of hartree–fock scf methods in quantum chemistry. *Molecular Physics*, 105(23-24):3057–3098, 2007.
- (2) Robert G Parr. Density functional theory of atoms and molecules. In *Horizons of quantum chemistry*, pages 5–15. Springer, 1980.
- (3) Kieron Burke. Perspective on density functional theory. *The Journal of chemical physics*, 136(15):150901, 2012.

- (4) MC Payne, JD Joannopoulos, DC Allan, MP Teter, and David H Vanderbilt. Molecular dynamics and ab initio total energy calculations. *Physical review letters*, 56(24):2656, 1986.
- (5) Eric Paquet and Herna L Viktor. Molecular dynamics, monte carlo simulations, and langevin dynamics: a computational review. *BioMed research international*, 2015, 2015.
- (6) Jiali Gao, Mark A Thompson, et al. *Combined quantum mechanical and molecular mechanical methods*, volume 712. ACS Publications, 1998.
- (7) Laura E Ratcliff, Stephan Mohr, Georg Huhs, Thierry Deutsch, Michel Masella, and Luigi Genovese. Challenges in large scale quantum mechanical calculations. *Wiley Interdisciplinary Reviews: Computational Molecular Science*, 7(1):e1290, 2017.
- (8) Matthew D Wodrich, Clémence Corminboeuf, Peter R Schreiner, Andrey A Fokin, and Paul von Rague Schleyer. How accurate are dft treatments of organic energies? *Organic letters*, 9(10):1851–1854, 2007.
- (9) Siwar Chibani and François-Xavier Coudert. Machine learning approaches for the prediction of materials properties. *APL Materials*, 8(8):080701, 2020.
- (10) Matthias Rupp, Alexandre Tkatchenko, Klaus-Robert Müller, and O Anatole Von Lilienfeld. Fast and accurate modeling of molecular atomization energies with machine learning. *Physical review letters*, 108(5):058301, 2012.
- (11) Keith T Butler, Daniel W Davies, Hugh Cartwright, Olexandr Isayev, and Aron Walsh. Machine learning for molecular and materials science. *Nature*, 559(7715):547–555, 2018.
- (12) Benjamin Sanchez-Lengeling and Alán Aspuru-Guzik. Inverse molecular design using machine learning: Generative models for matter engineering. *Science*, 361(6400):360–365, 2018.
- (13) Raghunathan Ramakrishnan, Mia Hartmann, Enrico Tapavicza, and O Anatole Von Lilienfeld. Electronic spectra from tddft and machine learning in chemical space. *The Journal of chemical physics*, 143(8):084111, 2015.
- (14) Julia Westermayr and Philipp Marquetand. Machine learning for electronically excited states of molecules. *Chemical Reviews*, 2020.
- (15) Julia Westermayr, Michael Gastegger, and Philipp Marquetand. Combining schnet and sharc: The schnarc machine learning approach for excited-state dynamics. *The journal of physical chemistry letters*, 11(10):3828–3834, 2020.
- (16) Rafael Gómez-Bombarelli, Jorge Aguilera-Iparraguirre, Timothy D Hirzel, David Duvenaud,
- (17) Dougal Maclaurin, Martin A Blood-Forsythe, Hyun Sik Chae, Markus Einzinger, Dong-Gwang Ha, Tony Wu, et al. Design of efficient molecular organic light-emitting diodes by a highthroughput virtual screening and experimental approach. *Nature materials*, 15(10):1120–1127, 2016.
- (18) Wiktor Pronobis, Kristof T Schütt, Alexandre Tkatchenko, and Klaus-Robert Müller. Capturing intensive and extensive dft/tddft molecular properties with machine learning. *The European Physical Journal B*, 91(8):1–6, 2018.

- (19) Peng Gao, Jie Zhang, Yuzhu Sun, and Jianguo Yu. Accurate predictions of aqueous solubility of drug molecules via the multilevel graph convolutional network (mgcn) and schnet architectures. *Physical Chemistry Chemical Physics*, 22(41):23766–23772, 2020.
- (20) Jarmo Huuskonen. Estimation of aqueous solubility for a diverse set of organic compounds based on molecular topology. *Journal of Chemical Information and Computer Sciences*, 40(3):773–777, 2000.
- (21) Alessandro Lusci, Gianluca Pollastri, and Pierre Baldi. Deep architectures and deep learning in chemoinformatics: the prediction of aqueous solubility for drug-like molecules. *Journal of chemical information and modeling*, 53(7):1563–1575, 2013.
- (22) John S Delaney. Esol: estimating aqueous solubility directly from molecular structure. *Journal of chemical information and computer sciences*, 44(3):1000–1005, 2004.
- (23) Joohee Lee, Atsuto Seko, Kazuki Shitara, Keita Nakayama, and Isao Tanaka. Prediction model of band gap for inorganic compounds by combination of density functional theory calculations and machine learning techniques. *Physical Review B*, 93(11):115104, 2016.
- (24) Jonathan Schmidt, Jingming Shi, Pedro Borlido, Liming Chen, Silvana Botti, and Miguel AL Marques. Predicting the thermodynamic stability of solids combining density functional theory and machine learning. *Chemistry of Materials*, 29(12):5090–5103, 2017.
- (25) David Weininger, Arthur Weininger, and Joseph L Weininger. Smiles. 2. algorithm for generation of unique smiles notation. *Journal of chemical information and computer sciences*, 29(2):97–101, 1989.
- (26) Hyuntae Lim and YounJoon Jung. Delfos: deep learning model for prediction of solvation free energies in generic organic solvents. *Chemical science*, 10(36):8306–8315, 2019.
- (27) David Duvenaud, Dougal Maclaurin, Jorge Aguilera-Iparraguirre, Rafael Gómez-Bombarelli, Timothy Hirzel, Alán Aspuru-Guzik, and Ryan P Adams. Convolutional networks on graphs for learning molecular fingerprints. *arXiv preprint arXiv:1509.09292*, 2015.
- (28) David Rogers and Mathew Hahn. Extended-connectivity fingerprints. *Journal of chemical information and modeling*, 50(5):742–754, 2010.
- (29) RG Parr and W Yang. Density-functional theory of atoms and molecules new york: Oxford univ, 1989.
- (30) Matthew Hirn, Stéphane Mallat, and Nicolas Poilvert. Wavelet scattering regression of quantum chemical energies. *Multiscale Modeling & Simulation*, 15(2):827–863, 2017.
- (31) Albert P Bartók, Risi Kondor, and Gábor Csányi. On representing chemical environments. *Physical Review B*, 87(18):184115, 2013.
- (32) Laurianne David, Amol Thakkar, Rocío Mercado, and Ola Engkvist. Molecular representations in ai-driven drug discovery: a review and practical guide. *Journal of Cheminformatics*, 12(1):1–22, 2020.
- (33) Peter Ertl. Molecular structure input on the web. *Journal of cheminformatics*, 2(1):1–9, 2010.
- (34) Adam C Mater and Michelle L Coote. Deep learning in chemistry. *Journal of chemical information and modeling*, 59(6):2545–2559, 2019.

- (35) Jie Zhou, Ganqu Cui, Zhengyan Zhang, Cheng Yang, Zhiyuan Liu, Lifeng Wang, Changcheng Li, and Maosong Sun. Graph neural networks: A review of methods and applications. *arXiv preprint arXiv:1812.08434*, 2018.
- (36) Connor W Coley, Wengong Jin, Luke Rogers, Timothy F Jamison, Tommi S Jaakkola, William H Green, Regina Barzilay, and Klavs F Jensen. A graph-convolutional neural network model for the prediction of chemical reactivity. *Chemical science*, 10(2):370–377, 2019.
- (37) Christian Reichardt and Thomas Welton. *Solvents and solvent effects in organic chemistry*. John Wiley & Sons, 2011.
- (38) Edward M Arnett, WG Bentrude, John J Burke, and Peter McC Duggleby. Solvent effects in organic chemistry. v. molecules, ions, and transition states in aqueous ethanol1. *Journal of the American Chemical Society*, 87(7):1541–1553, 1965.
- (39) Christopher A Lipinski, Franco Lombardo, Beryl W Dominy, and Paul J Feeney. Experimental and computational approaches to estimate solubility and permeability in drug discovery and development settings. *Advanced drug delivery reviews*, 23(1-3):3–25, 1997.
- (40) Amjad Alhalaweh, Lilly Roy, Naír Rodríguez-Hornedo, and Sitaram P Velaga. pH-dependent solubility of indomethacin–saccharin and carbamazepine–saccharin cocrystals in aqueous media. *Molecular pharmaceutics*, 9(9):2605–2612, 2012.
- (41) Jonathan W Steed and Jerry L Atwood. *Supramolecular chemistry*. John Wiley & Sons, 2013.
- (42) Jihyeon Kim, Sunghyun Ko, Chanwoo Noh, Heechan Kim, Sechan Lee, Dodam Kim, Hyeokjun Park, Giyun Kwon, Giyeong Son, Jong Wan Ko, et al. Biological nicotinamide cofactor as a redox-active motif for reversible electrochemical energy storage. *Angewandte Chemie International Edition*, 58(47):16764–16769, 2019.
- (43) Takashi Takeda, Ryosuke Taniki, Asuna Masuda, Itaru Honma, and Tomoyuki Akutagawa. Electron-deficient anthraquinone derivatives as cathodic material for lithium ion batteries. *Journal of Power Sources*, 328:228–234, 2016.
- (44) Alexandros Chremos and Jack F Douglas. Polyelectrolyte association and solvation. *The Journal of chemical physics*, 149(16):163305, 2018.
- (45) CN Pace and BA Shirley. Forces contributing proteins of proteins. *Faseb*, 10(1):75–83, 1996.
- (46) Alireza Mashaghi, Pouya Partovi-Azar, Tayebah Jadidi, Nasser Nafari, Philipp Maass, M Reza Rahimi Tabar, Mischa Bonn, and Huib J Bakker. Hydration strongly affects the molecular and electronic structure of membrane phospholipids. *The Journal of chemical physics*, 136(11):03B611, 2012.
- (47) Alireza Mashaghi, P Partovi-Azar, Tayebah Jadidi, Nasser Nafari, Keivan Esfarjani, Philipp Maass, M Reza Rahimi Tabar, Huib J Bakker, and Mischa Bonn. Interfacial water facilitates energy transfer by inducing extended vibrations in membrane lipids. *The Journal of Physical Chemistry B*, 116(22):6455–6460, 2012.
- (48) Zhenqin Wu, Bharath Ramsundar, Evan N Feinberg, Joseph Gomes, Caleb Geniesse, Aneesh S Pappu, Karl Leswing, and Vijay Pande. Moleculenet: a benchmark for molecular machine learning. *Chemical science*, 9(2):513–530, 2018.

- (49) Zonghan Wu, Shirui Pan, Fengwen Chen, Guodong Long, Chengqi Zhang, and S Yu Philip. A comprehensive survey on graph neural networks. *IEEE transactions on neural networks and learning systems*, 2020.
- (50) Justin Gilmer, Samuel S Schoenholz, Patrick F Riley, Oriol Vinyals, and George E Dahl. Neural message passing for quantum chemistry. In *International Conference on Machine Learning*, pages 1263–1272. PMLR, 2017.
- (51) Petar Velicković, Guillem Cucurull, Arantxa Casanova, Adriana Romero, Pietro Liò, and Yoshua Bengio. Graph Attention Networks. *International Conference on Learning Representations*, 2018.
- (52) Oriol Vinyals, Samy Bengio, and Manjunath Kudlur. Order matters: Sequence to sequence for sets. *arXiv preprint arXiv:1511.06391*, 2015.
- (53) Minjie Wang, Da Zheng, Zihao Ye, Quan Gan, Mufei Li, Xiang Song, Jinjing Zhou, Chao Ma, Lingfan Yu, Yu Gai, et al. Deep graph library: A graph-centric, highly-performant package for graph neural networks. *arXiv preprint arXiv:1909.01315*, 2019.
- (54) Christoph Hille, Stefan Ringe, Martin Deimel, Christian Kunkel, William E Acree, Karsten Reuter, and Harald Oberhofer. Generalized molecular solvation in non-aqueous solutions by a single parameter implicit solvation scheme. *The Journal of chemical physics*, 150(4):041710, 2019.
- (55) Mikhail A Stolov, Ksenia V Zaitseva, Mikhail A Varfolomeev, and William E Acree. Enthalpies of solution and enthalpies of solvation of organic solutes in ethylene glycol at 298.15 k: prediction and analysis of intermolecular interaction contributions. *Thermochimica Acta*, 648:91–99, 2017.
- (56) Igor A Sedov, Timur M Salikov, Anisha Wadawadigi, Olivia Zha, Ellen Qian, William E Acree Jr, and Michael H Abraham. Abraham model correlations for describing the thermodynamic properties of solute transfer into pentyl acetate based on headspace chromatographic and solubility measurements. *The Journal of Chemical Thermodynamics*, 124:133–140, 2018.
- (57) Christoph (1) Hille, Stefan (2) Ringe, Martin (1) Deimel, Christian (1) Kunkel, William E. (3) Acree, Karsten (1) Reuter, and Harald (1) Oberhofer. Solv@tum v 1.0, 2018.
- (58) Matt Swain, Eka A. Kurniawan, Zach Pawers, Hsiao Yi, Leonardo Lazzaro, Björn Dahlgren, and Rickard Sjorgen. Pubchempy. <https://github.com/mcs07/PubChemPy>, 2014.
- (59) Steven Kearnes, Kevin McCloskey, Marc Berndl, Vijay Pande, and Patrick Riley. Molecular graph convolutions: moving beyond fingerprints. *Journal of computer-aided molecular design*, 30(8):595–608, 2016.
- (60) Bharath Ramsundar, Peter Eastman, Patrick Walters, Vijay Pande, Karl Leswing, and Zhenqin Wu. Deep learning for the life sciences. *O'Reilly: Sebastopol, CA, US*, 2019.
- (61) Ilya Loshchilov and Frank Hutter. Sgdr: Stochastic gradient descent with warm restarts. *arXiv preprint arXiv:1608.03983*, 2016.
- (62) Hyuntae Lim and YounJoon Jung. Mlsolv-a: A novel machine learning-based prediction of solvation free energies from pairwise atomistic interactions. *arXiv preprint arXiv:2005.06182*, 2020.

- (63) T Wesolowski and Arieh Warshel. Ab initio free energy perturbation calculations of solvation free energy using the frozen density functional approach. *The Journal of Physical Chemistry*, 98(20):5183–5187, 1994.
- (64) Shuangliang Zhao, Zhehui Jin, and Jianzhong Wu. New theoretical method for rapid prediction of solvation free energy in water. *The Journal of Physical Chemistry B*, 115(21):6971–6975, 2011.
- (65) Devleena Shivakumar, Joshua Williams, Yujie Wu, Wolfgang Damm, John Shelley, and Woody Sherman. Prediction of absolute solvation free energies using molecular dynamics free energy perturbation and the oplis force field. *Journal of chemical theory and computation*, 6(5):1509–1519, 2010.
- (66) Pan Zhang, Lin Shen, and Weitao Yang. Solvation free energy calculations with quantum mechanics/molecular mechanics and machine learning models. *The Journal of Physical Chemistry B*, 123(4):901–908, 2018.
- (67) Dejun Jiang, Zhenxing Wu, Chang-Yu Hsieh, Guangyong Chen, Ben Liao, Zhe Wang, Chao Shen, Dongsheng Cao, Jian Wu, and Tingjun Hou. Could graph neural networks learn better molecular representation for drug discovery? a comparison study of descriptor-based and graph-based models. *Journal of cheminformatics*, 13(1):1–23, 2021.
- (68) Andrea Mauri, Viviana Consonni, Manuela Pavan, and Roberto Todeschini. Dragon software: An easy approach to molecular descriptor calculations. *Match*, 56(2):237–248, 2006.

## Chapter 6 Conclusion

Emissive materials are inevitable components in modern and emerging technologies such as solid-state lighting, electronic display, bio and chemical sensors for detection of various targets, bio-probes for imaging, and bioelectronics for optical stimulation. Unlike inorganic semiconductors, organic semiconductors can produce singlet and triplet excitons depending on their electrons' spin state upon excitation. In an OLED device, electrically injected uncorrelated charge carriers form singlet and triplet excitons in a 1:3 ratio. However, only the singlet excitons induce fluorescent emission, which limits the internal quantum efficiency (IQE) of fluorescent dyes to only 25%.

The goal of OLED research is to overcome the limitation imposed by forbidden decay from triplet states. In order to harness both singlet and triplet states for light emission applications, phosphorescent materials such as Ir and Pt complexes can be used to accelerate the intersystem crossing (ISC) owing to the heavy atom effect. Heavy atoms such as bromine has also been used for development of purely organic phosphorescence materials. Another promising pathway to achieve 100% IQE is to enhance  $T_1$  to  $S_1$  reverse intersystem crossing (rISC) by carefully designing organic molecules that exhibit a small energy gap ( $\Delta E_{ST}$ ) between  $S_1$  and  $T_1$  levels. This allows for non-radiative triplet states to up-convert to radiative singlet states, a process called thermally activated delayed fluorescence (TADF).

Despite the advantages of TADF materials like full usage of triplet excitons, their intrinsic limitation is the broad emission that reduces color purity. It has been long hypothesized



that rotation between donor and acceptor is the major cause of color purity issues since conventional TADF molecules typically involve large dihedral angle to introduce twisted intramolecular charge transfer (TICT). However, in chapter 2, we have shown that charge transfer characteristics play the pivotal role and determines the emission bandwidth of the TADF emitters. Our results suggest that a higher HOMO-LUMO overlap results in a narrower emission bandwidth. However, substantial HOMO-LUMO overlap also leads to a larger  $\Delta E_{ST}$ , which decreases the efficiency of the TADF emitters. Therefore, future efforts are directed towards designing TADF molecules with a higher HOMO-LUMO overlap; A presence of the  $^3n\pi^*$  triplet state is necessary to enhance rISC and compensate for the relatively large singlet-triplet energy gap.

Room-temperature phosphorescence from metal-free purely organic phosphors has attracted considerable interests for optical imaging in biology because of the unclear toxicities and high costs of the metal complexes. Without having metals with a heavy nucleus, purely organic molecules severely suffer from weak spin-orbit coupling interactions and consequently predominant non-radiative decay routes. Various design principles are adopted for purely organic phosphor exhibiting bright room-temperature phosphorescence; one of which is to use strong halogen bonding between bromine and the hydrogen of the neighboring molecules, which reduces the non-radiative decays by rigidification of the system. In chapter 3, we have shown how halogen bonding can effectively suppress vibrations and prevent non-radiative decays. Although these molecules are very promising for developing purely organic phosphors, they still cannot be used for practical applications because they require crystalline materials. Therefore, future efforts are directed towards designing molecular frameworks that can emit phosphorescence in solution or in an amorphous polymer matrix. Moreover, the emission

lifetime of the purely organic phosphors is as fast as millisecond regime, limiting their practical OLED applications. Thus, a breakthrough in material design of organic phosphor is demanding.

Hybrid fluorescent/phosphorescent single molecule white light emitters (SMWLE) has attracted considerable interest in lighting, sensing, and imaging applications. Moreover, SMWLEs are useful for lighting application where only one emissive layer is used for fabricating the device saving cost on fabrication expenses. In chapter 4, we have designed a fluorine-based molecular framework for developing white OLEDs by combining fluorescent and phosphorescent from a single molecule. We believe a rigid structure is essential for efficient phosphorescence emission so that the vibration is suppressed. Also, the fluorescence emission can be enhanced by suppressing the  $S_1$  to  $T_1$  El-Sayed enhanced intersystem crossing. Therefore, future efforts are directed towards synthesizing the suggested molecules and verifying the computational results presented in this chapter.

The primary objective of this thesis is to develop computational-driven rational molecular design principles of purely organic compounds for OLEDs. In our research strategy, we synergistically combine computation and experiments. In this effective research approach, computation is guiding experiments by predicting molecular and structural blueprints with specified performance characteristics and by helping to interpret experimental observations. Accordingly, the workflow encompasses:

1. Devising molecular design strategies based on past research experiences, literature review, etc.
2. Conceiving of candidate molecular building blocks and prediction of their properties, gauging their potential application for OLED applications.

3. Screening of a large number of candidate molecules derived from these basic building blocks, using DFT-based prediction of their ground state geometries, followed by a vibrational frequency analysis to confirm the stability of the optimized structures. Time-dependent density functional theory (TD-DFT) are carried out to study the excited state properties, including transition compositions, vertical excitation energies, nature of the states, and oscillator strength. Furthermore, natural transition orbitals (NTOs) are calculated using TD-DFT to analyze the electronic configuration of the low-lying singlet and triplet states. Molecular dynamic (MD) simulations can also be used to study the molecular conformations and analyzing the physical movements of atoms and molecules.
4. Identifying the most promising molecular candidates based on the simulation results, and developing chemical synthesis routes for selected candidates.
5. Characterizing the structures of synthesized materials and measuring their opto-electronic properties. Characterization includes studying the  $^1\text{H}$  NMR,  $^{13}\text{C}$  NMR, and Mass Spectrometry spectra. Opto-electronic measurements includes UV-visible absorption spectra, fluorescence, and phosphorescence emission spectra, experimental  $\Delta E_{\text{ST}}$  by comparing the fluorescence and phosphorescence spectra, steady state and delayed emission spectra, temperature dependent emission spectra, etc.
6. Analyzing the findings and validating the predictive design simulation framework. Governing principles underlying materials properties are identified which provides feedback to improve the design concepts conjectured in step 1.

We have succeeded this research approach and workflow in different projects presented in this thesis. Although for most of the computational studies presented in chapter 2, 3, and 4, quantum chemical simulations have been used, molecular dynamics simulations can also be used

where appropriate. DFT, MD, and hybrid quantum mechanics/molecular mechanics (QM/MM) are common strategies for predicting molecular properties and conformational studies.

Traditionally, these methods have been widely used to calculate various molecular properties without experimentation. High-performance computational screening based on these approaches has become routine, giving researchers the ability to simulate the properties of thousands of chemical compounds as part of a single study. However, their applications in real practice may be limited considering the high computational cost of running these advanced methods, as well as their low accuracy, especially for large systems. In chapter 5, we have shown how artificial intelligence and machine learning can be used for material property prediction and accelerating the design principles.

Recent developments in machine learning (ML) and deep learning (DL), have enabled researchers to predict the structure and properties of complex materials with an accuracy comparable to computational chemistry methods. An ML algorithm trains a machine learning predictive model using a training set of input-output pairs so that the model is able to learn from the input data. Therefore, these models perform well as we gather more data, and the training set gets larger. In materials science, machine learning is critical in areas such as new material discovery and material property prediction. Computational chemistry simulations and experimental measurements are two conventional methods that are widely adopted in the field of materials science. However, it is difficult to use these two methods to accelerate materials discovery and design because they are often time consuming and inefficient. With the launch of the Materials Genome Initiative, a large effort has been made by material scientists to collect extensive datasets of materials properties. These datasets include pre-existing computational simulations and experimental measurements. Therefore, machine learning techniques can be

used for finding patterns in this high-dimensional data, providing a fast and reliable solution for predicting the inherent properties of a large number of candidate molecules.

As a result, the use of machine learning models has become more widespread as they are computationally efficient and, in some cases, more accurate. We believe such promising predictive models will be applicable to enhancing the efficiency of the screening of candidate molecules for any material development program, especially OLED applications, as conjectured in step 3.

## Appendices

### Appendix A

#### Supporting Information for Chapter 2

##### UV-vis absorption and Photoluminescence spectra

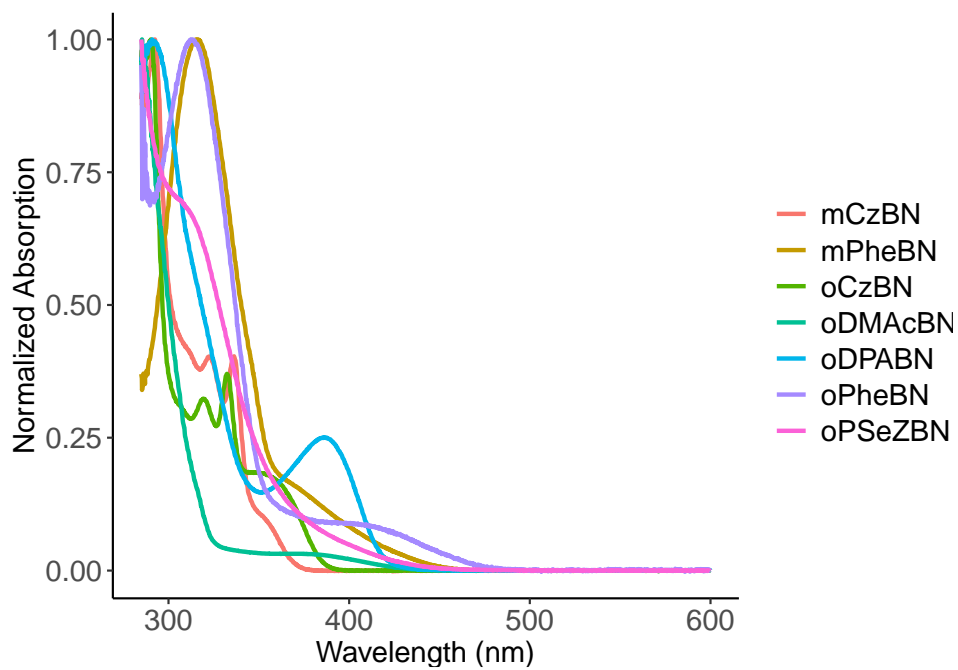


Figure A-1. UV-vis absorption spectra of the investigated molecules.

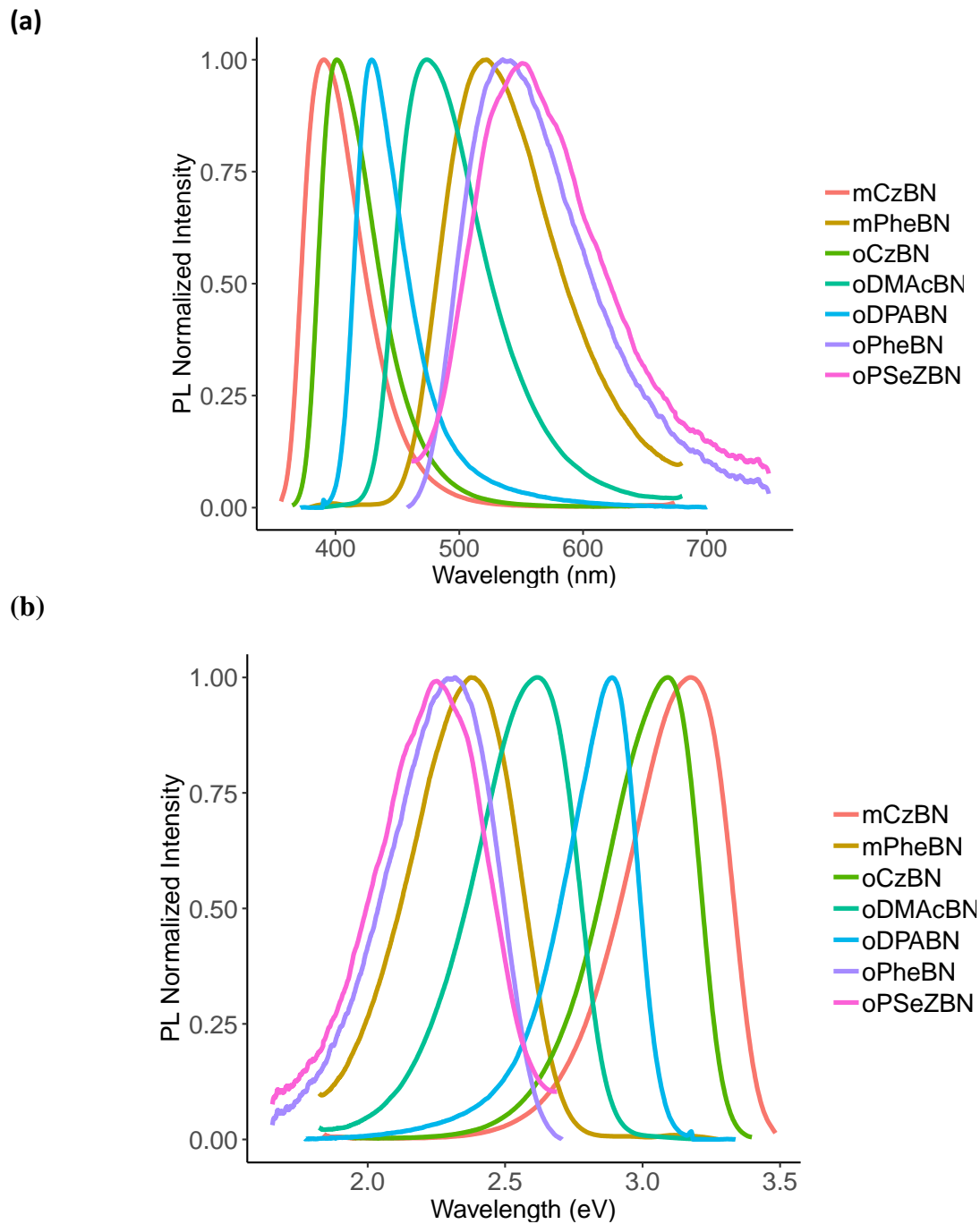
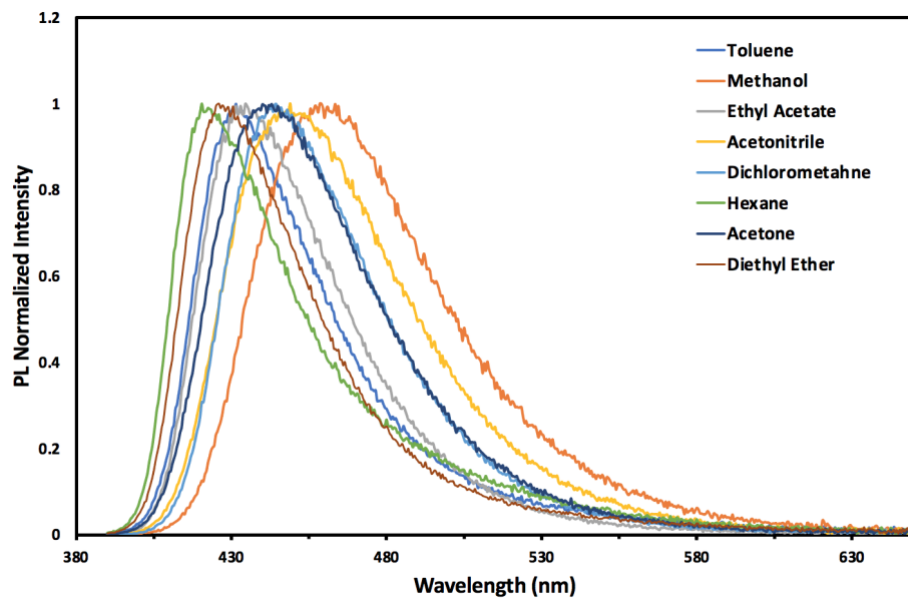


Figure A-2. Photoluminescence spectra of the investigated molecules (a) in nm and (b) in eV.

### Photoluminescence spectra of oDPABN in various solvents

(a)



(b)

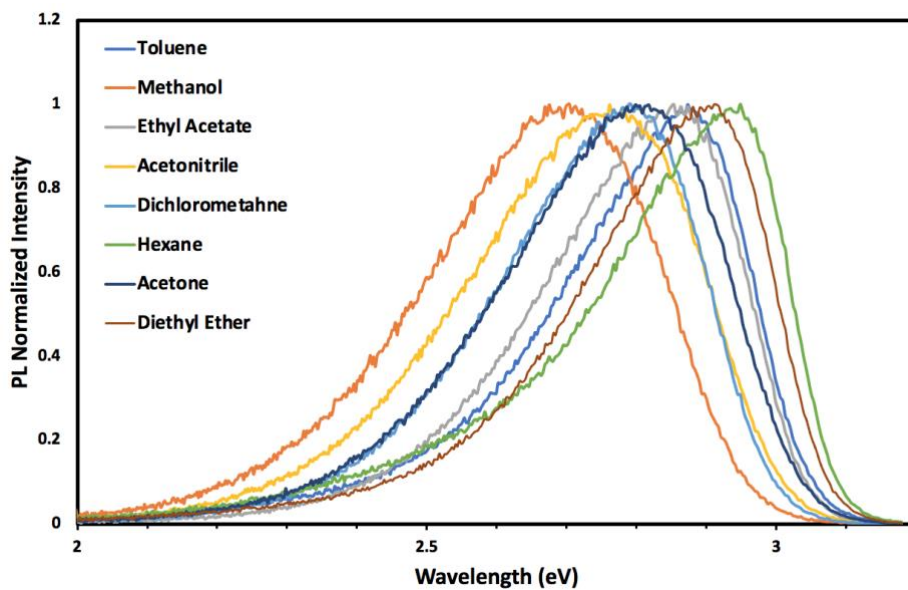
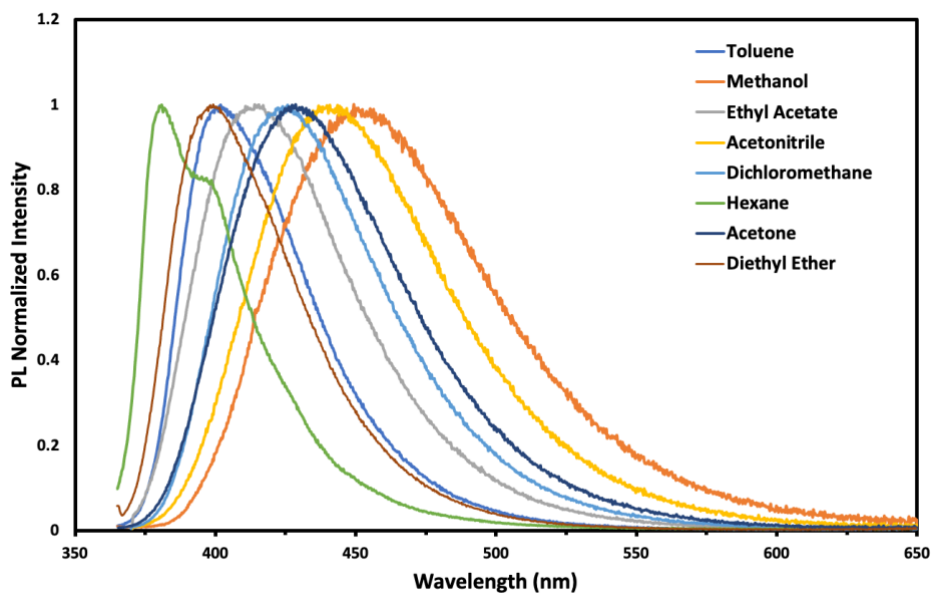


Figure A-3. Photoluminescence (PL) spectra of oDPABN in various solvents (a) in nm and (b) in eV (concentration  $10^{-5}$ M).



### Photoluminescence spectra of oCzBN in various solvents

(a)



(b)

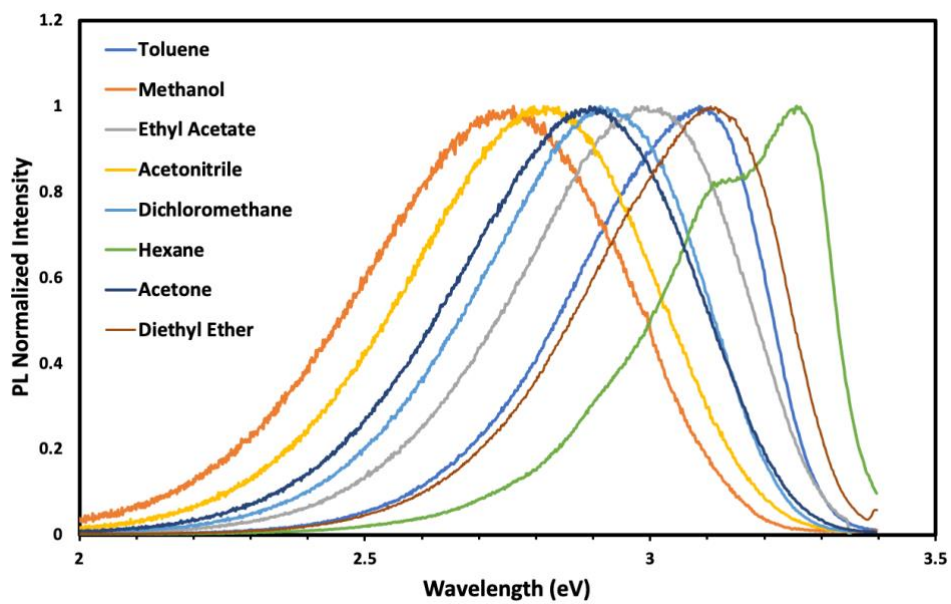


Figure A-4. Photoluminescence (PL) spectra of oCzBN in various solvents (a) in nm and (b) in eV (concentration  $10^{-5}$ M).

**Correlation between measured FWHM and calculated HOMO/LUMO overlap of oCzBN in various solvents**

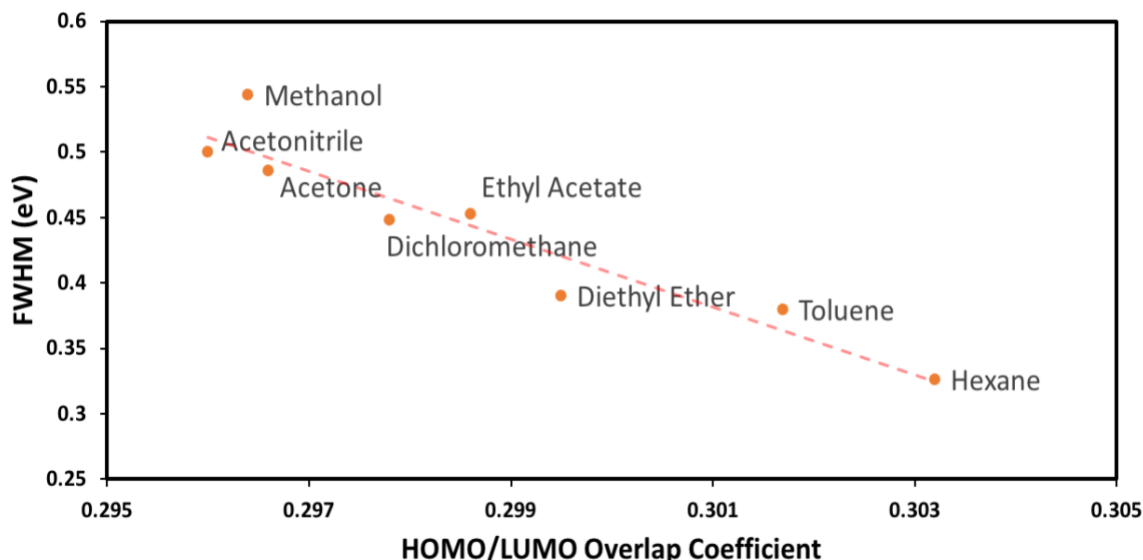


Figure A-5. Correlation between measured FWHM and calculated HOMO/LUMO overlap of oCzBN in various solvents using the polarizable continuum model (PCM) at the CAM-B3LYP/6-31G(d,p) level. More details can be found in the computational method section.

Table A-1. Summary of emission peak, FWHM, and HOMO/LUMO overlap coefficient of oCzBN in various solvents along with their relative polarity.

Solvents	Hexane	Diethyl Ether	Toluene	Ethyl Acetate	Dichloromethane	Acetone	Acetonitrile	Methanol
Relative polarity <sup>[a]</sup>	0.009	0.145	0.099	0.228	0.309	0.355	0.460	0.762
Emission peak (nm)	381	399	402	414	426	429	441	449
FWHM (nm)	40.5	52.0	51.5	64.5	67.0	74.0	80.5	91.8
FWHM (eV)	0.326	0.390	0.379	0.452	0.448	0.486	0.500	0.543
HOMO/LUMO overlap coefficient <sup>[b]</sup>	0.3032	0.2995	0.3017	0.2986	0.2978	0.2966	0.296	0.2964

[a] The values for relative polarity are normalized from measurements of solvent shifts of absorption spectra and were extracted from Christian Reichardt, *Solvents and Solvent Effects in Organic Chemistry*, Wiley-VCH Publishers, 3rd ed., 2003.

## HONTO LUNTO analysis for the first singlet state transition

Table A-2. [a] HONTO/LUNTO overlap coefficient for the first singlet state transition, [b] HOMO/LUMO overlap coefficient for ground state optimized structure and [c] HOMO/LUMO percentage for S1 transition which shows the S1 transition is mostly HOMO to LUMO at B3LYP/6-31G(d,p) level. [d] HONTO/LUNTO overlap coefficient for the first singlet state transition, [e] HOMO/LUMO overlap coefficient for ground state optimized structure at CAM-B3LYP/6-31G(d,p) level

Compound	HONTO/LUNTO overlap <sup>[a]*</sup>	HOMO/LUMO overlap <sup>[b]*</sup>	HOMO → LUMO percentage for S1 transition <sup>[c]*</sup>	HONTO/LUNTO overlap <sup>[d]**</sup>	HOMO/LUMO overlap <sup>[e]**</sup>
1 oDPABN	0.4754	0.4856	98.3%	0.5034	0.4912
2 oCzBN	0.3081	0.3057	99.2%	0.3702	0.3097
3 oPheBN	0.2165	0.2145	98.6%	0.2351	0.2234
4 oDMAcBN	0.2077	0.2063	98.8%	0.2177	0.2072
5 oDPSeZBN	0.1969	0.1687	97.9%	0.2373	0.1795

\* B3LYP/6-31G(d,p)

\*\* CAM-B3LYP/6-31G(d,p)

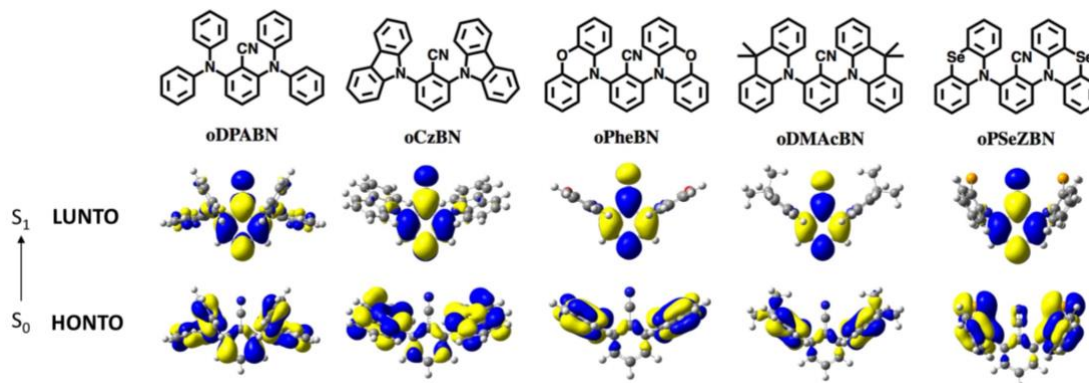


Figure A-6. Chemical structures and calculated distributions of HONTO and LUNTO for the first singlet state ( $S_1$ ) transition at CAM-B3LYP/6-31G(d,p) level.

### Photophysical properties of oDPABN, oDMAcBN, and oPSeZBN

Table A-3. Photophysical data for oDPABN, oDMAcBN, and oPSeZBN in Toluene at 300 K (concentration  $10^{-5}\text{M}$ ). Second column shows the excitation wavelength used for the measurement. Third and fourth column show the absolute quantum yield (QY) in air and relative QY in vacuum, respectively. The QY is measured in air only, and the relative QY in vacuum is calculated by comparing the emission intensity with and without air. The photophysical properties and TADF characteristic of oCzBN, mCzBN, oPheBN, and mPheBN have been reported in the literature; all other molecules are synthesized and characterized for the first time in this work. This table shows that the oDMAcBN and oPSeZBN have TADF characteristic, since the QY increases in vacuum condition (No oxygen). However, oDPABN does not have TADF characteristic and that's because of the relatively large  $\Delta E_{\text{ST}}$  of this compound ( $\Delta E_{\text{ST}} = 0.313 \text{ eV}$ ).

Compound	Excitation Wavelength (nm)	$\Phi_{\text{Air}}$	$\Phi_{\text{Vacuum}}$
oDPABN	385	8.89%	8.89%
oDMAcBN	371	6.96%	10.76%
oPSeZNM	320	1.01%	3.15%